



저작자표시-비영리-변경금지 2.0 대한민국

이용자는 아래의 조건을 따르는 경우에 한하여 자유롭게

- 이 저작물을 복제, 배포, 전송, 전시, 공연 및 방송할 수 있습니다.

다음과 같은 조건을 따라야 합니다:



저작자표시. 귀하는 원저작자를 표시하여야 합니다.



비영리. 귀하는 이 저작물을 영리 목적으로 이용할 수 없습니다.



변경금지. 귀하는 이 저작물을 개작, 변형 또는 가공할 수 없습니다.

- 귀하는, 이 저작물의 재이용이나 배포의 경우, 이 저작물에 적용된 이용허락조건을 명확하게 나타내어야 합니다.
- 저작권자로부터 별도의 허가를 받으면 이러한 조건들은 적용되지 않습니다.

저작권법에 따른 이용자의 권리는 위의 내용에 의하여 영향을 받지 않습니다.

이것은 [이용허락규약\(Legal Code\)](#)을 이해하기 쉽게 요약한 것입니다.

[Disclaimer](#)

공학박사 학위논문

**Structural Modification of
Polymer Electrolyte Membrane Fuel Cells
Components**

고분자 전해질 연료전지
구성요소의 구조적 변경

2018 년 8 월

서울대학교 대학원

화학생물공학부

안 치 영

Structural Modification of Polymer Electrolyte Membrane Fuel Cells Components

고분자 전해질 연료전지

구성요소의 구조적 변경

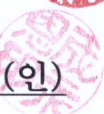
지도교수 성 영 은

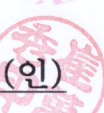
이 논문을 공학박사 학위논문으로 제출함
2018년 8월

서울대학교 대학원
화학생물공학부
안 치 영

안치영의 공학박사 학위논문을 인준함
2018년 8월

위 원 장 유 제 용 (인) 

부위원장 성 영 은 (인) 

위 원 최 만 수 (인) 

위 원 유 성 중 (인) 

위 원 조 응 훈 (인) 

Abstract

Structural Modification of Polymer Electrolyte Membrane Fuel Cells Components

Chi-Yeong Ahn

School of Chemical and Biological Engineering

The Graduate School

Seoul National University

Polymer electrolyte fuel cells (PEFCs) are being investigated as applications of hydrogen, one of the candidates to replace fossil fuels due to near zero emissions. However, since the price merit and the performance are still far from the internal combustion engine due to expensive components, much research is still required for commercialization. These components are mainly membrane, electrode, gas diffusion layer, and flow field. Therefore, the main theme of this thesis is to analyze the improved performance and durability by structurally changing the components of the fuel cell.

Chapter 1 briefly introduces the polymer electrolyte membrane fuel cell. Then the features, roles, and challenges of fuel cell components are addressed.

In chapter 2, a metal foam was characterized and applied as a flow field in a PEFC unit cell. In addition, the electrochemical performance of the metal foam was

compared with that of the commonly used serpentine flow field. At a relative humidity (RH) of 100%, no significant difference in performance was observed between the metal foam and serpentine flow field. However, the performance of a single cell with the metal foam was superior to that of the common flow field under an RH of 20% under pressurized conditions. Furthermore, the factors affecting fuel cell performance by application of the flow field were discussed.

In chapter 3, we have achieved performance enhancement of PEFC through crack generation on its electrodes. It is the first attempt to enhance the performance of PEFC by using cracks which are generally considered as defects. The pre-defined, cracked electrode was generated by stretching a catalyst-coated Nafion membrane. With the strain-stress property of the membrane that is unique in the aspect of plastic deformation, membrane electrolyte assembly (MEA) was successfully incorporated into the fuel cell. Cracked electrodes with the variation of strain were investigated and electrochemically evaluated. Remarkably, mechanical stretching of catalyst-coated Nafion membrane led to a decrease in membrane resistance and an improvement in mass transport, which resulted in enhanced device performance. In chapter 4, Guided cracks were successfully generated in an electrode using the concentrated surface stress of a prism-patterned Nafion membrane. An electrode with guided cracks was formed by stretching the catalyst-coated Nafion membrane. The morphological features of the stretched membrane electrode assembly (MEA) were investigated with respect to variation in the prism pattern dimension (prism pitches of 20 μm and 50 μm) and applied strain ($S \approx 0.5$ and 1.0). The behaviour of water on the surface of the cracked electrode was examined using environmental scanning electron microscopy. Guided cracks in the electrode layer were shown to be efficient water reservoirs and liquid water passages. The MEAs with and without guided cracks were incorporated into fuel cells, and electrochemical measurements were conducted. As expected, all MEAs with guided cracks

exhibited better performance than conventional MEAs, mainly because of the improved water transport.

In chapter 5, to increase the durability of highly loaded platinum- and platinum-nickel alloy catalysts possessing different types of carbon supports, a nitrogen-doped carbon shell was introduced on the catalyst surface through dopamine coating. As the catalyst surfaces were altered following shell formation, the ionomer contents of the catalyst inks were adjusted to optimise the three-phase boundary formation. Single cell tests were then conducted on these inks by applying them in a membrane electrolyte assembly. Furthermore, to confirm the durability of the catalysts under accelerated conditions, the operation was continued for 200 h at 70 °C and at a relative humidity of 100%. Transmission electron microscopy and electrochemical analysis were conducted before and after the durability tests, and the observed phenomena were discussed for catalysts bearing different types of carbon supports.

In appendix A, development of a single cell for X-ray absorption fine structure (XAFS) analysis is described. Also, we developed a new type of single cell system to enable XAFS analysis under real operating condition. In this system, the electrode can be analyzed at practical fuel cell operation conditions, and signals will be obtained in fluorescence mode and transmission mode. This study will play a major role in analyzing fuel cell components in actual driving conditions in the future.

Keywords: Fuel Cells, Components, Flow Field, Membrane Electrode Assembly, Structural Modification, Performance, Durability

Student number: 2014-31090

Contents

Abstracti

Contentsiv

List of Tablesvii

List of Figuresix

Chapter 1. Introduction1

1.1. General introduction to fuel cells.....1

1.2. Aim of this thesis.....8

1.3. References13

**Chapter 2. Effect of Porous Metal Flow Field in Polymer
Electrolyte Membrane Fuel Cell under Pressurized
Condition17**

2.1. Introduction17

2.2. Experimental section20

2.3. Results and discussion26

2.4. Conclusions49

2.5. References50

Chapter 3. High-performance Fuel Cell with Stretched Catalyst-Coated Membrane: One-step Formation of Cracked Electrode.....59

3.1. Introduction59
3.2. Experimental section61
3.3. Results and discussion65
3.4. Conclusions86
3.5. References87

Chapter 4. Guided cracking of electrodes by stretching prism-patterned membrane electrode assemblies for high-performance fuel cells90

4.1. Introduction90
4.2. Experimental section92
4.3. Results and discussion95
4.4. Conclusions117
4.5. References119

Chapter 5. Effect of N-doped Carbon Coatings on the Durability of Highly loaded Platinum and Alloy Catalysts with Different Carbon Supports for Polymer Electrolyte Membrane Fuel Cells.....124

5.1. Introduction124

5.2. Experimental section	128
5.3. Results and discussion	131
5.4. Conclusions	156
5.5. References	158

Appendix A. Preparation of <i>In-situ</i> XAFS Cell In-operando Single Cell Tests for Structural Analysis of Cathode Catalyst	165
--	------------

국문 초록 (Abstract in Korean)	170
---	------------

List of Publications (SCI)	173
---	------------

List of Tables

Chaper 1

-

Chaper 2

Table 2.1. Electrochemical properties of fuel cell with the serpentine and porous flow fields. For the polarization curve and EIS results, the temperatures of the cell and humidifier were maintained 70°C (100% RH), and H ₂ and air were supplied with a stoichiometry of 1.5:2.0 to the anode and cathode, respectively. For CV measurements, the temperatures of the cell (30°C) and humidifiers (35°C) were maintained constant. H ₂ and N ₂ were supplied to the anode and cathode at constant flow rates of 50 and 200 sccm, respectively.....	33
Table 2.2. Summary of performance of SCS and SCCF at atmospheric condition.....	39
Table 2.3. Summary of performance of SCS and SCCF at pressurized condition.....	44
Table 2.4. Current density at 0.6 V and the maximum power density of single cells at 20% RH under atmospheric pressure and pressurized conditions (180 kPa). For this performance curve, the temperatures of the cell (70°C) and humidifier (36.8°C) were maintained constant, and H ₂ and air were supplied with a stoichiometry of 1.5:2.0 to the anode and cathode, respectively.....	46

Chaper 3

Table 3.1 Physical property of Nafion 212 membrane.....	68
Table 3.2 Physical and electrochemical properties of the samples.....	76
Table 3.3 Electrochemical impedance spectroscopy (EIS) fitted data.....	81

Chaper 4

Table 4.1 Physical properties of the Nafion membrane.100

Table 4.2 Maximum power densities and current densities at 0.6 V for the prism-patterned MEAs.....112

Table 4.3 Electrochemical impedance spectroscopy (EIS) fitted data.116

Chaper 5

Table 5.1 Summary of the electrochemical analyses of PC, PNHC, PCD, and PNHCD.....145

List of Figures

Chaper 1

Figure 1.1 Classification and reactions of Fuel Cells by Different Types of Electrolytes	2
Figure 1.2 Genenal components of the PEFC	4
Figure 1.3 Sturcture of Nafion® (1100 of Equivalent Weight).	5
Figure 1.4 Drawing of physically machined flow field in a bipolar plate.	7
Figure 1.5 Comparison of mass activity of various platinum-based catalysts at liquid half cell and practical fuel cell level.	9

Chaper 2

Figure 2.1 General components of a unit cell (a) and designed drawing and photograph of a bipolar plate with the serpentine flow field (b) and metal foam flow field (c).	22
Figure 2.2 Schematic diagram of the MEA with conventional flow field (a) and metal foam flow field (b).....	23
Figure 2.3. SEM images of the pristine copper metal foam (a)–(c) and compressed copper metal foam (d)–(e), Scale bar 100 μm . (c) and (f) represent cross-sectional images before and after compression.	27
Figure 2.4. Pore distribution of the pristine (blue line, average pore size of 167.38 μm and 83.13% average porosity) and compressed metal foam (red line, average pore size of 167.08 μm and 78.50% average porosity) by mercury intrusion porosimetry.....	28
Figure 2.5 Voltage profiles of single cells with (a) the conventional serpentine (b) nickel foam, and (c) copper foam flow fields during activation. The inset shows	

pictures of each flow field. The temperatures of the single cells and all humidifiers were maintained 70°C (100% RH) during this process without backpressure, and H₂ and O₂ were supplied to the anode and cathode at a constant flow of 150 and 200 sccm, respectively.30

Figure 2.6 Results from (a) the polarization curve, (b) CV and (c) EIS with single cells with SCF and SCCF. For polarization curves and EIS results, the temperatures of the cell and humidifier were maintained at 70°C (100% RH), and H₂ and air were supplied with a stoichiometry of 1.5:2.0 to the anode and cathode, respectively. For CV measurements, the temperatures of the cell (30°C) and humidifiers (35°C) were maintained constant. H₂ and N₂ were supplied to the anode and cathode at constant flow rates of 50 and 200 sccm, respectively.31

Figure 2.7 EDS spectra of the copper foam (a) before and (b) after single-cell operation, and (c) current density profile of SCCF in the constant voltage mode (inset: EDS mapping images before and after fuel-cell operation). For the constant voltage (0.63 V) test, the temperatures of the single cell and all humidifiers were maintained at 70°C (100% RH) during this process without backpressure, and H₂ and air were supplied to the anode and cathode at constant flow rates of 150 and 200 sccm, respectively.35

Figure 2.8 Polarization curve of fuel cells with SCS and the partially corrected curve of SCCF. For this performance curve, the temperatures of the cell and humidifier were maintained at 70°C (100% RH), and H₂ and air were supplied with a stoichiometry of 1.5:2.0 to the anode and cathode, respectively.37

Figure 2.9 Polarization curve for SCS and SCCF with various relative humidity (a) RH80, (b) RH60, (c) RH 40, and (d) RH 20 at atmospheric condition.....38

Figure 2.10 Performance curve of SCS and partially corrected curve of SCCF under backpressure condition (180 kPa) at 100% RH. For this performance curve, the temperatures of the cell and humidifier were maintained at 70°C, and H₂ and air

were supplied with a stoichiometry of 1.5:2.0 to the anode and cathode, respectively.....	41
Figure 2.11 Polarization curve for SCS and SCCF with various relative humidity (a) RH100, (b) RH 80, (c) RH 60, and (d) RH 40 at pressurized condition.....	42
Figure 2.12 Polarization curve of SCS and non-corrected curve of SCCF under pressurized condition (180 kPa) at 20% RH. For this performance curve, the temperatures of the cell (70°C) and humidifier (36.8°C) were maintained constant, and H ₂ and air were supplied with a stoichiometry of 1.5:2.0 to the anode and cathode, respectively.....	45
Figure 2.13 Schematic diagram of the metal foam flow field under low RH and pressurized conditions.....	48

Chaper 3

Figure 3.1 A camera image for one channel serpentine-type.	62
Figure 3.2 (a-c) Camera images for the preparation of stretched MEA within ~5 cm ² active area. (d) Changes of width and height of Nafion membrane with variation of strains (0.5, 1.0, 1.5 and 2.0).	63
Figure 3.3. Generation of cracks in the electrode: (a) Schematic illustration of generating cracks in Pt/C catalyst layer with simply mechanical stretching. (b) Corresponding SEM images of catalyst layer before (left) and after (right) stretching out the catalyst coated membrane (Inset: corresponding optical images of stretcher machine)	66
Figure 3.4 Physical property of Nafion membrane: Stretching properties of Nafion 212 membrane. (a) Strain-stress curves of Nafion membrane obtained by applying strain to the membrane until its breaks. (b) Changes of width, height and thickness of Nafion membrane with variation of strains (0.5, 1.0, 1.5 and 2.0).	67

Figure 3.5 Measurement of the membrane thickness after stretching out the membrane	70
Figure 3.6 Morphological features of the generated cracks and measurements of device performance: (a) Corresponding SEM images of catalyst coated membrane after applying various strains (0.5, 1.0, 1.5 and 2.0). (b,c) Polarization curves of conventional membrane electrode assembly (MEA) and the MEA with electrode cracks with variation of strains (0.5, 1.0, 1.5 and 2.0) under the conditions of H ₂ /O ₂ (b) and H ₂ /Air (c).	71
Figure 3.7 The results of maximum power densities according to the ratio of cracks in the MEAs.....	73
Figure 3.8. SEM images for catalyst layer of stretched MEA for each strain (0.5, 1.0, 1.5 and 2.0)	75
Figure 3.9 Accelerated durability test (ADT) for the stretched MEA with 1.5 strain and reference MEA.....	77
Figure 3.10 SEM images for catalyst layer of stretched MEA before ADT(a) and after ADT(b)	78
Figure 3.11 Electrochemical analysis: (a) Cyclic voltammogram (CV) of the cathode catalyst layers of a conventional MEA and the 1.5-strain applied MEA. (b) Electrochemical impedance spectroscopy (EIS) of a conventional MEA and the 1.5-strain applied MEA. at 0.6 V compared with RHE. (c) Equivalent circuit of the PEFC (L_W = inductance of the electric wire, $R_{membrane}$ = internal membrane resistance, $R_{cathode (anode)}$ = charge transfer resistance of the cathode (anode), $CPE_{cathode (anode)}$ = constant phase element of the cathode (anode) and Z_W = Warburg impedance).	80
Figure 3.12 EIS measurements at the same current density ($\sim 1.4 \text{ A cm}^{-2}$) for the sample of reference and stretched MEA (S ~ 1.5)	82
Figure 3.13 The graph for the oxygen gain obtained by calculating potential difference when oxygen and air are supplied respectively.....	83

Figure 3.14 Polarization curves of the stretched MEA and the MEA with only membrane stretched. (a) H₂/O₂ condition, (b) H₂/Air condition.84

Figure 3.15 (a) EIS measurement of the stretched MEA and the MEA with only membrane stretched. (b) Oxygen gain calculation of the stretched MEA and the MEA with only membrane stretched.85

Chaper 4

Figure 4.1 Simulation results for the stress distribution on a Nafion 212 membrane and prism-patterned membranes with pitches of 20 μm and 50 μm.96

Figure 4.2 Schematic illustration of guided crack generation in an electrode by stretching the prism-patterned membrane electrode assembly.97

Figure 4.3 (a, b) SEM images of a Nafion membrane imprinted with a prism mould with a pitch of 20 μm (P-20 membrane) (a) and 50 μm (P-50 membrane) (b). (c, d) Stretching properties of the Nafion membranes: (c) strain–stress curves of the Nafion 212 membrane, 20 μm prism-patterned Nafion membrane, and 50 μm prism-patterned Nafion membrane measured by applying strain to the membranes (Inset: optical image showing the operation of the stretching machine); (d) ratio of height, width, and thickness changes of the Nafion membranes with varying strains (~0.5, ~1.0, and ~1.5).99

Figure 4.4 Morphological features of the generated guided cracks: (a–d) SEM images of the cracks generated after applying strains (*S*) of ~0.5 and ~1.0 to the prism-patterned MEAs with pitches of 20 μm and 50 μm: (a) P-20 MEA with *S* ≈ 0.5, (b) P-20 MEA with *S* ≈ 1.0, (c) P-50 MEA with *S* ≈ 0.5, and (d) P-50 MEA with *S* ≈ 1.0. (e, f) Simulations of the stress distributions on the prism-patterned MEAs with pitches of 20 μm (e) and 50 μm (f).102

Figure 4.5 Simulation of the stress distribution on a prism-patterned MEA with a pitch of 10 μm and an applied strain of ~ 0.5 , and the corresponding SEM image.....	103
Figure 4.6 Cross-sectional SEM images of the P-20 and P-50 MEAs with $S \approx 0.5$ and 1.0, and a conventional MEA.	105
Figure 4.7 Schematic illustrations of the behaviour of generated water in the controlled cracks in the catalyst layer.	106
Figure 4.8. ESEM images of water behaviour on a 20 μm cracked catalyst layer (strain ≈ 0.5) with respect to time: (a) 60 s, (b) 180 s, and (c) 360 s. The chamber pressure and substrate temperature were maintained at ~ 5.1 Torr and ~ 2 $^{\circ}\text{C}$, respectively (RH = 95%).....	107
Figure 4.9 Electrochemical measurements of the MEAs: (a, b) Polarization curves of a conventional MEA and the MEAs with cracks generated using a 20 μm prism pattern (a) and a 50 μm prism pattern (b) with various strains (~ 0.5 and ~ 1.0) under H_2/air . (c) Oxygen gains obtained under ambient pressure. (d) Cyclic voltammetry (CV) measurements of the prism-patterned MEAs with the same strain (~ 0.5) and a conventional MEA at the cathode catalyst layers (NHE = normal hydrogen electrode).	109
Figure 4.10 Measurements of device performance: (a, b) Polarization curves of a conventional MEA, P-20 MEA, and P-50 MEA with the same applied strain of ~ 0.5 (a) and ~ 1.0 (b) under H_2/air	110
Figure 4.11 Polarization curves of conventional MEA, MEA with pre-stretched membrane ($S \sim 0.5$), P-20 patterned MEA with pre-stretched membrane ($S \sim 0.5$) and P-20 patterned MEA with controlled cracks via stretching MEA ($S \sim 0.5$) ...	113
Figure 4.12 Electrochemical impedance spectroscopy (EIS) measurements of prism-patterned MEAs with the same strain (~ 0.5) and a conventional MEA at 0.6 V vs. a reversible hydrogen electrode (a) and at 1.6 A cm^{-2} (b). (c) Equivalent circuit of the PEFC ($L1$ = inductance of the electric wire, $R1$ = internal membrane	

resistance, R3 (2) = charge transfer resistance of the cathode (anode), CPE2 (1) = constant phase element of the cathode (anode), and W1 = Warburg impedance).115

Chaper 5

Figure 5.1 Schematic diagram of the N-doped carbon-coated Pt/CB (top) and Pt₂Ni/HC (bottom) systems before and after the accelerated degradation tests (ADTs).127

Figure 5.2 TEM images of (a) Pt/CB and (b) Pt₂Ni/HC before dopamine coating, and (c) Pt/CB and (d) Pt₂Ni/HC after dopamine coating. The insets in (c) and (d) show high-resolution TEM images.132

Figure 5.3 Particle size distribution of (a) Pt/CB, (b) Pt₂Ni/HC, (c) Pt/CB with N-doped carbon shell, and (d) Pt₂Ni/HC with N-doped carbon shell before ADT ...133

Figure 5.4 TEM images of (a) heat-treated Pt/CB and (b) heat-treated Pt₂Ni/HC without dopamine coating.135

Figure 5.5 TEM images of Pt/CB after 45 min of reaction with dopamine. Inside of the yellow dotted line, carbon shell is partially formed.136

Figure 5.6 The XRD spectra of Pt/CB and the prepared Pt₂Ni/HC catalysts.....137

Figure 5.7 The SEM-EDS results of Pt/CB and the prepared Pt₂Ni/HC catalysts after dopamine coating.138

Figure 5.8 Electrochemical performance curves for (a) PC, (b) PNHC, (c) PCD, and (d) PNHCD. With the exception of PC, the ionomer content tests were performed to optimise the TPB. The ionomer contents relative to the catalyst are noted in the legends.140

Figure 5.9 ORR activity of Pt/CB and Pt₂Ni/HC at 1600 rpm with 10 mV s⁻¹ in 0.5M H₂SO₄ solution.142

Figure 5.10 Electrochemical performance curves for (a) PC, (b) PNHC, (c) PCD, and (d) PNHCD before and after the ADTs.	146
Figure 5.11 Trends of normalised current density (at 0.6 V) and maximum power density with ADT time: (a) PC, (b) PNHC, (c) PCD, and (d) PNHCD.	148
Figure 5.12 CV results for (a) PC, (b) PNHC, (c) PCD, and (d) PNHCD before and after the ADT.	150
Figure 5.13 TEM images of the catalysts extracted from the MEAs after the ADT. (a) Pt/CB and (b) Pt ₂ Ni/HC before dopamine coating, and (c) Pt/CB and (d) Pt ₂ Ni/HC after dopamine coating. The insets in parts (c) and (d) show the high resolution TEM images.	153
Figure 5.14 Particle size distribution of each catalyst extracted from cathode electrode of (a) PC, (b) PNHC, (c) PCD, and (d) PNHCD after ADT.	154

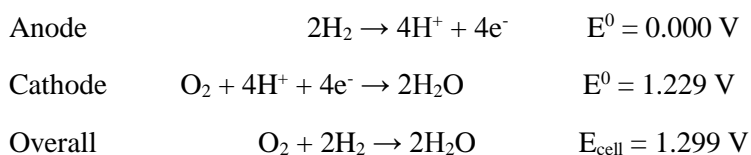
Appendix A

Figure a.1 XAFS measurement pictures of (a) the transmission mode and (b) the fluorescent cell unit cell.....	167
Figure a.2 Fuel cell evaluation system set up at PAL 8C beamline.....	168

Chapter 1. Introduction

1.1. General introduction to fuel cells

Fuel cells (FCs) are energy devices that generate electricity when fuel is supplied.^{1,2} In an internal combustion engine, kinetic energy is converted into electric energy while burning the fuel at high temperature and high pressure, but the FC directly converts the fuel into electric energy.³ They are divided into several types depending on the type of electrolyte as shown in Figure 1.1.⁴ They include polymer electrolytes (PEs), alkaline electrolytes (AFs), phosphoric acid (PA), molten carbonate (MC), and solid oxides (SO).⁵ As for the operating temperature, the PE and AE fuel cells are classified as low temperature FCs, the PA fuel cells as intermediate temperature FC, and MC and SO as high temperature FCs. Among these, PEFC is applied to various applications such as automotive, transport power, distributed power, potable power, auxiliary power, etc. because of its low operating temperature and fast start-up.^{6,7} Therefore, many energy-related companies are trying to commercialize PEFC.



Where E^0 is the standard electrode potential vs. normal hydrogen electrode (NHE). The oxidation of hydrogen occurs at the node and the reduction of oxygen occurs at the cathode. Since the hydrogen electrode is used as a reference, the voltage of the

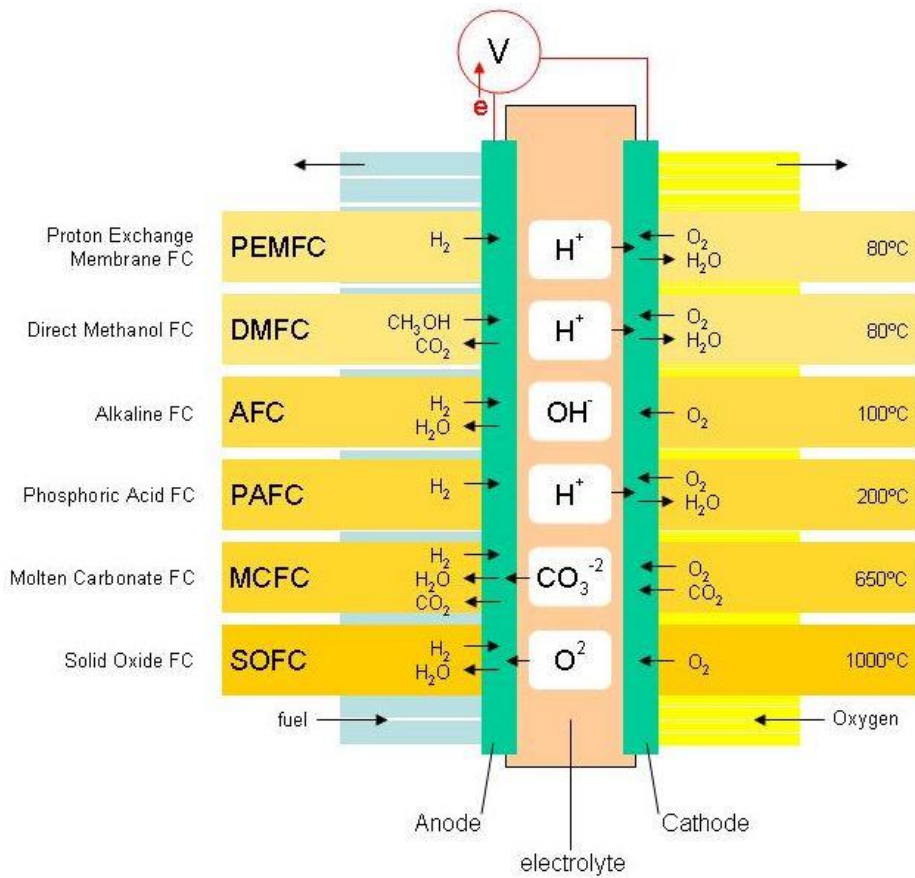


Figure 1.1 Classification and reactions of Fuel Cells by Different Types of Electrolytes (Source, <http://www.jobsinfuelcells.com/fctypes.htm>)

cathode determines the total cell voltage.⁸ Because of the abundant oxygen in the air, fuel cells are energy devices that can generate power in virtually infinite ways if they have only hydrogen sources such as hydrogen gas, methanol ethanol formic acid and etc.⁹ Furthermore, since the product of the cathode is water, it can be said that there is no emission of the greenhouse gas such as carbon dioxide, NO_x, SO_x only by FC itself.¹⁰ However, since the product is H₂O as mentioned earlier, when the operating temperature is higher than the boiling point of water, the transport of the reaction gas is inhibited and the performance of the fuel cell may be decreased. Therefore, it can not operate at high temperature, and therefore, it can be seen that it is inevitable to use precious metal such as platinum, palladium, gold and etc. As mentioned above, many companies are attempting to commercialize a variety of products using PEFC, but it is still being delayed due to the disadvantage of using expensive catalysts of precious metals.¹¹ Therefore, many groups are studying to reduce the use of these precious metals as much as possible or to increase the efficiency of entire system of FCs.¹²

The components of the PEFC are a hydrogen ion (proton) conductive polymer membrane (as an electrolyte), hydrogen oxidation catalysts (anode), an oxygen reduction catalyst (cathode), and a binder, a gas diffusion layer (GDL), bipolar plate containing flow field, as shown in Figure 1.2.^{13,14}

In PEFC, the membrane performs the following functions, i.g. (i) Transfer of proton generated by oxidation of hydrogen at anode to cathode; (ii) Disconnect the anode and the cathode, electrically; (iii) inhibition of gas crossover.¹⁵ A number of studies are underway in various groups, but Nafion[®] produced by Du Pont is currently a commercially available polymer membrane. The structure of Nafion is shown in the Figure 1.3. It is similar in structure to Teflon but contains ether, CF₂ and sulfuric acid in the side chain.^{16,17} In order to compensate the mechanical strength of the thin membrane, a fine mesh type Teflon support was placed in the middle of the Nafion membrane to improve durability and is called supported

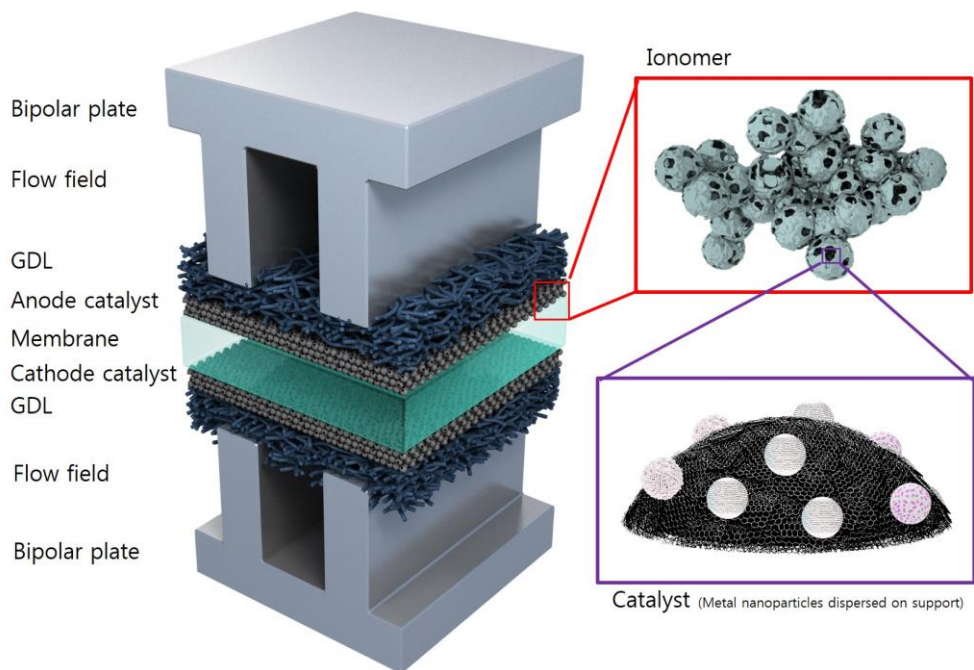


Figure 1.2 General components of the PEFC

membrane.

In both cases of hydrogen oxidation and oxygen reduction, platinum and platinum alloy catalysts are known to be the most active catalysts to date.¹⁸ However, the oxygen reduction reaction (ORR) is more complicated and slower than the hydrogen oxidation reaction (HOR), so the research is mainly focused on the catalyst development for ORR.¹⁹⁻²¹ Since metal was dispersed in porous carbon at nano size, these metal catalysts were able to greatly reduce the amount of use.²²⁻²⁴ However, indeed, the high price of precious metals is still one of the factors that hinders commercialization of fuel cells.

Furthermore, by impregnating the proton conductive material into the catalyst layer, the performance of the fuel cell further increased.^{25,26} When a polymer similar in structure to the membrane is dispersed in a solvent and mixed with a catalyst to prepare electrodes, the material covers the catalyst layer thinly as the solvent is dried. At this time, this material also serves to hold the catalyst layers so that they do not separate from each other, and is also called a binder. The use of binder allows proton transfer to the deep inside of the catalyst layer, which can greatly increase the performance of PEFC by increasing the utilization of the catalyst layer.²⁷

The bipolar plate is called the 'bipolar' plate because it electrically connects the anode to the cathode in the fuel cell stack. The plate is not only electrically connected, but also serves as a frame to support the fuel cell mechanically and as a flow field for the reactive gas.²⁸ Therefore, it should have excellent electrical conductivity, mechanical strength, and corrosion resistance in an acidic environment because the operating conditions of the PEFC are strong acids due to the produced water (or water from humidified gas) and oxidized hydrogen (proton).²⁹⁻³² Furthermore, since the fuels of PEFC are basically gas or liquid phase, the flow of the fluid is artificially induced by physically processing the bipolar plate (figure 1.4) so as to widen the reaction time and reaction area and to consume

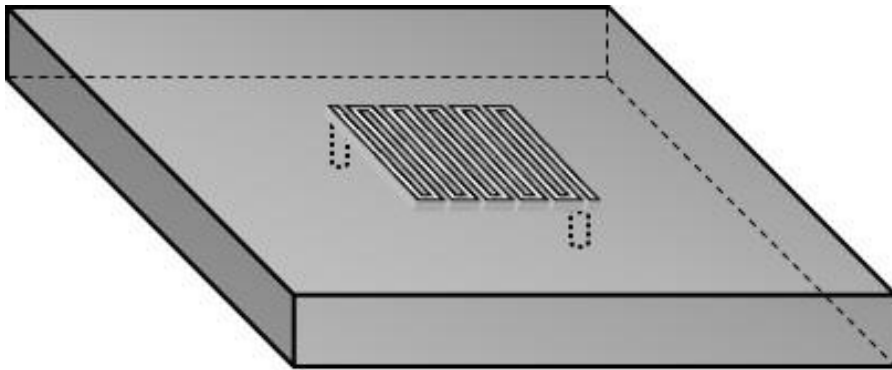


Figure 1.4 Drawing of physically machined flow field in a bipolar plate.

the fuels from the electrode with high efficiency.

1.2. Aim of this thesis

In recent years, the activity of ORR catalysts has steadily increased through several synthetic methods, such as increasing the number of active sites of the catalysts or increasing the activity of the catalyst itself, supporting computer-based calculations.³³

Indeed, the mass activity of structurally controlled Pt or Pt-alloy catalysts increased by several orders of magnitude compared to polycrystalline Pt nanoparticles in liquid half-cell level.³⁴ However, when this activity was measured at the single cell level after incorporation of the catalyst into the membrane electrode assembly (MEA), no significant improvement was observed as increased activity at the half cell level as shown in Figure 1.5.³⁵ There are several arguments for this reason.

Thus, in this study, rather than controlling the metal catalyst for ORR itself, one that improves performance and durability in a practical fuel cell level has been addressed.

1.2.1 Structural modification of flow field

In this study, fuel cell tests using a metal foam flow field were conducted under different RH and pressurized conditions to understand the advantages of porous structures when applied to a flow field. From the results obtained for the experiment under normal pressure and 100% RH, better performance for the conventional serpentine flow field was observed as compared with that observed with the metal foam in the cell. To investigate the effect of water, experiments were conducted under low-humidity conditions, but no improvement in performance was observed. Performance similar to that observed under atmospheric conditions was observed at 100% RH in the low-current-density region, with drastic performance reduction in the high-current-density region. However, the porous flow field

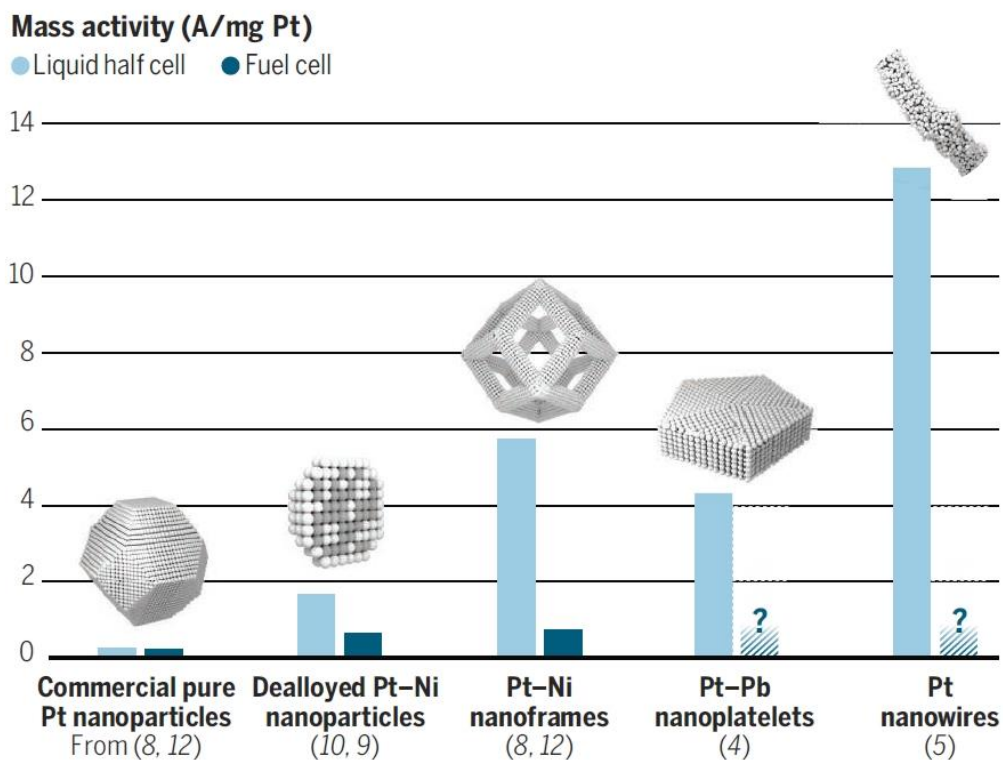


Figure 1.5 Comparison of mass activity of various platinum-based catalysts at liquid half cell and practical fuel cell level. Adapted from Ref [33] (Ifan Erfyl Lester Stephens, Jan Rossmeisl, and Ib Chorkendorff, *Science* **354**, 1378-1379 (2016))

exhibits favorable effects under pressurized and low-humidity conditions and the results were discussed.

1.2.2 Structural modification of MEA

Recently, there have been several technical issues for the commercialization of PEFC including water management at the cathode in the membrane electrode assembly (MEA) and resistance reduction of the electrolyte membrane. In order to address these issues in a simple and effective way, we deliberately generated cracks on the electrode composed of carbon supported Pt particles (Pt/C) by stretching out a membrane electrode assembly (MEA) and used the stretched MEA in order to enhance mass transport in the electrode and to reduce ohmic resistance simultaneously. Recent studies have also indicated that cracks can be used to detect the strain force as in an ultrasensitive sensor, microfluidic channels and so on. In this study, we have presented, for the first time, a novel strategy to improve water transport and reduce ohmic resistance by simply stretching out the Pt/C-coated Nafion membrane.

1.2.3 Structural modification of catalyst surface through carbon coating

Due to the electrochemically harsh operating conditions of PEFCs, research regarding the durability of any materials employed is of particular importance, as degradation of the metal particles dispersed on the carbon supports can occur through migration/dissolution of the metal and corrosion of the carbon itself. When carbon is applied as a protective layer to the surface of the catalyst, the durability of the catalyst is increased by preventing migration and dissolution of the metal. However, most previous studies have introduced a protective carbon shell on a 20 wt% metal catalyst on support. In these cases, the distance between the metal nanoparticles is long because the total amount of the metal is small compared to the support. However, highly loaded catalysts are often used in practical fuel cell

devices to reduce the volume of the electrodes. Thus, we herein report the application of a carbon-based protective layer for highly loaded Pt- and Pt-alloy catalysts on different types of carbon supports to prevent agglomeration of adjacent metal nano-particles during degradation process and/or heat treatment.

1.2.4 Structural modification of electrode surface by improving ionomer properties

The ionomers play roles in conducting protons within the porous electrodes and mechanically supporting the carbon materials with high surface area on which Pt catalyst particles are distributed in nanoscale. The ionomers impregnated for electrode formation largely contributes to improved electrochemical PEFC performances, when compared with those obtained from ionomer-free electrodes. The state-of-the art ionomer materials are perfluorinated sulfonic acid (PFSA) derivatives, which are made up of a chemically robust, hydrophobic poly(tetrafluoroethylene)(PTFE) backbone, and fluorinated side chains containing a hydrophilic sulfonic acid ($-\text{SO}_3\text{-H}^+$) group at each terminal end. Unfortunately, it does not mean that the Nafion® dispersion can offer electrode characteristics enough to guarantee high levels of PEFC performances for a long period of times. In this paper, using supercritical fluid, we developed an ionomer with superior properties such as dispersibility than conventional emulsion polymerization. In addition, it shows higher proton conductivity and crystallinity than conventional one.

1.2.5 Single cell design for analysis of PEFC component

X-ray absorption fine structure (XAFS) is a tool for analyzing the local structure properties, chemical valence state and local density of states of materials. Using this tool, many groups have used them to analyze and study the properties of materials. In the field of fuel cells, the properties of electrocatalysts in various groups were analyzed with the above mentioned tools, which revealed the cause of

increased activity and durability. However, only the characteristics of the material itself were confirmed, and it was difficult to identify the electro-catalyst in which the external influences were reflected. More and more attempts are being made to see the behavior of the catalyst in the MEA state. However, most of the analysis in XAFS and single cell linkage system was only for the development of the phenomenon in nitrogen atmosphere. In this study, we designed a single cell for the analysis of cathode catalyst integrated with MEA rather than a half cell level analysis. Furthermore, a system capable of analyzing not only nitrogen but also oxygen (air) atmospheres was introduced.

1.3. References

- 1 Perry, M. L. & Fuller, T. F. A historical perspective of fuel cell technology in the 20th century. *Journal of the Electrochemical Society* **149**, S59-S67 (2002).
- 2 Dincer, I. Environmental and sustainability aspects of hydrogen and fuel cell systems. *International Journal of Energy Research* **31**, 29-55 (2007).
- 3 Dincer, I. & Rosen, M. A. Sustainability aspects of hydrogen and fuel cell systems. *Energy for Sustainable Development* **15**, 137-146 (2011).
- 4 *Types of Fuel Cells*, <<http://www.jobsinfuelcells.com/fctypes.htm>> (2014).
- 5 O'Hayre, R. Cha, S. Colella, W. Prinz, F. B. Chapter 8 Overview of Fuel Cell Types in *Fuel Cell Fundamentals* (eds R. O'Hayre, Cha, S.; Colella, W.;Prinz, F. B.) (John Wiley & Sons, Inc., 2016).
- 6 Mench, M. M. Chapter 6 Polymer Electrolyte Fuel Cells in *Fuel Cell Engines* (ed M. M.; Mench), 285-379 (John Wiley & Sons, Inc., 2008).
- 7 Westenberger, A. Chapter 5 Hydrogen and Fuel Cells: Mobile Application in Aviation in *Hydrogen and Fuel Cell: Technologies and Market Perspectives* (eds Johannes Töpler & Jochen Lehmann) 107-125 (Springer Berlin Heidelberg, 2016).
- 8 Mench, M. M. Chapter 2 Basic Electrochemical Principles in *Fuel Cell Engines* (ed M. M.; Mench) (John Wiley and Sons Inc., 2008).
- 9 Yuan, X.-Z. & Wang, H. Chapter 1 PEM Fuel Cell Fundamentals in *PEM Fuel Cell Electrocatalysts and Catalyst Layers: Fundamentals and Applications* (ed JiuJun Zhang) 1-87 (Springer London, 2008).
- 10 Sørensen, B. Chapter 1 Introduction in *Hydrogen and Fuel Cells (Second Edition)* 1-4 (Academic Press, 2012).
- 11 Sabine, S. M., Bron. Chapter 15 Catalysis in Low-Temperature Fuel Cells An Overview in *Fuel Cell Science and Engineering* (ed Prof. Detlef Stolten; Dr. Bernd Emonts;) (John Wiley & Sons, 2012).

- 12 Greeley, J. *et al.* Alloys of platinum and early transition metals as oxygen reduction electrocatalysts. *Nature Chemistry* **1**, 552 (2009).
- 13 Jörissen, L. & Garche, J. Chapter 14 Polymer Electrolyte Membrane Fuel Cells in *Hydrogen and Fuel Cell: Technologies and Market Perspectives* (eds Johannes Töpler & Jochen Lehmann) 239-281 (Springer Berlin Heidelberg, 2016).
- 14 Steele, B. C. H. & Heinzl, A. Materials for fuel-cell technologies. *Nature* **414**, 345 (2001).
- 15 Park, C. H. *et al.* Nanocrack-regulated self-humidifying membranes. *Nature* **532**, 480 (2016).
- 16 Mauritz, K. A. & Moore, R. B. State of Understanding of Nafion. *Chemical Reviews* **104**, 4535-4586 (2004).
- 17 Kerres, J. A. Development of ionomer membranes for fuel cells. *Journal of Membrane Science* **185**, 3-27 (2001).
- 18 Genorio, B. *et al.* Selective catalysts for the hydrogen oxidation and oxygen reduction reactions by patterning of platinum with calix[4]arene molecules. *Nature Materials* **9**, 998 (2010).
- 19 Debe, M. K. Electrocatalyst approaches and challenges for automotive fuel cells. *Nature* **486**, 43 (2012).
- 20 Raciti, D., Liu, Z., Chi, M. & Wang, C. Chapter 6 Recent Development of Platinum-Based Nanocatalysts for Oxygen Reduction Electrocatalysis in *Nanomaterials for Fuel Cell Catalysis* (eds Kenneth I. Ozoemena & Shaowei Chen) 253-280 (Springer International Publishing, 2016).
- 21 Greeley, J. *et al.* Alloys of platinum and early transition metals as oxygen reduction electrocatalysts. *Nature Chemistry* **1**, 552 (2009).
- 22 Ejikeme, P. M., Makgopa, K. & Ozoemena, K. I. Chapter 13 Effect of Support Materials on the Performance of Fuel Cells in *Nanomaterials for Fuel Cell Catalysis* (eds Kenneth I. Ozoemena & Shaowei Chen) 517-550

- (Springer International Publishing, 2016).
- 23 Sharma, S. & Pollet, B. G. Support materials for PEMFC and DMFC electrocatalysts—A review. *Journal of Power Sources* **208**, 96-119 (2012).
- 24 Dicks, A. L. The role of carbon in fuel cells. *Journal of Power Sources* **156**, 128-141 (2006).
- 25 Costamagna, P. & Srinivasan, S. Quantum jumps in the PEMFC science and technology from the 1960s to the year 2000: Part I. Fundamental scientific aspects. *Journal of Power Sources* **102**, 242-252 (2001).
- 26 Litster, S. & McLean, G. PEM fuel cell electrodes. *Journal of Power Sources* **130**, 61-76 (2004).
- 27 Lopez-Haro, M. *et al.* Three-dimensional analysis of Nafion layers in fuel cell electrodes. *Nature Communications* **5**, 5229 (2014).
- 28 US Department of Energy. *Parts of a Fuel Cell*,
<<https://www.energy.gov/eere/fuelcells/parts-fuel-cell>>
- 29 Alo, O. A., Otunniyi, I. O., Pienaar, H. & Iyuke, S. E. Materials for Bipolar Plates in Polymer Electrolyte Membrane Fuel Cell: Performance Criteria and Current Benchmarks. *Procedia Manufacturing* **7**, 395-401 (2017).
- 30 Rajeev, K. G., Soma, B. & Kamal, K. K. Bipolar Plate Materials for Proton Exchange Membrane Fuel Cell Application. *Recent Patents on Materials Science* **8**, 15-45 (2015).
- 31 Asri, N. F., Husaini, T., Sulong, A. B., Majlan, E. H. & Daud, W. R. W. Coating of stainless steel and titanium bipolar plates for anticorrosion in PEMFC: A review. *International Journal of Hydrogen Energy* **42**, 9135-9148 (2017).
- 32 Taherian, R. A review of composite and metallic bipolar plates in proton exchange membrane fuel cell: Materials, fabrication, and material selection. *Journal of Power Sources* **265**, 370-390 (2014).
- 33 Seh, Z. W. *et al.* Combining theory and experiment in electrocatalysis:

- Insights into materials design. *Science* **355** (2017).
- 34 Vidal-Iglesias, F. J., Solla-Gullón, J. & Feliu, J. M. Chapter 2 Recent Advances in the Use of Shape-Controlled Metal Nanoparticles in Electrocatalysis in *Nanomaterials for Fuel Cell Catalysis* (eds Kenneth I. Ozoemena & Shaowei Chen) 31-92 (Springer International Publishing, 2016).
- 35 Stephens, I. E. L., Rossmeisl, J. & Chorkendorff, I. Toward sustainable fuel cells. *Science* **354**, 1378-1379 (2016).

Chapter 2. Effect of Porous Metal Flow Field in Polymer Electrolyte Membrane Fuel Cell under Pressurized Condition

2.1. Introduction

Fuel cells are among the most promising powering devices owing to their relatively high fuel efficiency and almost zero emission. However, the components of fuel cells—e.g., the catalyst, gas diffusion layer (GDL), bipolar plate, and balance of plant (BOP)—are expensive, thereby limiting device commercialization. Moreover, the use of hydrogen as a fuel source poses several risks, such as high flammability and easy ignition. Hence, several research groups have been conducting experiments to improve the activity and durability of catalysts¹⁻⁶ to develop a stable, lightweight fuel cell system⁷⁻¹⁰ for resolving the safety issues associated with fuel cells,¹¹⁻¹³ and, most importantly, to facilitate the commercialization of fuel cells.

A bipolar plate is the most important component in PEFCs because it not only connects the anode and cathode electronically but also supplies H₂ and air/O₂ to the electrodes and removes the generated water. When fuel is supplied in the gas phase, the bipolar plate must have pathways or channels, referred to as the flow field. Generally, flow fields are carved on the bipolar plate with a depth of approximately 1 mm. Specifically, serpentine, column, and interdigitated hollow flow fields are commonly used in a PEFC, and experiments and computer-based simulations related to these flow fields have been reported.¹⁴⁻²² However, fuels mostly flow along the hollow channels and the GDLs are compressed by the flow field in the

assembled fuel cells, indicating that the electrical conductivity of GDL should increase because of better contact during compression, but the transport of gases (e.g., H₂ and air (O₂)) is hindered because of the decreased porosity and gas permeability of GDL.

Conventionally, compressed graphite has been used for bipolar plates in PEFCs, because of its chemical stability and moderate electric conductivity. However, despite the advantages of graphite, it is relatively heavyweight (approximately 80% of the total weight of a fuel cell stack) and brittle, and incurs high machining cost²³⁻²⁶. Hence, for fabricating a cost-effective, lightweight PEFC, the conventional bipolar plate must be replaced with low-cost, lighter materials while simultaneously maintaining the advantages of graphite. In this regard, several groups have been extensively researching materials to develop a new bipolar plate, e.g., a metal-based bipolar plate.^{19, 27, 28}

Metal foam materials have been applied to several fields, e.g., medicine, filter industries, and energy engineering, caused by their metallic properties and high porosities²⁹⁻³⁴. Recently, metal foam materials have also been utilized for energy devices, e.g., secondary batteries, water electrolyzers, and solar cells.³⁵⁻⁵⁰ Moreover, these materials have also been applied to fuel cells as a flow field, and most studies have reported better performance as compared with that observed for conventional materials.⁵¹⁻⁵⁶

Generally, the best performance of PEFCs is known to be achieved under completely humid conditions, caused by the sustained proton conductivity of Nafion (both ionomer and membrane).⁵⁷⁻⁶⁰ However, additional humidifiers are still required for the anode and cathode, in addition to temperature controllers, which must be set in the humidifiers to maintain RH conditions for fuel cell systems. Hence, several attempts have been reported to develop new components, e.g., membranes, catalyst layers, and GDLs, which can be applied under low RH operation.⁶¹⁻⁶⁷ Furthermore, using back-pressure devices, the fuel cell performance

is enhanced under pressured atmosphere as this condition renders advantages, such as increased exchange current density of the reaction, improved kinetics, and mass transfer.⁶⁸⁻⁷⁰

In this study, fuel cell tests using a metal foam flow field were conducted under different RH and pressurized conditions. In addition, the advantages of the metal foam flow field were confirmed by experiments.

2.2. Experimental section

2.2.1. Characterization of Metal Foam

A copper foam (PC-04, Alantum, Korea) was cut to an appropriate size ($\sim 1 \text{ cm}^2$). Scanning electron microscopy (SEM, JSM-6360 at the Research Institute of Advanced Materials) images were recorded for analyzing the morphology of the foam without any coatings. Energy-dispersive spectroscopy (EDS) mapping images were recorded to confirm the foam-containing elements. Mercury intrusion porosimetry (MIP) was employed to measure the porosity and average pore size of the foam.

2.2.2. Preparation of the Membrane Electrolyte Assembly

Pt/C (40 wt%, Alfa Aesar, USA) was dispersed in distilled water and isopropyl alcohol (Samchun Chemical, Korea) using a homogenizer (VCX130, Sonics & Materials, Inc., U.S.A.) with an amplitude of 30% for 3 min. A Nafion[®] solution (5 wt%, Sigma-Aldrich, U.S.A.) was added to the Pt/C solution and homogenized again for another 3 min. The ionomer content was 30 wt%. Proton exchange membranes (NR-212, DuPont, U.S.A.) with a thickness of 50 μm and an equivalent weight of 2100 were pretreated prior to fabrication with 1 M hydrogen peroxide (Daejung Chemicals & Metals Co., Ltd., Korea) and 1 M sulfuric acid (Samchun Chemical, Korea) at 80 $^{\circ}\text{C}$ for 1 h, followed by washing with deionized water. Membrane electrolyte assemblies (MEAs) were prepared by the catalyst-coated membrane (CCM) method. The pretreated membrane was fixed between two acrylic frames with a 5 cm^2 window, and the residual water on the membrane was blown out using an air compressor. Catalyst inks were added into a feed cup of a spray gun (Gun Piece GP-2, Richpen, Japan) and spread over the membrane. The active area of MEAs was 5 cm^2 , and the catalyst loading amount for the anode and cathode was 0.2 $\text{mg}_{\text{pt}} \text{cm}^{-2}$.

2.2.3. Single-Cell Tests

The prepared MEA was added into the center of the single cell, and GDLs (35BC, SGL Carbon, Germany) and Teflon gaskets were added to both sides of the MEA (Figure 2.1 (a)). In this study, two bipolar plates were applied to the single cells (CNL, Korea), and Figure 2.2 (a) and (b) shows schematic diagrams of MEA with a conventional flow field and metal foam flow field, respectively. First, two compressed graphite plates with a single serpentine flow field (channel width of 1 mm) (Figure 2.1 (b)) were prepared as a reference. The other set was graphite plates with no flow field with a rectangular parallelepiped (5 cm^2) empty space on one side, and it was filled with the metal foam (nickel and copper with the same porosity and pore size) (Figure 2.1 (c)). The depth of the two graphite plates was 1 mm. As the thickness of metal foams was greater than the depth of the space, these plates, which were processed to 5 cm^2 , were inserted into the hollow space of the bipolar plate, followed by compression from 1.6 mm to 1.0 mm using a presser (3850-0, Carver, U.S.A.) so that the plates can be precisely positioned at the depth of the plate. All other variables (total area of plate, current collectors, and cell assembly terminals) of the bipolar plate are the same except for the flow field area.

2.2.4. Electrochemical Measurements

The temperature of the single cell and humidifiers in the anode and cathode was maintained at $70 \text{ }^\circ\text{C}$, and the feed gas lines were enveloped by an insulator. H_2 and O_2 were supplied to the anode and cathode, respectively, at constant flow rates ($\text{H}_2:\text{O}_2 = 150 \text{ sccm}:200 \text{ sccm}$) for single-cell activation. For activation, the cell was operated in the open-circuit mode for 1 min, and the current was increased to 50 mA s^{-1} . When the current reached 5 A (1 A cm^{-2}), 10 A (2 A cm^{-2}), and 15 A (3 A cm^{-2}) at each value, it was maintained constant for 10 min. When the voltage was

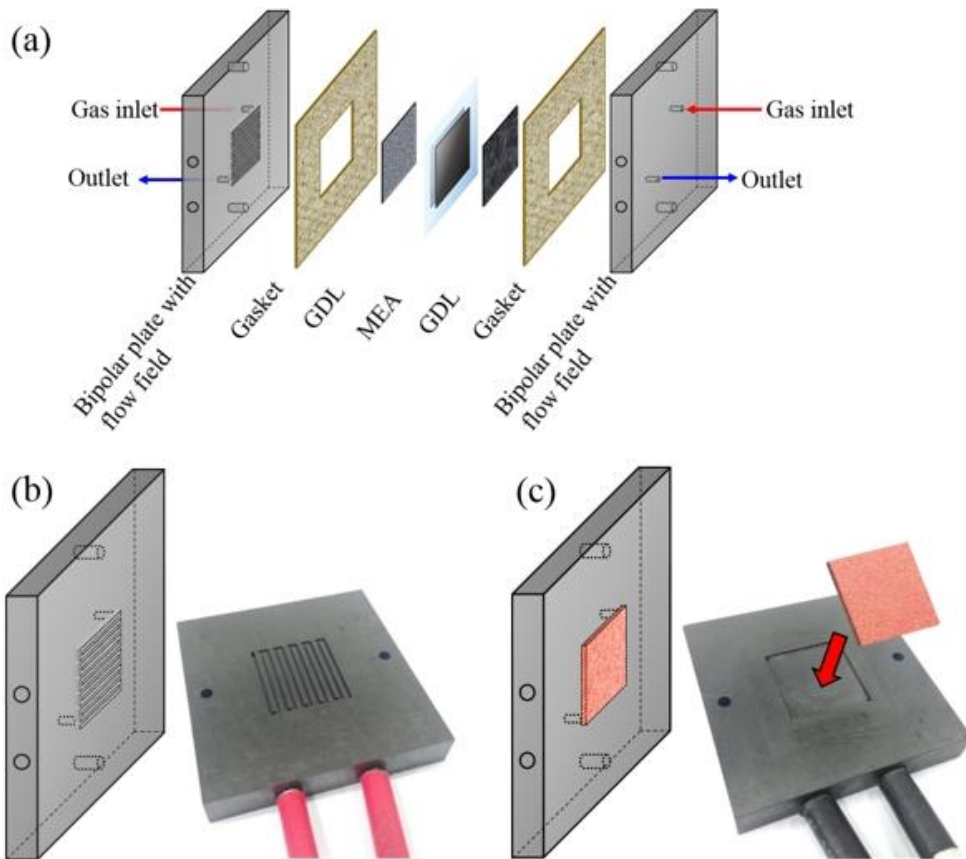


Figure 2.1 General components of a unit cell (a) and designed drawing and photograph of a bipolar plate with the serpentine flow field (b) and metal foam flow field (c).

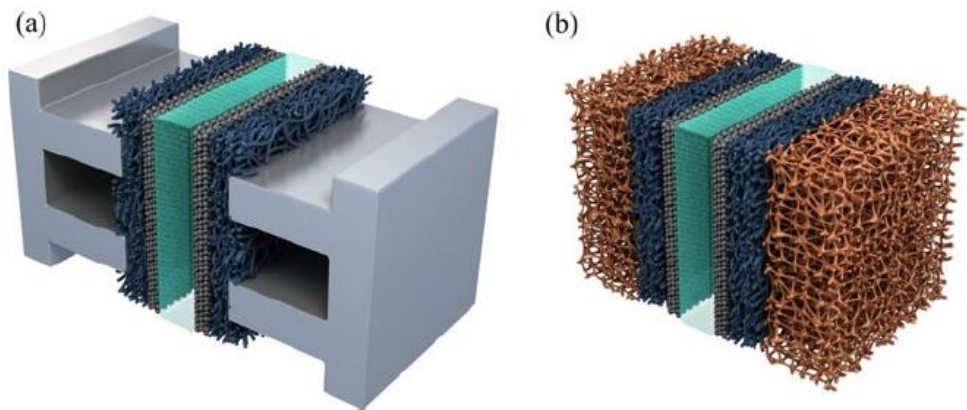


Figure 2.2 Schematic diagram of the MEA with conventional flow field (a) and metal foam flow field (b).

decreased to less than 0.37 V, no current was applied, and the voltage was recovered back to the open-circuit voltage (OCV).

The aforementioned process was repeated until both the current and power density did not increase any further. After activation, performance tests were conducted with a current load of 50 mA s⁻¹ without changing the gas species and flow rate (O₂, sccm). After 30 s at the OCV, the current was increased to obtain an *i*-*V* curve with a voltage limit of 0.35 V. Then, O₂ (cathode feed gas) was changed to air, and the gas stoichiometry for the anode and cathode was changed to 1.5:2.0. Electrochemical impedance spectroscopy (EIS) was employed to obtain single-cell resistances. From 100 kHz to 100 MHz, impedance was analyzed with an amplitude of 5 mV, and the measurement was repeated four times. The values were averaged for accuracy. For obtaining the electrochemical surface area (ECSA), cyclic voltammetry (CV) was conducted at a scan rate of 100 mV s⁻¹. The flow rates for the anode and cathode were 50 sccm (H₂) and 200 sccm (N₂), respectively. The temperature of the single cell was maintained at 30 °C, while that of the two humidifiers was maintained constant at 35 °C. EIS and CV were performed using the same device (Zennium, Zahner, Germany) in different modes.

2.2.5. Relative Humidity (RH) Tests

After measuring the initial performance under completely humid conditions, the performance at different values of relative humidity (20% to 100% RH) was analyzed. The temperature of the single cells was maintained at 70°C, while that of the two humidifiers was changed to investigate the effect of RH on the fuel cell performance with different flow fields. The temperatures of the humidifiers were maintained at 36.8, 50.2, 58.6, 64.9, and 70°C at 20, 40, 60, 80, and 100% RH, respectively. Before performance tests, cells were purged with dry N₂ for 10 min, and then a current density of 100 mA cm⁻² was applied for 10 min to attain the

same pre-testing conditions at the assigned RH. In addition, the performance was compared with that observed under the back-pressure condition (180 kPa). The RH values of the anode and cathode were measured using a humidity-temperature transmitter (HMT330, Vaisala, Finland).

2.3. Results and Discussion

2.3.1. Characteristics of Metal Foam Flow Fields

Figure 2.3 shows the application of the copper foam to the flow field in a unit cell, and Figure 2.3 (a)–(c) shows the SEM images of the pristine foam. The size of a single empty cell of the foam was approximately 450 μm , the cell pore size ranged from 50 to 250 μm . The cross-sectional morphology of the pristine foam (Figure 2.3 (c)) appeared very rough because of the physical cutting process, but its pore structure was in good agreement with its planar view. Figure 2.3 (d)–(e) shows the SEM images of the compressed metal foam to be applied as the flow field. The width and length of the metal foams were the same before and after compression, and the foams were only compressed in the height direction from 1.6 mm to 1.0 mm. Thus, the volume of the metal foam was reduced to 67.5% of its original volume. Although the cell and pore sizes were the same, the distance between the connected metal layers was closer than that in the pristine foam. The differences were clearly reflected in the cross-sectional image (Figure 2.3 (c) and (f)), related to the interconnected tube structure of this material, as well as the empty spaces present inside the metal tubes.

To estimate the porosity and average pore size of the pristine and compressed copper foams, MIP was employed. Figure 2.4 shows the results. The smaller pore (approximately 10 μm) and larger pore (approximately 100 μm) distribution corresponded to the inner and outer spaces of the metal tubes, respectively. Although the foam material was compressed, the average pore size of both foam materials was similar (~ 167 μm) to that of the pristine foam. In addition, no significant difference in the average porosities of these materials (only a 4.63% decrease from 87.13% to 78.50% after compression) was observed after compression.

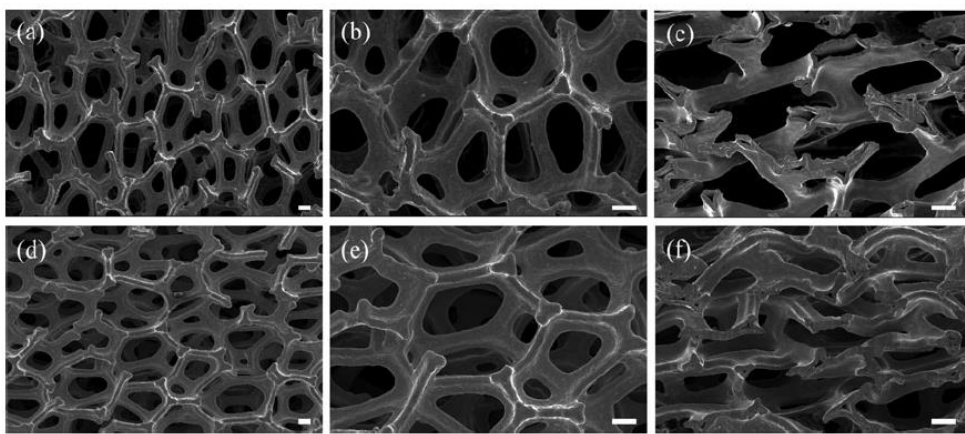


Figure 2.3. SEM images of the pristine copper metal foam (a)–(c) and compressed copper metal foam (d)–(e), Scale bar 100 μm . (c) and (f) represent cross-sectional images before and after compression.

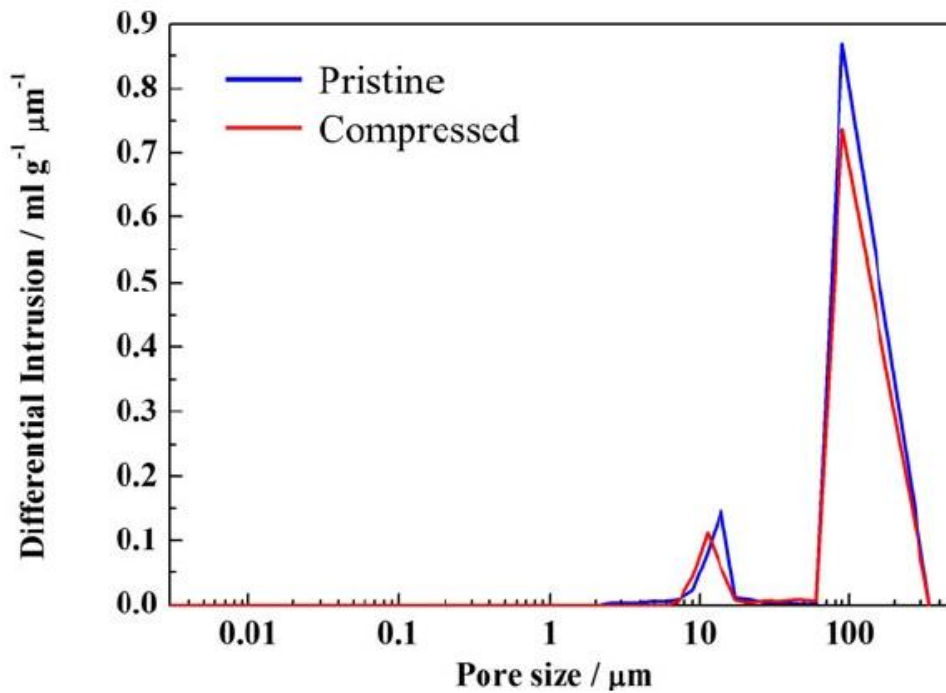


Figure 2.4. Pore distribution of the pristine (blue line, average pore size of 167.38 μm and 83.13% average porosity) and compressed metal foam (red line, average pore size of 167.08 μm and 78.50% average porosity) by mercury intrusion porosimetry.

2.3.2. Selection of Metal Foam Material for Flow Fields

Figure 2.5 shows the voltage profiles for single cells with three flow fields (graphite-based serpentine, nickel foam, and copper foam flow fields, respectively) during electrical activation. Because of the activation of single cells under O₂, the single-cell performance with the serpentine flow field (SCS) (Figure 2.5(a)) was stabilized approximately 6,000 s after activation. The single cell with the nickel foam flow field (SCNF) exhibited unstable performance even after 6,000 s when the conventional foam field was stabilized, and the stabilization did not occur even after 10,000 s (Figure 2.5 (b)). Stable single-cell performance was observed for the copper foam flow field (SCCF) (Figure 2.5 (c)) after approximately 2,000 s. Under the same conditions except for the flow field, different profiles were observed for the unit-cell performance; this difference is thought to be related to the fact that the properties of the flow field material affect the performance stabilization of fuel cells as nickel can not only undergo facile corrosion but also dissolve under acidic, and relatively high-temperature conditions.⁷¹ Tseng *et al.*⁵⁵ have reported low performance for a unit cell comprising a nickel foam as a flow distributor. To overcome this limitation, the porous nickel surface was treated with polytetrafluoroethylene (PTFE). The unit cell with the treated nickel foam exhibits improved fuel cell performance. On the other hand, stable performance was attained with the use of the Cu foam, and even stable performance was attained at a more rapid rate as compared with that observed for the conventional foam. Hence, the following experiments are conducted with an SCCF.

2.3.3. Electrochemical Performance

After activation, unit cells were supplied with air instead of O₂, and the RH was fixed at 100%. Figure 2.6 (a) shows the results obtained from the polarization curve of two PEM fuel cells. At 0.6 V, the current densities were 1,060 mA cm⁻² and 969 mA cm⁻² for SCS and SCCF, respectively. Their corresponding power dens

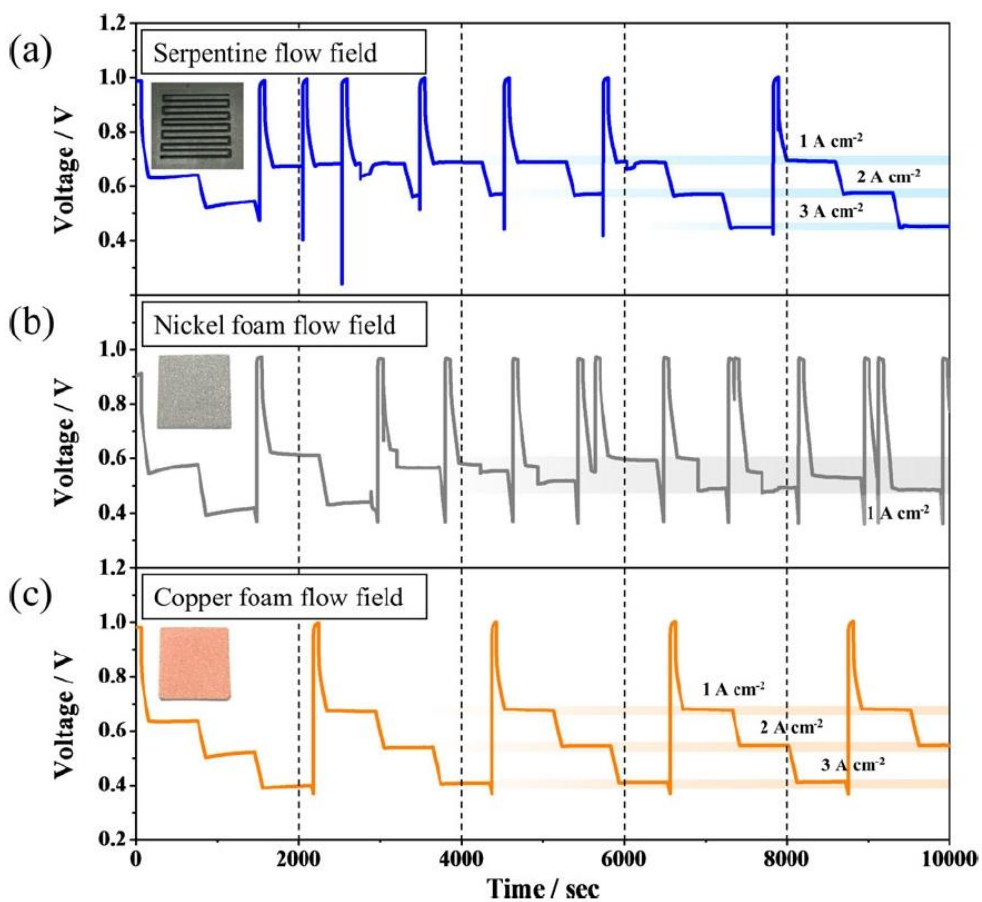


Figure 2.5 Voltage profiles of single cells with (a) the conventional serpentine (b) nickel foam, and (c) copper foam flow fields during activation. The inset shows pictures of each flow field. The temperatures of the single cells and all humidifiers were maintained 70°C (100% RH) during this process without backpressure, and H₂ and O₂ were supplied to the anode and cathode at a constant flow of 150 and 200 sccm, respectively.

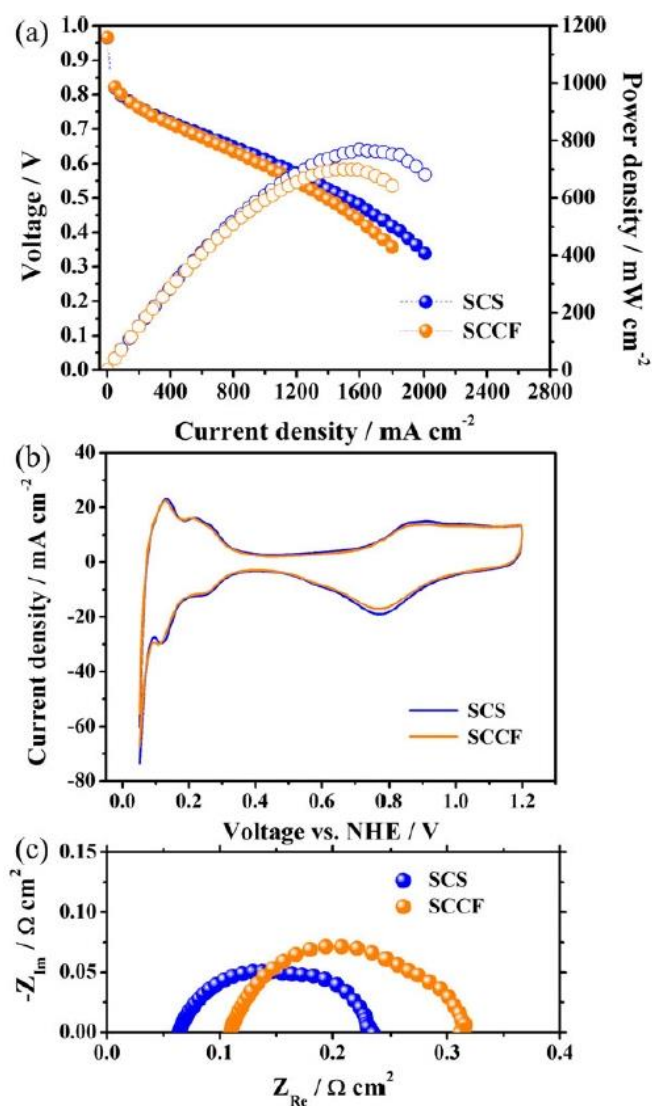


Figure 2.6 Results from (a) the polarization curve, (b) CV and (c) EIS with single cells with SCF and SCCF. For polarization curves and EIS results, the temperatures of the cell and humidifier were maintained at 70°C (100% RH), and H₂ and air were supplied with a stoichiometry of 1.5:2.0 to the anode and cathode, respectively. For CV measurements, the temperatures of the cell (30°C) and humidifiers (35°C) were maintained constant. H₂ and N₂ were supplied to the anode and cathode at constant flow rates of 50 and 200 sccm, respectively.

-ities at 0.6 V were 638 mW cm⁻² and 581 mW cm⁻², respectively. The maximum power densities for the conventional and porous channels were 771 mW cm⁻² and 702 mW cm⁻², respectively. When normalized to the amount of Pt applied to both the cathode and anode, the specific power density values were 1.93 kW g_{Pt}⁻¹ and 1.76 kW g_{Pt}⁻¹ for SCS and SCCF, respectively. Table 2.1 summarizes these results. Although similar performance was observed in the low-current-density region, gradual decrease in the performance was observed for SCCF as compared to SCS at current densities greater than equal to approximately 400 mA cm⁻². As a result, different performance from that expected is observed: improved performance is observed because of the advantage of mass transfer, caused by the structural characteristics of the porous metal flow field.

Figure 2.6 (b) shows the results obtained from the CV measurement of two unit cells under H₂/N₂. The ECSA values calculated from the hydrogen adsorption area from CV were 59.67 m² g⁻¹ and 59.83 m² g⁻¹ for SCS and SCCF, respectively. Because EAS is predominantly determined by the loading amount of the catalyst (platinum) in the fuel cell electrode, similar ECSA values are thought to be obtained with the use of the same loading amount of platinum for two unit cells. For further analysis, EIS was conducted. Figure 2.6 (c) shows the results obtained. The ohmic resistance values were 0.0641 Ω cm² and 0.1103 Ω cm² for SCS and SCCF, respectively. High-frequency impedance represents the ohmic resistance (electrical contact resistance and proton conducting membrane resistance) of the fuel cell components; this resistance is often referred to as membrane resistance as the proton resistance of membranes predominantly contributes to the total ohmic resistance.⁷² Although identical operation conditions were utilized, as well as single cell components, except for the flow field, higher ohmic resistance (R_{Ω}) values were observed for SCCF as compared to SCS, possibly related to the oxidation of copper under the fuel-cell operation environment. Generally, a PEFC is

Table 2.1 Electrochemical properties of fuel cell with the serpentine and porous flow fields. For the polarization curve and EIS results, the temperatures of the cell and humidifier were maintained 70°C (100% RH), and H₂ and air were supplied with a stoichiometry of 1.5:2.0 to the anode and cathode, respectively. For CV measurements, the temperatures of the cell (30°C) and humidifiers (35°C) were maintained constant. H₂ and N₂ were supplied to the anode and cathode at constant flow rates of 50 and 200 sccm, respectively.

	Current Density at 0.6 V/ mA cm ⁻²	Maximum Power density/ mW cm ⁻²	Power Density/ kW g _{pt} ⁻¹	ECSA/m ² g ⁻¹	Ohmic Resistance/ Ω cm ²	Charge Resistance/ Ω cm ²
SCS	1,060	771	1.93	59.67	0.0641	0.1667
SCCF	969	702	1.76	59.83	0.1103	0.2048

operated under acidic environment, caused by the effect of hydrogen ions and generated water; hence, metal corrosion occurs easily. In addition, the charge-transfer resistance of the cell ($R_{ct} = 0.2048 \Omega \text{ cm}^2$) for SCCF was slightly greater than that for SCS ($R_{ct} = 0.1667 \Omega \text{ cm}^2$), and this result supported the lower performance as compared with that observed for the conventional cell in the polarization curve (Figure 2.6 (a)).

2.3.4. Analysis of Porous Flow Field Corrosion and Fuel Cell Performance Before and After Single-Cell Operation

During the application of copper to flow fields of fuel cells, copper is easily oxidized by the acidic conditions under which PEFC is operated. Hence, the elements of the flow field are examined before and after the fuel-cell operation, and electrical stability is also confirmed (Figure 2.7). Initially, the foam was composed of 100.00 wt% copper (Figure 2.7 (a)), with no oxides. However, after activation and electrochemical tests, copper oxide was observed (Cu, 89.07 wt% and O, 10.93 wt%). Tang et al.⁷³ have reported the corrosion and electrical resistance of copper fibers for the anode/cathode (half-cell) condition and contact mode, respectively. In addition, they have confirmed the feasibility of using porous materials for the flow field in a bipolar plate. To investigate the effect of this foam on the electrochemical stability of the fuel cell, a constant voltage (0.63 V) was applied to the cell. Figure 2.7 (c) shows the result. Initially, the current density increased, but it fairly stabilized after approximately 100 s. Hence, although the copper foam is oxidized after the fuel-cell operation, oxidation is not considered to proceed beyond a certain percentage based on this result. In addition, because of the interconnected structure of the metal foam, no issues related to the electric conductivity were considered once the oxide film was formed on the surface based on this constant voltage test.

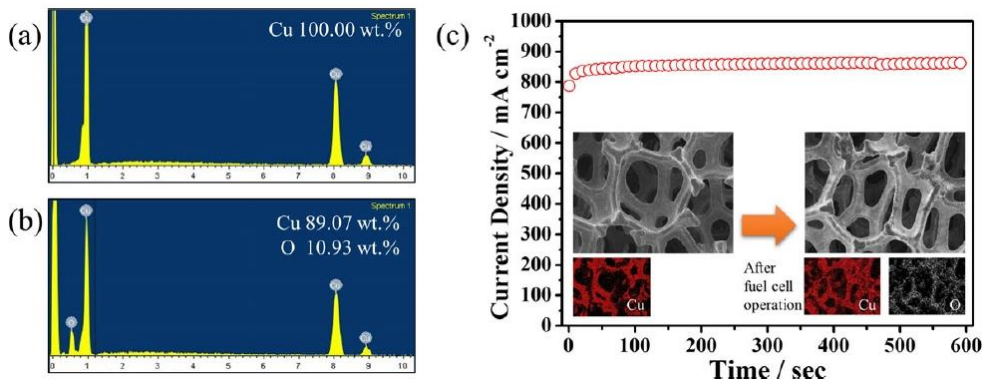


Figure 2.7 EDS spectra of the copper foam (a) before and (b) after single-cell operation, and (c) current density profile of SCCF in the constant voltage mode (inset: EDS mapping images before and after fuel-cell operation). For the constant voltage (0.63 V) test, the temperatures of the single cell and all humidifiers were maintained at 70°C (100% RH) during this process without backpressure, and H₂ and air were supplied to the anode and cathode at constant flow rates of 150 and 200 sccm, respectively.

To understand the manner in which the porous structure affects the metal flow field, the performance curve of the metal foam was reconstructed by the correction of the differences in the high-frequency resistance (HFR) values of SCS and SCCF ($HFR_{(SCCF)} - HFR_{(SCS)}$) (Figure 2.8). The corrected performance curve of the fuel cell with the metal foam flow field exhibited performance similar to that of SCS. The current density at 0.5–0.7 V, which is mainly utilized for practical fuel cell applications, was slightly greater than that of SCCF. However, by the application of metal foam, no significant performance improvement was observed. In addition, the performance reduction in the high-current-density region was greater than that observed for the conventional foam as the porous flow field was expected to exhibit a significant performance improvement in the mass-transfer-resistance region. Hence, no advantages related to the application of the porous metal flow field are observed under the current experimental conditions.

2.3.5. Performance Evaluation with Different Values of the Relative Humidity of Supply Gas

During the application of the porous flow field, the effect caused by the water generated in the reaction is considered greater than that observed for the conventional flow field. To overcome this phenomenon, the RH of the feed gas was reduced from 100 to 20%, and the performance at each RH is summarized in Table 2.2. Figure 2.9 shows the results obtained. At 80% RH, the results were similar to those obtained at 100% RH (Figure 2.6 (a)) (similar performance in the low-current region, and gradually lower performance was observed toward the high-current region). At 60% RH, the performance in the low-current region was slightly less than that observed for the conventional flow field, but opposite behavior was observed at a current density greater than 1,400 mA cm⁻². However, at 40% RH, the performance of SCS was less than or equal to that of SCCF. The performance of SCCF was less than that of SCS even at 20% RH, and the performance

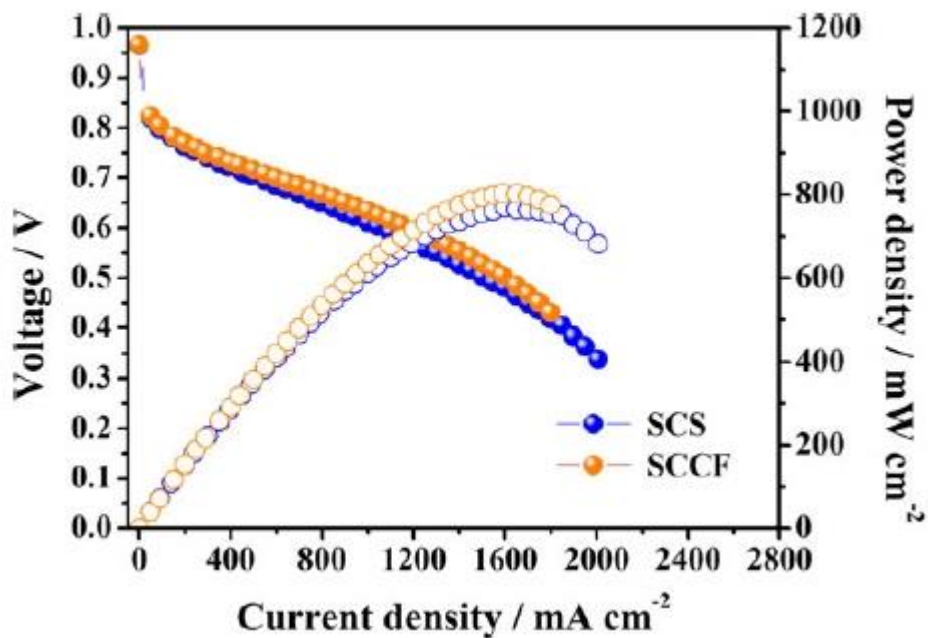


Figure 2.8 Polarization curve of fuel cells with SCS and the partially corrected curve of SCCF. For this performance curve, the temperatures of the cell and humidifier were maintained at 70°C (100% RH), and H₂ and air were supplied with a stoichiometry of 1.5:2.0 to the anode and cathode, respectively.

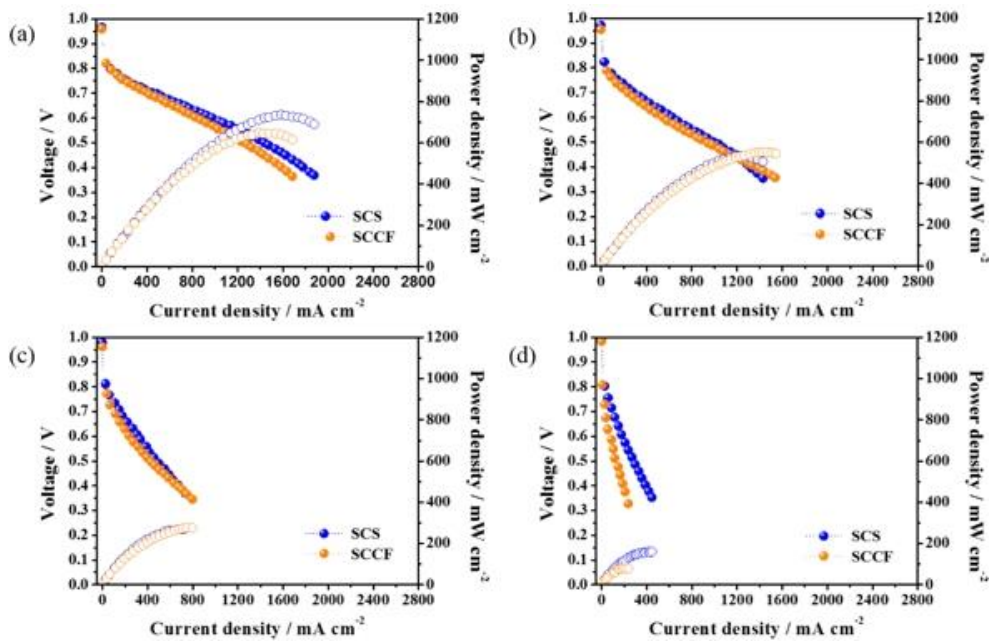


Figure 2.9 Polarization curve for SCS and SCCF with various relative humidity (a) RH80, (b) RH60, (c) RH 40, and (d) RH 20 at atmospheric condition

Table 2.2 Summary of performance of SCS and SCCF at atmospheric condition.

	SCS		SCCF	
	Current Density at 0.6 V/mA cm ⁻²	Max. Power Density/mW cm ⁻²	Current Density at 0.6 V/mA cm ⁻²	Max. Power Density/mW cm ⁻²
RH20	180	159	84	79
RH40	310	275	249	276
RH60	627	535	546	553
RH80	975	738	849	649
RH100	1,069	771	969	702

difference was greater than that at 40% RH, related to the dehydration of the membrane and electrode caused by the introduction of the fuel from the outside with low humidity. In addition, as the metal foam exhibited high porosity per area, dehydration is considered to occur to a greater extent in SCCF; as a result, lower performance is observed. Under the above experimental conditions, it is difficult to explain the specific advantages of the porous flow field. Hence, experimental conditions with the advantage of applying the highly porous structure to the flow field need to be examined.

2.3.6. Performance Evaluation under Pressurized Atmosphere

Tsai *et al.* [56] have reported that the mainstream of supplied gases flows in a diagonal direction with the passage of the gas through the metal foam; thus, the non-uniform distribution of gas is observed because of the characteristics of the foam, e.g., high porosity, large pore size, and open structure of the metal foam. In other words, gases are not sufficiently supplied to some parts of the electrode (non-mainstream region), e.g., dead zone. Hence, their group has designed a new plate for better gas flow. However, this strategy requires a delicate process to manufacture bipolar plate. As a result, for the uniform distribution of the reactant, a backpressure method was applied, which involves the application of a specific pressure to the outlet of the fuel cell to increase the efficiency via the increase of the partial pressure of the fuel. To investigate the structural effects of porous metals, partially corrected data, such as atmospheric conditions of 100% RH (Figure 2.8), are shown in Figure 2.10. (Figure 2.11 shows the performance curve before correction.) In the low-current-density region, the performance of SCCF was slightly greater than, or the same as, that of SCS. However, at a current density greater than $1,800 \text{ mA cm}^{-2}$, the voltage of SCCF abruptly decreased. This result is somewhat different from that expected by the application of a porous flow field.

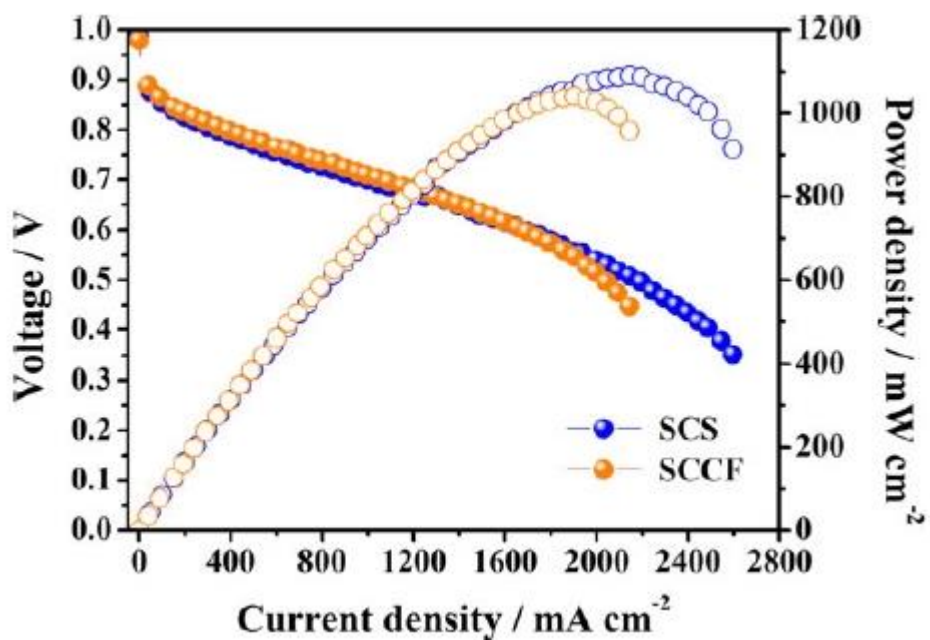


Figure 2.10 Performance curve of SCS and partially corrected curve of SCCF under backpressure condition (180 kPa) at 100% RH. For this performance curve, the temperatures of the cell and humidifier were maintained at 70°C, and H₂ and air were supplied with a stoichiometry of 1.5:2.0 to the anode and cathode, respectively.

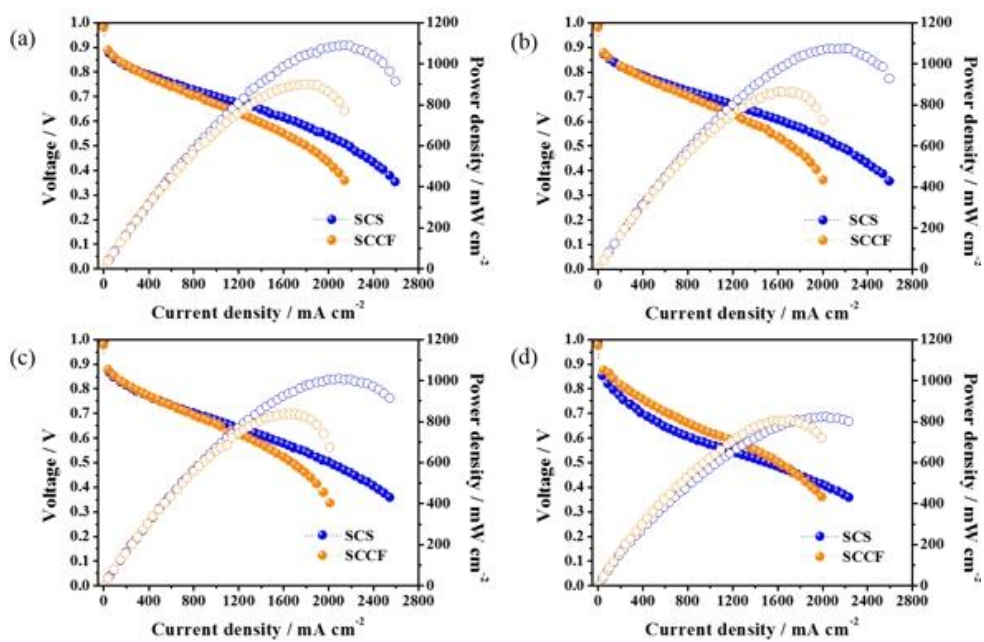


Figure 2.11 Polarization curve for SCS and SCCF with various relative humidity
 (a) RH100, (b) RH 80, (c) RH 60, and (d) RH 40 at pressurized condition

The decreased performance is thought to be caused by the increase of the mass-transfer resistance, related to the water generated during the reaction at high current density. Hence, as observed under atmospheric pressure conditions, the experiment is carried out with the relative humidity lowered to adjust the absolute amount of the liquid in the cell, and the performance at each RH is summarized in Table 2.3. Figure 2.11 shows the result obtained. At 80% RH, the performance decrease of SCCF was greater than that of SCS. At 60% RH, the reduction in the performance of SCCF was less than that of SCS as compared to the result obtained at 80% RH. At 40% RH, the performance of SCS decreased in the low-current-density region. This result is possibly related to the fact that not only low amounts of water are present in the fuel itself but also low amounts of water are produced by the reaction, hindering the transfer of hydrogen ions in the electrode and rapidly decreasing the performance. On the other hand, at 40% RH, SCCF did not exhibit a large reduction in performance as compared with that observed at 60% RH. Figure 2.12 (non-corrected) shows the i - V curve of two single cells at 20% RH. At 0.6 V, the current density and maximum power density for SCCF were 2 times less than that observed for SCS, and the absolute current values for both cells were extremely low, caused by the low proton conductivity under atmospheric conditions (Figure 2.9 (d)). However, under the back-pressure condition, the current density of SCCF at 0.6 V was superior to that of SCS (Table 2.4). Therefore, during the application of the flow field with a porous structure under low humidity and pressurized conditions, superior performance was observed as compared with that observed for the conventional flow field because the foam structure exhibits several pores, which is a material characteristic; hence, the H₂O originating from the gas and that generated by the reaction are considered to be stored in the pores of the porous flow field, caused by the capillary action,⁷⁴ and the fuel with low RH is added to humidification from the water remaining in the pore to help improve the fuel cell performance. Therefore, the residual liquid water is considered to interfere with

Table 2.3 Summary of performance of SCS and SCCF at pressurized condition.

	SCS		SCCF	
	Current Density at 0.6 V/mA cm ⁻²	Max. Power Density/mW cm ⁻²	Current Density at 0.6 V/mA cm ⁻²	Max. Power Density/mW cm ⁻²
RH20	329	405	982	822
RH40	833	823	1,123	809
RH60	1,468	1,011	1,293	842
RH80	1,647	1,075	1,333	867
RH100	1,688	1,090	1,363	903

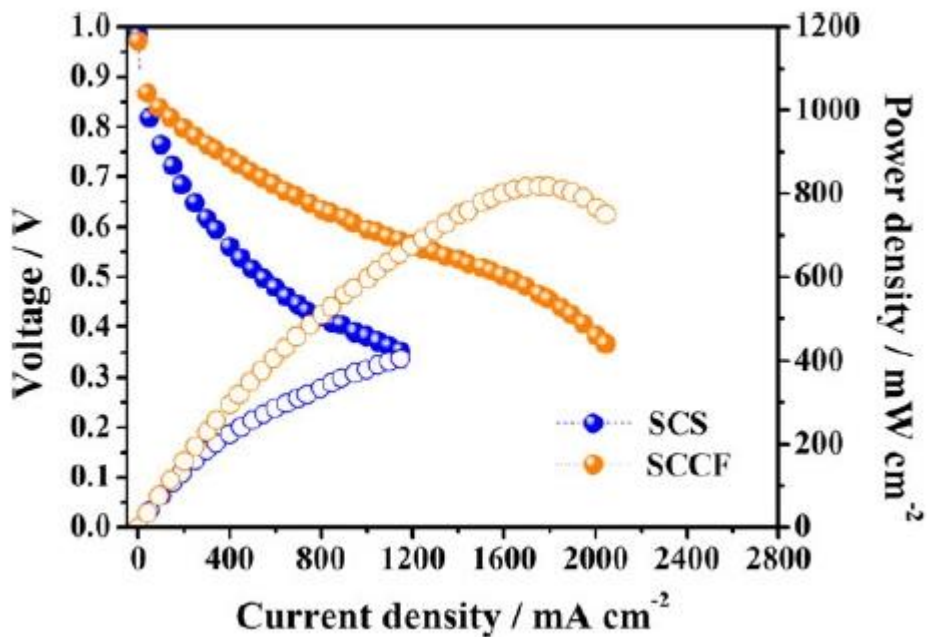


Figure 2.12 Polarization curve of SCS and non-corrected curve of SCCF under pressurized condition (180 kPa) at 20% RH. For this performance curve, the temperatures of the cell (70°C) and humidifier (36.8°C) were maintained constant, and H₂ and air were supplied with a stoichiometry of 1.5:2.0 to the anode and cathode, respectively.

Table 2.4 Current density at 0.6 V and the maximum power density of single cells at 20% RH under atmospheric pressure and pressurized conditions (180 kPa). For this performance curve, the temperatures of the cell (70°C) and humidifier (36.8°C) were maintained constant, and H₂ and air were supplied with a stoichiometry of 1.5:2.0 to the anode and cathode, respectively.

	Atmospheric condition		Backpressure condition	
	Current Density at 0.6 V/mA cm ⁻²	Maximum Power Density/mW cm ⁻²	Current Density at 0.6 V/mA cm ⁻²	Maximum Power Density/mW cm ⁻²
SCS	180	159	329	405
SCCF	84	79	982	822

dehydration, related to the capillary action under pressurized conditions, even if the water from the electrode side is subjected to dehydration by the inflow fuel with low humidity. Hence, the foam is considered to act as a humidifier, and the schematic diagram is shown in Figure 2.13. For this reason, during the application of the foam material to the flow field, the entire fuel cell system could be simplified by the removal or reduction of humidifiers. However, despite the structural advantages of the metal foams mentioned above, there is room to improve the performance decrease caused by the oxidation of the metal under the operating conditions of the fuel cell by further studies, e.g., treatment of surfaces and alloying of foam material.

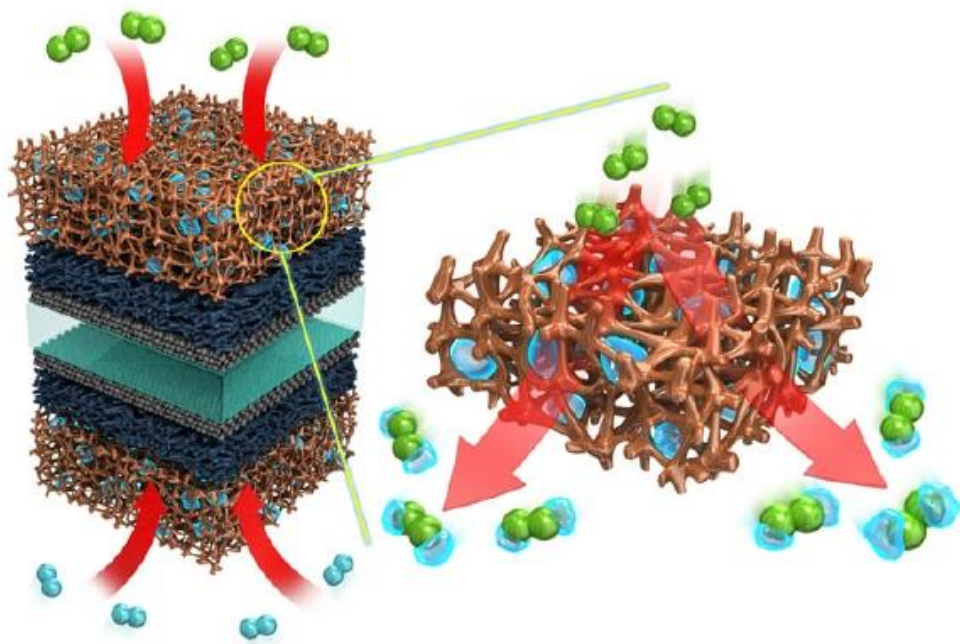


Figure 2.13 Schematic diagram of the metal foam flow field under low RH and pressurized conditions.

2.4. Conclusions

In this study, the effects of the structure of the metal foam as a fuel cell flow field were investigated. From the results obtained for the experiment under normal pressure and 100% RH, better performance for the conventional serpentine flow field (771 mW cm^{-2}) was observed as compared with that observed with the metal foam in the cell (702 mW cm^{-2}), caused by metal oxidation, as well as the decreased performance of the fuel cell related to the increased contact resistance. For compensating the effect of metal oxidation, the performance was similar to that of the conventional one, but the performance drastically decreased in the high-current-density region. To investigate the effect of water, experiments were conducted under low-humidity conditions, but no improvement in performance was observed. To compensate the disadvantages of the porous structure as the flow field, and to uniformly distribute the reactant gas, the experiment was conducted under pressurized conditions. Performance similar to that observed under atmospheric conditions was observed at 100% RH in the low-current-density region, with drastic performance reduction in the high-current-density region. However, high performance was observed under low RH conditions. Hence, the porous flow field exhibits favorable effects under pressurized and low-humidity conditions, considered to be caused by the characteristics of porous materials, such as the capillary phenomenon. Furthermore, better results are expected to be obtained with further research via surface treatment and/or material changes because preventing material corrosion is an important issue in selecting materials for fuel cell components, and it is necessary to use materials that are stable material under fuel cell operating conditions.

2.5. References

- 1 Chen, C. *et al.* Highly crystalline multimetallic nanoframes with three-dimensional electrocatalytic surfaces. *Science* **343**, 1339-1343 (2014).
- 2 Chung, D. Y. *et al.* Highly Durable and Active PtFe Nanocatalyst for Electrochemical Oxygen Reduction Reaction. *Journal of the American Chemical Society* **137**, 15478-15485 (2015).
- 3 Stephens, I. E. L., Bondarenko, A. S., Grønbyerg, U., Rossmeisl, J. & Chorkendorff, I. Understanding the electrocatalysis of oxygen reduction on platinum and its alloys. *Energy and Environmental Science* **5**, 6744-6762 (2012).
- 4 Wu, J. & Yang, H. Platinum-based oxygen reduction electrocatalysts. *Accounts of Chemical Research* **46**, 1848-1857 (2013).
- 5 Zhang, L. *et al.* Platinum-based nanocages with subnanometer-thick walls and well-defined, controllable facets. *Science* **349**, 412-416 (2015).
- 6 Zhou, Y. *et al.* Enhancement of Pt and Pt-alloy fuel cell catalyst activity and durability via nitrogen-modified carbon supports. *Energy and Environmental Science* **3**, 1437-1446 (2010).
- 7 Gamburgzev, S. & Appleby, A. J. Recent progress in performance improvement of the proton exchange membrane fuel cell (PEMFC). *Journal of Power Sources* **107**, 5-12 (2002).
- 8 Lee, C.-H., Lee, Y.-B., Kim, K.-M., Jeong, M.-G. & Lim, D.-S. Electrically conductive polymer composite coating on aluminum for PEM fuel cells bipolar plate. *Renewable Energy* **54**, 46-50 (2013).
- 9 Nam, S., Lee, D., Kim, J. & Lee, D. G. Development of the light weight carbon composite tie bar. *Composite Structures* **134**, 124-131 (2015).
- 10 Wang, S.-H., Lui, W.-B., Peng, J. & Zhang, J.-S. Performance of the Iridium Oxide (IrO₂)-Modified Titanium Bipolar Plates for the Light Weight Proton Exchange Membrane Fuel Cells. *Journal of Fuel Cell*

- Science and Technology* **10**, 041002-041002-041006 (2013).
- 11 Collong, S. & Kouta, R. Fault tree analysis of proton exchange membrane fuel cell system safety. *International Journal of Hydrogen Energy* **40**, 8248-8260 (2015).
 - 12 Gerbec, M., Jovan, V. & Petrovčič, J. Operational and safety analyses of a commercial PEMFC system. *International Journal of Hydrogen Energy* **33**, 4147-4160 (2008).
 - 13 Yu, S. & Jung, D. Thermal management strategy for a proton exchange membrane fuel cell system with a large active cell area. *Renewable Energy* **33**, 2540-2548 (2008).
 - 14 Antuñano, M. A. Z. *et al.* Fuel Pressure Distribution as a Criterion for the Bipolar Plate Geometry Optimization in PEM Fuel Cells, Modeling and Experiment. *Fuel Cells* **15**, 639-645 (2015).
 - 15 Barreras, F., Lozano, A., Valiño, L., Marín, C. & Pascau, A. Flow distribution in a bipolar plate of a proton exchange membrane fuel cell: experiments and numerical simulation studies. *Journal of Power Sources* **144**, 54-66 (2005).
 - 16 Debe, M. K. & Herdtle, T. Design and Development of a Novel Flow Field for PEM Fuel Cells to Obtain Uniform Flow Distribution. *ECS Transactions* **1**, 581-604 (2006).
 - 17 Han, S.-H., Choi, N.-H. & Choi, Y.-D. Simulation and experimental analysis on the performance of PEM fuel cell by the wave-like surface design at the cathode channel. *International Journal of Hydrogen Energy* **39**, 2628-2638 (2014).
 - 18 Kwon, O. J. *et al.* Development of flow field design of polymer electrolyte membrane fuel cell using in-situ impedance spectroscopy. *International Journal of Hydrogen Energy* **36**, 9799-9804 (2011).
 - 19 Li, X. & Sabir, I. Review of bipolar plates in PEM fuel cells: Flow-field

- designs. *International Journal of Hydrogen Energy* **30**, 359-371 (2005).
- 20 Mehrpooya, M., Kheir Rouz, M. & Nikfarjam, A. Optimum Design of the Flow-Field Channels and Fabrication of a Micro-PEM Fuel Cell. *Industrial & Engineering Chemistry Research* **54**, 3640-3647 (2015).
- 21 Saripella, B. P., Koylu, U. O. & Leu, M. C. Experimental and Computational Evaluation of Performance and Water Management Characteristics of a Bio-Inspired Proton Exchange Membrane Fuel Cell. *Journal of Fuel Cell Science and Technology* **12**, 061007-061007-061009 (2015).
- 22 Sousa, T., Mamlouk, M., Scott, K. & Rangel, C. M. Three Dimensional Model of a High Temperature PEMFC. Study of the Flow Field Effect on Performance. *Fuel Cells* **12**, 566-576 (2012).
- 23 Bhlapibul, S. & Pruksathorn, K. Preparation of graphite composite bipolar plate for PEMFC. *Korean Journal of Chemical Engineering* **25**, 1226-1231 (2008).
- 24 Shimpalee, S. *et al.* Investigation of bipolar plate materials for proton exchange membrane fuel cells. *International Journal of Hydrogen Energy* **41**, 13688-13696 (2016).
- 25 Taherian, R. & Nasr, M. Performance and material selection of nanocomposite bipolar plate in proton exchange membrane fuel cells. *International Journal of Energy Research* **38**, 94-105 (2014).
- 26 Wang, J. & Wang, H. Flow-Field Designs of Bipolar Plates in PEM Fuel Cells: Theory and Applications. *Fuel Cells* **12**, 989-1003 (2012).
- 27 Taherian, R. A review of composite and metallic bipolar plates in proton exchange membrane fuel cell: Materials, fabrication, and material selection. *Journal of Power Sources* **265**, 370-390 (2014).
- 28 Wang, H. & Turner, J. A. Reviewing Metallic PEMFC Bipolar Plates. *Fuel Cells* **10**, 510-519 (2010).

- 29 Bansiddhi, A., Sargeant, T. D., Stupp, S. I. & Dunand, D. C. Porous NiTi for bone implants: A review. *Acta Biomaterialia* **4**, 773-782 (2008).
- 30 Jin, X. *et al.* Bio-Inspired Multifunctional Metallic Foams Through the Fusion of Different Biological Solutions. *Advanced Functional Materials* **24**, 2721-2726 (2014).
- 31 Lefebvre, L. P., Banhart, J. & Dunand, D. C. Porous Metals and Metallic Foams: Current Status and Recent Developments. *Advanced Engineering Materials* **10**, 775-787 (2008).
- 32 Singh, R., Lee, P. D., Dashwood, R. J. & Lindley, T. C. Titanium foams for biomedical applications: a review. *Materials Technology* **25**, 127-136 (2010).
- 33 Stergioudi, F. *et al.* Copper foams in water treatment technology: Removal of hexavalent chromium. *Materials & Design* **87**, 287-294 (2015).
- 34 Wen, C. E. *et al.* Novel titanium foam for bone tissue engineering. *Journal of Materials Research* **17**, 2633-2639 (2002).
- 35 Nam, D.-H., Kim, R.-H., Lee, C.-L. & Kwon, H.-S. Highly Reversible Sn-Co Alloy Anode Using Porous Cu Foam Substrate for Li-Ion Batteries. *Journal of The Electrochemical Society* **159**, A1822-A1826 (2012).
- 36 Feng, N. *et al.* Growth of nanostructured nickel sulfide films on Ni foam as high-performance cathodes for lithium ion batteries. *Physical Chemistry Chemical Physics* **15**, 9924-9930 (2013).
- 37 Choi, H. *et al.* Next-Generation Polymer-Electrolyte-Membrane Fuel Cells Using Titanium Foam as Gas Diffusion Layer. *ACS Applied Materials & Interfaces* **6**, 7665-7671 (2014).
- 38 Jing, S., Jiang, H., Hu, Y. & Li, C. Graphene supported mesoporous single crystal silicon on Cu foam as a stable lithium-ion battery anode. *Journal of Materials Chemistry A* **2**, 16360-16364 (2014).
- 39 Li, W. Q., Qu, Z. G., He, Y. L. & Tao, Y. B. Experimental study of a

- passive thermal management system for high-powered lithium ion batteries using porous metal foam saturated with phase change materials. *Journal of Power Sources* **255**, 9-15 (2014).
- 40 Mazouzi, D. *et al.* Very High Surface Capacity Observed Using Si Negative Electrodes Embedded in Copper Foam as 3D Current Collectors. *Advanced Energy Materials* **4**, 1301718-n/a (2014).
- 41 Park, S. H. *et al.* Nickel-nitride-coated nickel foam as a counter electrode for dye-sensitized solar cells. *Surface and Coatings Technology* **259**, Part C, 560-569 (2014).
- 42 Zhang, Q. *et al.* Growth of Hierarchical 3D Mesoporous NiSix/NiCo2O4 Core/Shell Heterostructures on Nickel Foam for Lithium-Ion Batteries. *ChemSusChem* **7**, 2325-2334 (2014).
- 43 Chen, G., Yang, J., Tang, J. & Zhou, X. Hierarchical NiCo2O4 nanowire arrays on Ni foam as an anode for lithium-ion batteries. *RSC Advances* **5**, 23067-23072 (2015).
- 44 Tang, C., Cheng, N., Pu, Z., Xing, W. & Sun, X. NiSe Nanowire Film Supported on Nickel Foam: An Efficient and Stable 3D Bifunctional Electrode for Full Water Splitting. *Angewandte Chemie International Edition* **54**, 9351-9355 (2015).
- 45 Zhao, Q. *et al.* Sulfur Nanodots Electrodeposited on Ni Foam as High-Performance Cathode for Li-S Batteries. *Nano Letters* **15**, 721-726 (2015).
- 46 Sivanantham, A., Ganesan, P. & Shanmugam, S. Hierarchical NiCo2S4 Nanowire Arrays Supported on Ni Foam: An Efficient and Durable Bifunctional Electrocatalyst for Oxygen and Hydrogen Evolution Reactions. *Advanced Functional Materials* **26**, 4661-4672 (2016).
- 47 Um, J. H. *et al.* 3D macroporous electrode and high-performance in lithium-ion batteries using SnO2 coated on Cu foam. *Scientific Reports* **6**, 18626 (2016).

- 48 You, B., Jiang, N., Sheng, M., Bhushan, M. W. & Sun, Y. Hierarchically Porous Urchin-Like Ni₂P Superstructures Supported on Nickel Foam as Efficient Bifunctional Electrocatalysts for Overall Water Splitting. *ACS Catalysis* **6**, 714-721 (2016).
- 49 Zhu, W. *et al.* Nickel sulfide microsphere film on Ni foam as an efficient bifunctional electrocatalyst for overall water splitting. *Chemical Communications* **52**, 1486-1489 (2016).
- 50 Park, H. *et al.* Hierarchical micro-lamella-structured 3D porous copper current collector coated with tin for advanced lithium-ion batteries. *Applied Surface Science* **399**, 132-138 (2017).
- 51 Kumar, A. & Reddy, R. G. Modeling of polymer electrolyte membrane fuel cell with metal foam in the flow-field of the bipolar/end plates. *Journal of Power Sources* **114**, 54-62 (2003).
- 52 Kumar, A. & Reddy, R. G. Materials and design development for bipolar/end plates in fuel cells. *Journal of Power Sources* **129**, 62-67 (2004).
- 53 Arisetty, S., Prasad, A. K. & Advani, S. G. Metal foams as flow field and gas diffusion layer in direct methanol fuel cells. *Journal of Power Sources* **165**, 49-57 (2007).
- 54 Tsai, B.-T. *et al.* Effects of flow field design on the performance of a PEM fuel cell with metal foam as the flow distributor. *International Journal of Hydrogen Energy* **37**, 13060-13066 (2012).
- 55 Tseng, C.-J. *et al.* A PEM fuel cell with metal foam as flow distributor. *Energy Conversion and Management* **62**, 14-21 (2012).
- 56 Tseng, C.-J., Heush, Y.-J., Chiang, C.-J., Lee, Y.-H. & Lee, K.-R. Application of metal foams to high temperature PEM fuel cells. *International Journal of Hydrogen Energy* **41**, 16196-16204 (2016).
- 57 Zawodzinski, T. A. *et al.* A Comparative Study of Water Uptake By and

- Transport Through Ionomeric Fuel Cell Membranes. *Journal of The Electrochemical Society* **140**, 1981-1985 (1993).
- 58 Büchi, F. N. & Scherer, G. G. Investigation of the Transversal Water Profile in Nafion Membranes in Polymer Electrolyte Fuel Cells. *Journal of The Electrochemical Society* **148**, A183-A188 (2001).
- 59 Wang, X.-D., Duan, Y.-Y., Yan, W.-M. & Weng, F.-B. Effect of humidity of reactants on the cell performance of PEM fuel cells with parallel and interdigitated flow field designs. *Journal of Power Sources* **176**, 247-258 (2008).
- 60 Jeon, D. H., Kim, K. N., Baek, S. M. & Nam, J. H. The effect of relative humidity of the cathode on the performance and the uniformity of PEM fuel cells. *International Journal of Hydrogen Energy* **36**, 12499-12511 (2011).
- 61 Miyake, N., Wainright, J. S. & Savinell, R. F. Evaluation of a Sol-Gel Derived Nafion/Silica Hybrid Membrane for Proton Electrolyte Membrane Fuel Cell Applications: I. Proton Conductivity and Water Content. *Journal of The Electrochemical Society* **148**, A898-A904 (2001).
- 62 Sahu, A. K., Selvarani, G., Pitchumani, S., Sridhar, P. & Shukla, A. K. A Sol-Gel Modified Alternative Nafion-Silica Composite Membrane for Polymer Electrolyte Fuel Cells. *Journal of The Electrochemical Society* **154**, B123-B132 (2007).
- 63 Wang, C. *et al.* Composite Membranes with Sulfonic and Phosphonic Functionalized Inorganics for Reduced Relative Humidity PEM Fuel Cells. *Journal of The Electrochemical Society* **158**, B690-B697 (2011).
- 64 Choun, M., Chung, S., Jeon, H., Uhm, S. & Lee, J. Atomic-layer-deposited TiO₂ on cathode gas diffusion layer for low humidity operation in hydrogen fuel cells. *Electrochemistry Communications* **24**, 108-111 (2012).
- 65 Inoue, N., Uchida, M., Watanabe, M. & Uchida, H. Experimental analyses

- of low humidity operation properties of SiO₂-containing catalyst layers for polymer electrolyte fuel cells. *Electrochimica Acta* **88**, 807-813 (2013).
- 66 Choi, I. *et al.* Characterization of self-humidifying ability of SiO₂-supported Pt catalyst under low humidity in PEMFC. *Applied Catalysis B: Environmental* **168–169**, 220-227 (2015).
- 67 Kitahara, T., Nakajima, H. & Okamura, K. Gas diffusion layers coated with a microporous layer containing hydrophilic carbon nanotubes for performance enhancement of polymer electrolyte fuel cells under both low and high humidity conditions. *Journal of Power Sources* **283**, 115-124 (2015).
- 68 Zhang, J., Song, C., Zhang, J., Baker, R. & Zhang, L. Understanding the effects of backpressure on PEM fuel cell reactions and performance. *Journal of Electroanalytical Chemistry* **688**, 130-136 (2013).
- 69 Kim, D. K., Koh, J. S., Kim, M. S. & Song, H. H. Experimental and computational study on the dynamic interaction between load variation and back pressure control in a polymer electrolyte membrane fuel cell for automotive application. *International Journal of Hydrogen Energy* **40**, 12370-12381 (2015).
- 70 Rohendi, D. *et al.* Effects of temperature and backpressure on the performance degradation of MEA in PEMFC. *International Journal of Hydrogen Energy* **40**, 10960-10968 (2015).
- 71 Wind, J., Späh, R., Kaiser, W. & Böhm, G. Metallic bipolar plates for PEM fuel cells. *Journal of Power Sources* **105**, 256-260 (2002).
- 72 Yuan, X.-Z., Song, C., Wang, H. & Zhang, J. *Electrochemical Impedance Spectroscopy in PEM Fuel Cells: Fundamentals and Applications*. 1-37 (Springer London, 2010).
- 73 Tang, Y., Yuan, W., Pan, M. & Wan, Z. Feasibility study of porous copper fiber sintered felt: A novel porous flow field in proton exchange membrane

fuel cells. *International Journal of Hydrogen Energy* **35**, 9661-9677 (2010).

- 74 Banhart, J. Manufacture, characterisation and application of cellular metals and metal foams. *Progress in Materials Science* **46**, 559-632 (2001).

Chapter 3. High-performance Fuel Cell with Stretched Catalyst-Coated Membrane: One-step Formation of Cracked Electrode

3.1. Introduction

Polymer electrolyte membrane fuel cell (PEFC) has been extensively studied as an eco-friendly alternative energy device in the aspect of high energy conversion efficiency and continuous production of the electricity without pollutant emissions.¹⁻⁴ Recently, there have been several technical issues for the commercialization of PEFC including water management at the cathode in the membrane electrode assembly (MEA)⁵⁻⁸ and resistance reduction of the electrolyte membrane.^{9,10} To improve transport of water generated from electrochemical reaction at the cathode, research has been conducted on inserting meso/macro pore structures such as platinum inverse opal structure and pore formers into the electrode, which methods need chemical post-treatments.¹¹⁻¹⁵ Moreover, there have been attempts to reduce the resistance of an electrolyte membrane by lowering the thickness of the membrane. This thinning method, however, has remained as a challenge due to the inferior mechanical properties of the thinned membrane.^{2,10}

Herein, in order to address these issues in a simple and effective way, we deliberately generated cracks on the electrode composed of carbon supported Pt particles (Pt/C) by stretching out a membrane electrode assembly (MEA) and used the stretched MEA in order to enhance mass transport in the electrode and to reduce ohmic resistance simultaneously. Generally, cracks are generated from the elastic mismatch between two attached surfaces with different elastic modulus

when the surfaces are deformed.^{16,17} Cracks have commonly been considered as defects¹⁸⁻²² and many studies have focused on how to avoid them. However, recent studies have indicated that cracks can be used to detect the strain force as in an ultrasensitive sensor,¹⁶ microfluidic channels¹⁷ and so on. It is noteworthy that the crack can be a useful tool rather than a defect, when it is properly generated with a purpose of achieving a specific goal.

3.2. Experimental section

3.2.1. Preparation of membrane electrode assembly (MEA)

Catalyst ink was prepared by mixing water, 5 wt.% Nafion solution (DuPont) and isopropyl alcohol (IPA) (Aldrich) with the catalyst. 40 wt.% Pt/C (Johnson Matthey) was used for the cathode catalyst inks. The prepared catalyst ink was blended by ultrasonic treatment and sprayed onto the cathode side of bare Nafion 212 membrane to fabricate MEAs. The catalyst loadings were equally 0.2 mg cm^{-2} in the cathodes of the MEAs. These catalyst-coated membranes (CCMs) were dried at room temperature for more than 12 hours. After the process of stretching out the CCMs, the prepared catalyst ink was sprayed onto the anode side with 0.2 mg cm^{-2} catalyst loading. Then, gas diffusion layers (GDLs, SGL 35 BC), Teflon type gaskets and one channel serpentine-type (Figure 3.1) were put onto the anode and cathode without a hot-press process.

3.2.2. Process of stretching out prepared CCMs

As-prepared catalyst-coated membranes were stretched out by a stretcher machine (Intron Corp.), which can provide the strong binding force of the chuck and the uniform strain to the membrane. One side of the membrane was fixed and the other side of the membrane was pressed by two bite-blocks with the width of 5 cm. The initial length of the membrane was 2 cm and the membrane was stretched out with variation of strains (0.5, 1.0, 1.5, and 2.0). See detailed experimental process in Figure 3.2. And the samples without the stretching process were also prepared as a reference.

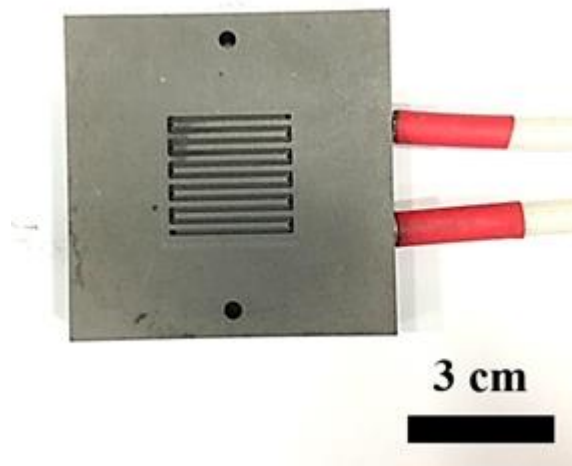


Figure 3.1 A camera image for one channel serpentine-type.

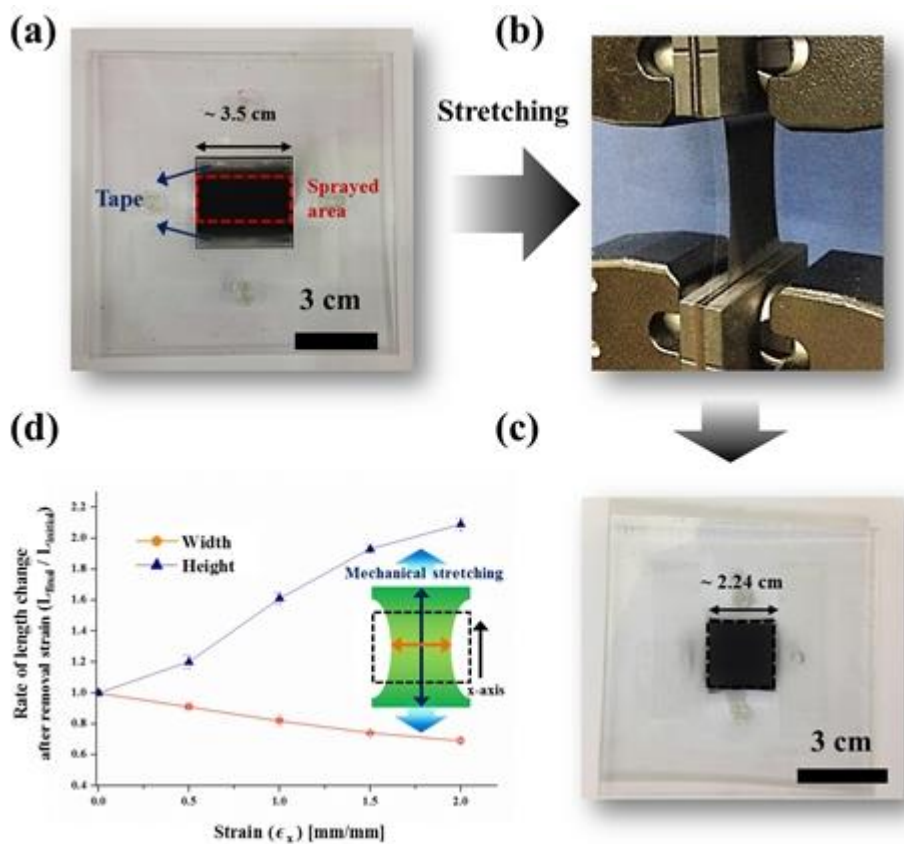


Figure 3.2 (a-c) Camera images for the preparation of stretched MEA within ~ 5 cm^2 active area. (d) Changes of width and height of Nafion membrane with variation of strains (0.5, 1.0, 1.5 and 2.0).

3.2.3. Physical analysis

Field emission-scanning electron microscopy (FE-SEM) was conducted using a SUPRA 55VP microscope (Carl Zeiss) to measure the morphology of the various samples used in this paper. The samples were observed at SE mode without additional coating processes.

3.2.4. Electrochemical measurements

Prepared MEAs were assembled in a single cell (CNL PEM005-01, CNL Energy). For the single cell performance test at 70°C, humidified H₂ and O₂ (air) gases were made to flow into the anode and cathode with the active geometric areas of 5.0 cm², respectively. The stoichiometric coefficient of H₂/O₂ (air) was 2.0/9.5 (2.0). Additionally, the relative humidity (RH) for the anode and cathode gases were 100%. To check repeatability, we tested five different samples which have the same applied strain. Electrochemical impedance spectroscopy (EIS) (Zennium, Zahner) of the single cells was measured at 0.6 V with an amplitude of 5 mV. The measurement was conducted in the frequency range from 0.1 Hz to 100 kHz. Other experimental conditions, such as temperature and gas humidification, were the same as the case for the single-cell operation at 70°C with H₂/Air. The ZView program (Scribner Associates Inc.) was used to fit the EIS data, and a simple equivalent circuit was applied as shown in Figure 3.10. Cyclic voltammograms (CVs) were obtained at 100 mV s⁻¹ between 0.05 and 1.20 V to measure the electrochemical active surface (EAS) of the prepared cathode catalyst layers at room temperature. Humidified H₂ and N₂ gases were supplied to the anode and cathode, respectively, and the RH was 100% during the CVs measurement. The anode with H₂ gas flowing around was used as the reference and counter electrodes, and the cathode with N₂ gas served as a working electrode.

3.3. Results and Discussion

3.3.1. Generation of cracks in the electrode by stretching out the catalysts-coated Nafion membrane

Figure 3.3 shows the schematic illustration of crack generation in the electrode. A Nafion membrane has a relatively lower elastic modulus than a porous electrode with Pt/C. From this difference in elastic modulus called elastic mismatch, when the two attached surfaces are stretched out, cracks are generated on the porous electrode. If the Nafion membrane is stretched over the elastic deformation region, then it would not recover its original shape, and this means that the membrane has become longer than its original length due to the applied strain. And then, the cracks on the electrode also maintain their deformed shape along with the deformed membrane.

3.3.2. Physical property of Nafion membrane

To investigate the stretching property of a Nafion membrane, we conducted a strain test on a Nafion 212 membrane with a thickness of ~ 50 μm . As shown in Figure 3.4, the membrane showed the maximum tensile strength of ~ 31.11 MPa and elongation of $\sim 300\%$ till its break. (Table 3.1) This result shows that the membrane can endure the stress until reaching the maximum tensile strength before it tears off, and can be stretched out to ~ 3 times of its original length, which is an intriguing feature in terms of stretchability. Furthermore, the shape of the strain-stress curve in Figure 3.4 (a) presents that the region of elastic deformation completely which has recovered to its original length is under ~ 0.08 strain, and it shows that the plastic deformation which has incompletely recovered in the region is above ~ 0.08 strain. The plastic deformation region is much wider than the elastic region and we used the plastic deformation of the membrane to simultaneously reduce the thickness of the membrane and generate cracks in the electrodes composed of Pt/C particles. As shown in Figure 3.4 (b), we measured the rate of

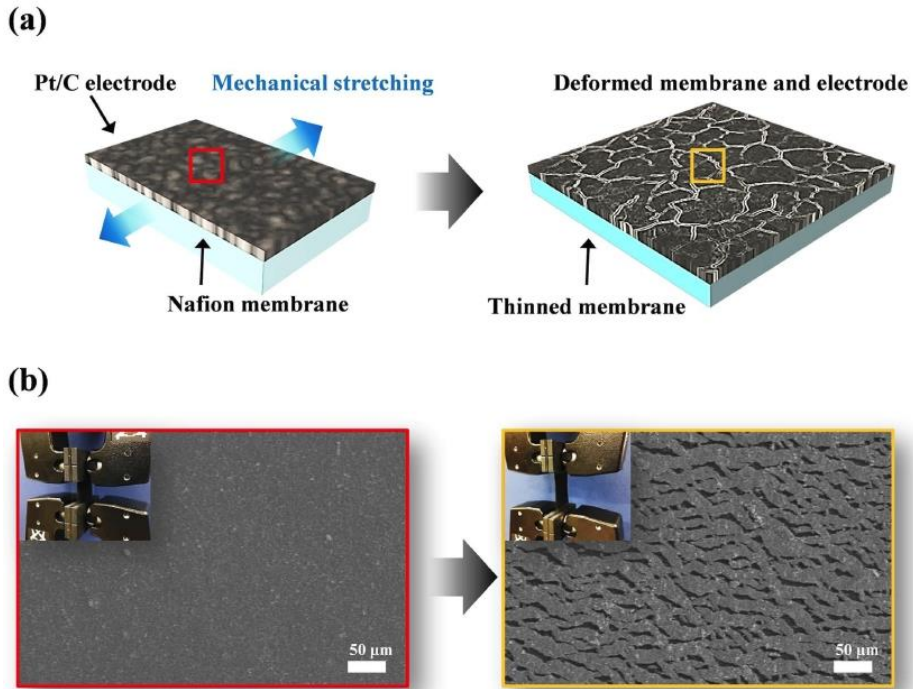


Figure 3.3. Generation of cracks in the electrode: (a) Schematic illustration of generating cracks in Pt/C catalyst layer with simply mechanical stretching. (b) Corresponding SEM images of catalyst layer before (left) and after (right) stretching out the catalyst coated membrane (Inset: corresponding optical images of stretcher machine)

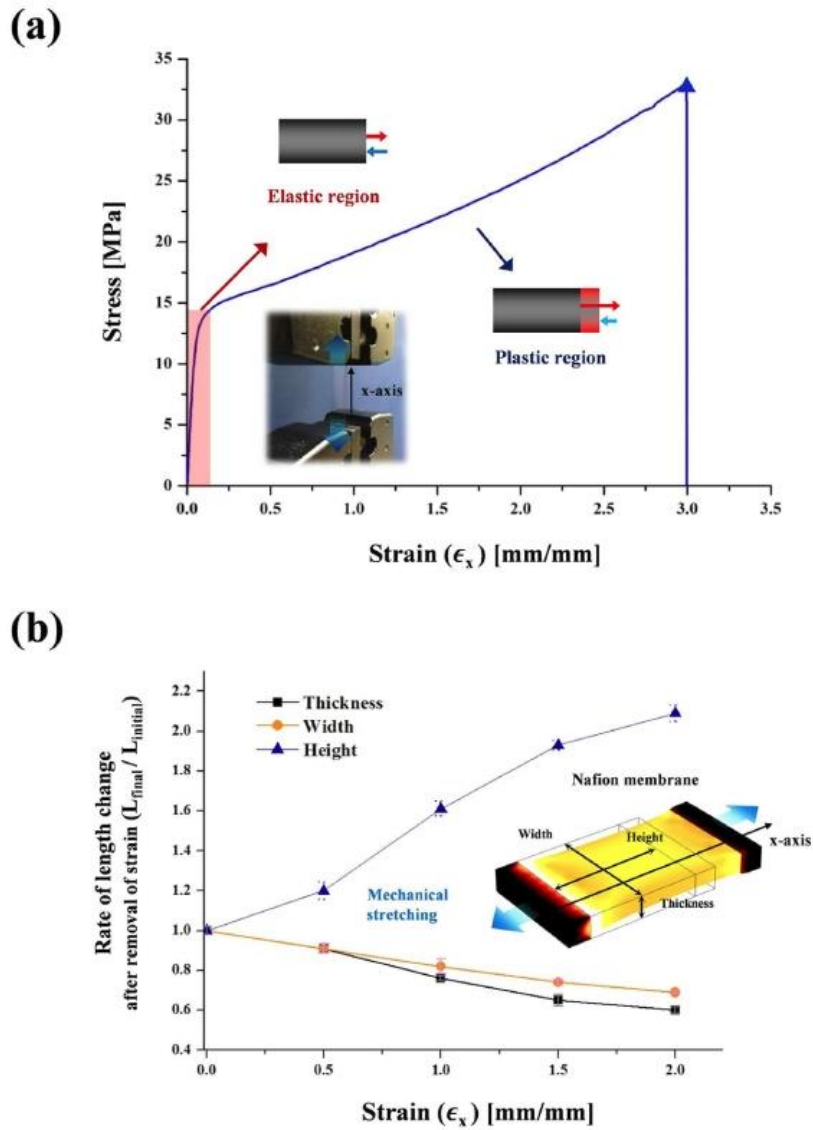


Figure 3.4 Physical property of Nafion membrane: Stretching properties of Nafion 212 membrane. (a) Strain-stress curves of Nafion membrane obtained by applying strain to the membrane until its breaks. (b) Changes of width, height and thickness of Nafion membrane with variation of strains (0.5, 1.0, 1.5 and 2.0).

Table 3.1 Physical property of Nafion 212 membrane

<i>Tensile strength, max. [MPa]</i>	<i>Elongation to break, %</i>
31.11 (\pm 2.49)	300 (\pm 18)

changes of width, height and thickness of a Nafion membrane according to the variation of strains (0.5, 1.0, 1.5 and 2.0) after removing them. And, we ascertained that changes of the membrane thickness were spatially uniform after the removal of strains as shown in Figure 3.5.

3.3.3. Morphological features of the generated cracks with variation of strains

To investigate the geometrical features of the cracks induced by applied strains, we observed the cracks with variation of strains by using a scanning electron microscopy (SEM) as shown in Figure 3.6 (a). The catalyst-coated membranes were stretched out with variation of strains (S; 0.5, 1.0, 1.5, and 2.0) and areal fractions of the cracks with each strain in the corresponding SEM images were analyzed by using an image analysis program (ImageJ). As expected, the areal fractions of cracks increased as the value of strain increased. (~7.8 % for S~0.5, ~13.4 % for S~1.0, ~22.5% for S~1.5, and ~33.4% for S~2.0) Interestingly, we observed that the size of the cracks enlarged as the strain intensified. It implies that the cracks, or the macro-pores, in the catalyst layer can be controlled by the value of strain.

3.3.4. Improved performance with cracked membrane electrode assembly (MEA) in polymer electrolyte membrane fuel cell (PEFC)

To demonstrate the effect of cracks on the performance of PEFC, we incorporated a cracked MEA into a single cell. This single cell with the cracked MEA was operated in a fully humidified condition of H₂/O₂ (H₂/Air) and exhibited highly improved performance under all the conditions regardless of the strains compared with a conventional MEA, as shown in Figure 3.6 (b) and (c). However, the MEA with a strain of ~ 2.0 applied exhibited more decreased performance than other samples under H₂/air condition. This resulted from the catalysts debonded by high strain. When looking into the surface morphology of the stretched MEA at a lower

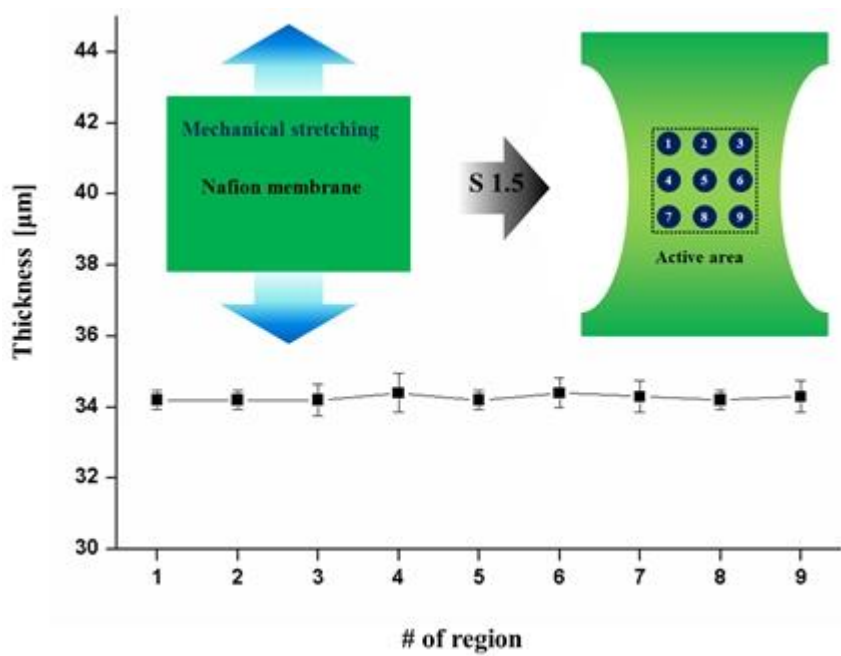


Figure 3.5 Measurement of the membrane thickness after stretching out the membrane

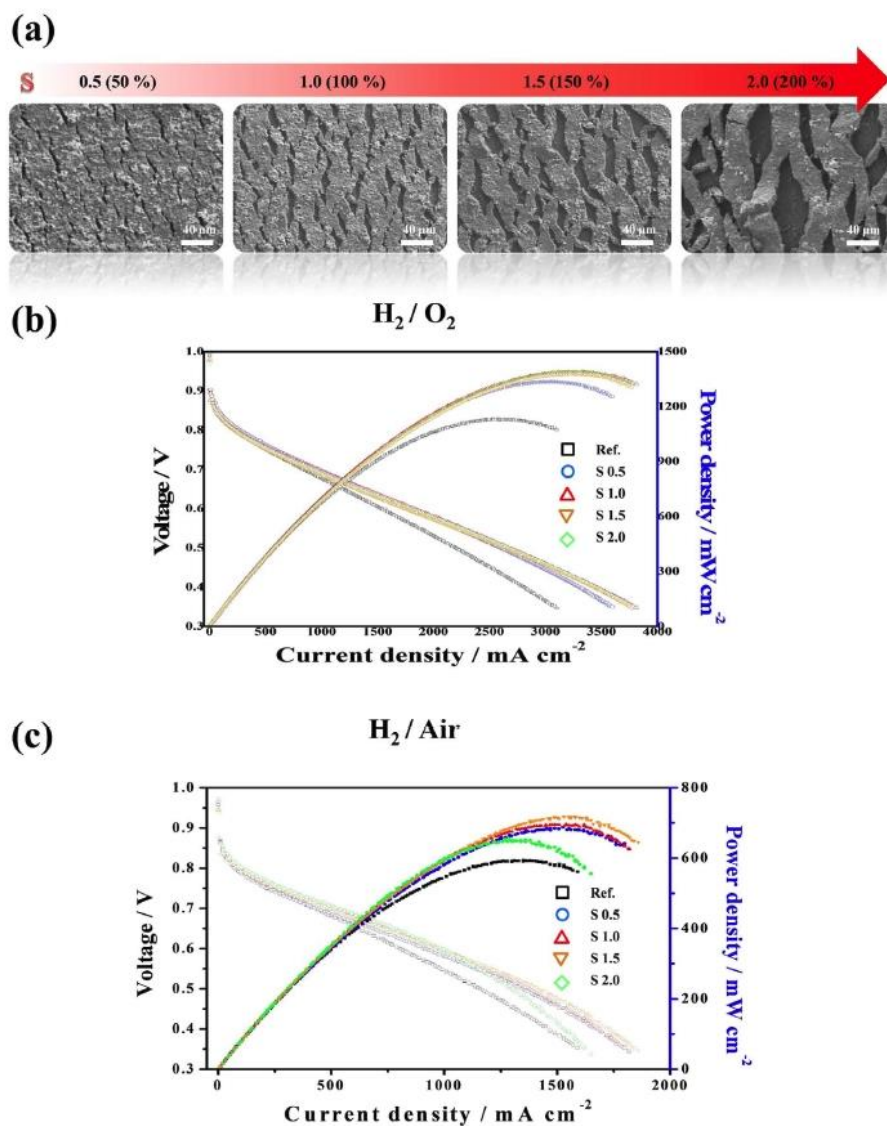


Figure 3.6 Morphological features of the generated cracks and measurements of device performance: (a) Corresponding SEM images of catalyst coated membrane after applying various strains (0.5, 1.0, 1.5 and 2.0). (b,c) Polarization curves of conventional membrane electrode assembly (MEA) and the MEA with electrode cracks with variation of strains (0.5, 1.0, 1.5 and 2.0) under the conditions of H_2/O_2 (b) and H_2/Air (c).

magnification of the SEM (Figure 3.6), we observed that only the catalyst layer of the stretched MEA with a strain of ~ 2.0 was detached from the membrane (In some cases, we observed with the naked eye that large Pt/C aggregates in the catalyst layer were locally separated from the membrane.). The detached catalyst layer would induce degradation of performance due to the increase of interfacial resistance and loss of the Pt catalyst. And, the result indicates that there exists the upper limit of applied strain to the catalyst-coated membrane and the optimal strain for the high performance of the MEA. In our experimental sets, the stretched MEA with 1.5 strain applied exhibited the highest performance. It showed the maximum power density of $\sim 0.72 \text{ W cm}^{-2}$ in the case of H_2/air conditions, which power density is higher than the conventional one ($\sim 0.59 \text{ W cm}^{-2}$) by $\sim 22\%$. (Table 3.2) The area of cracks in MEAs was 7.8, 13.4, 22.5, and 33.4% in S0.5, S1.0, S1.5 and S2.0, respectively. To quantify the area and performance of the cracks, the trends are expressed in formulas and shown in Figure 3.7. (The x-axis is the area of the crack, and the y-axis is the maximum power densit.) When expressed as a linear equation, the highest performance can be expected when the crack area is about 21%. When the maximum power density according to the crack area was represented by a quadratic equation, the best performance was expected at a crack of about 19%. Thus, the best performance could be expected to occur when looking for strains where 19-21% cracks are generated.

These performance enhancements can be explained by the effects from a crack acting as a macro-pore and the thinned membrane. First, the water transport enhancement which was confirmed by the difference of the power density that increased as the current density increased contributed to the performance enhancement of the MEA. Second, the membrane thickness reduced by stretching out has lowered ohmic resistance that occurs during the PEFC operation. To address the stability issue, we conducted accelerated durability tests (ADTs) by repeated polarization test for ~ 1000 cycles with fully humidified H_2/Air gases

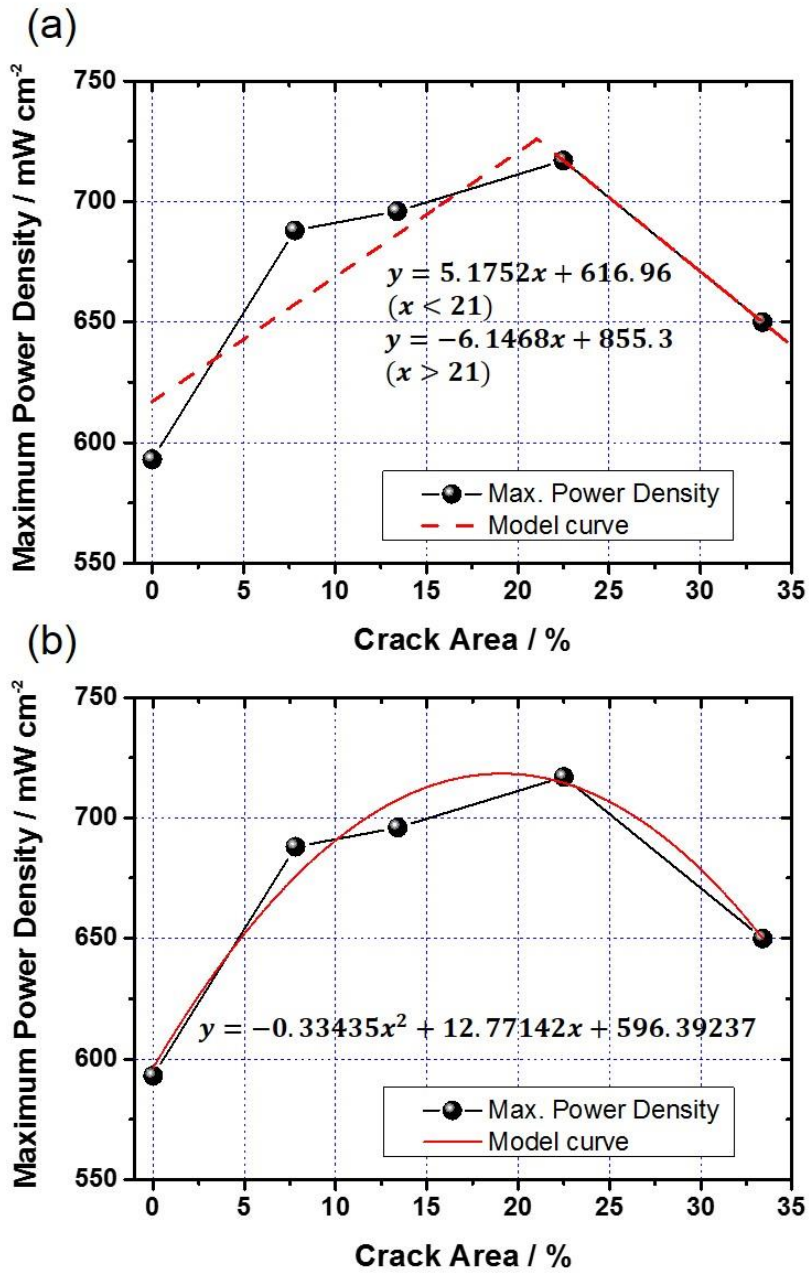


Figure 3.7. The results of maximum power densities according to the ratio of cracks in the MEAs

supplied to anode and cathode, respectively. Even after ADT tests, the maximum power density of the stretched MEA was higher than the conventional MEA by ~36.7 % in the case of H₂/Air conditions under ambient pressure as shown in Figure 3.9. Furthermore, the morphology of the cracks was maintained even after the durability test was carried out as shown in Figure 3.10. There was no breakdown of the system even with the long term electrochemical stress. The results have come from the fact that pre-defined cracks from stretching out provide more available space that would distribute stress from the Nafion membrane when it swells and contracts. Hence, the stretched MEA with cracks have advantages in durability and long term stability than the conventional one.

3.3.5. Electrochemical analysis of cracked MEA

To quantitatively investigate the effect of water transport enhancement and reduced ohmic resistance, both electrochemical impedance spectroscopy (EIS) and cyclic voltammetry (CV) were conducted (Figure 3.11). As shown in Figure 3.11 (a), comparable electrochemical active surface area (ECSA) was observed from the CV measurement,²³ which indicates that the generated crack doesn't affect the area of tri-phase boundary during the operation. When the EIS data were fitted and calculated by the equivalent circuit (Figure 3.11 (b)),²⁴ we found relatively lower ohmic resistance in the case of the 1.5-strain-applied MEA than that of the conventional one by ~ 14 %, which resulted from the thinned membrane in the stretching process. Moreover, the Warburg impedance of the 1.5-strain-applied MEA (0.0393 Ω cm²) was much smaller than that of the conventional one (0.0691 Ω cm²), although the current density of the 1.5-strain-applied MEA was higher than that of the reference at 0.6 V. (Table 3.3) Furthermore, results of EIS measurement at the same current density (~ 1.4 A cm⁻²) show less resistance in the case of stretched MEA (S~1.5) than that of the reference as shown in Figure 3.12. It means that the water removal from the cathode catalyst layer has been improved due to

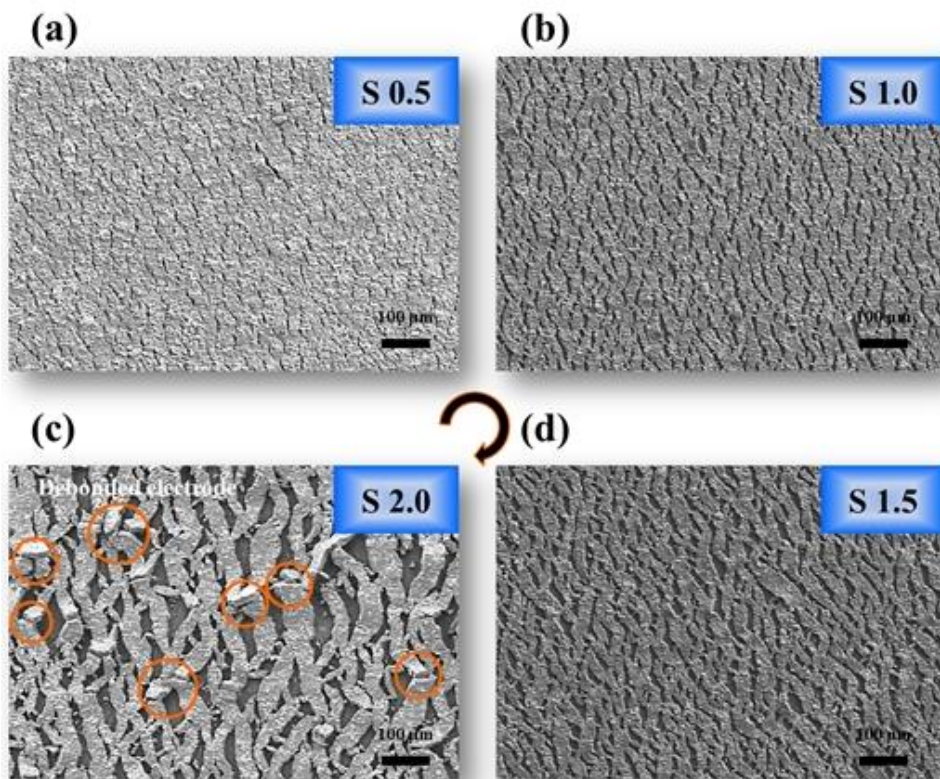


Figure 3.8. SEM images for catalyst layer of stretched MEA for each strain (0.5, 1.0, 1.5 and 2.0)

Table 3.2 Physical and electrochemical properties of the samples.

	Maximum power density (W cm ⁻²)	ECSA (m ² g ⁻¹)	Pt loading (mg cm ⁻²)	Average Pt particle size (nm)	Geometric Surface Area (m ² g ⁻¹)	Pt utilization (%)
Conventional MEA	0.59 (1.13) ^a	59.17				63.31
			0.20	3.00 ^b	93.46 ^b	
1.5-strain applied MEA	0.72 (1.38) ^a	58.67				62.78

^a Cell operation under ambient pressure with H₂/air (H₂/O₂).

^b Nature comm., 6, 9484 (2015).

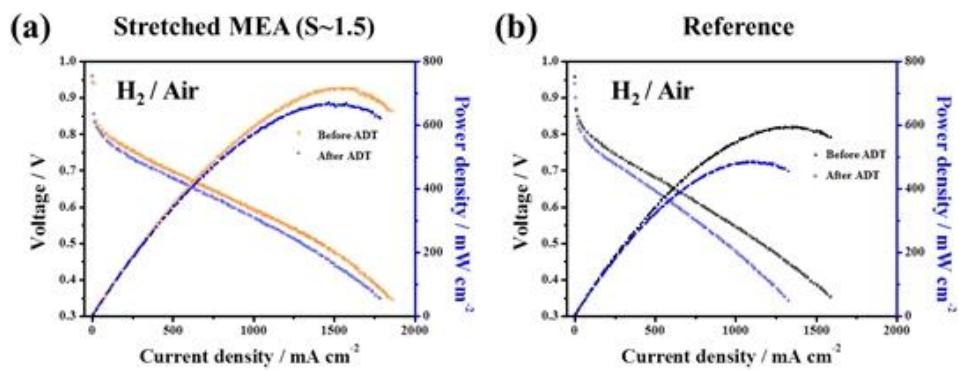


Figure 3.9 Accelerated durability test (ADT) for the stretched MEA with 1.5 strain and reference MEA

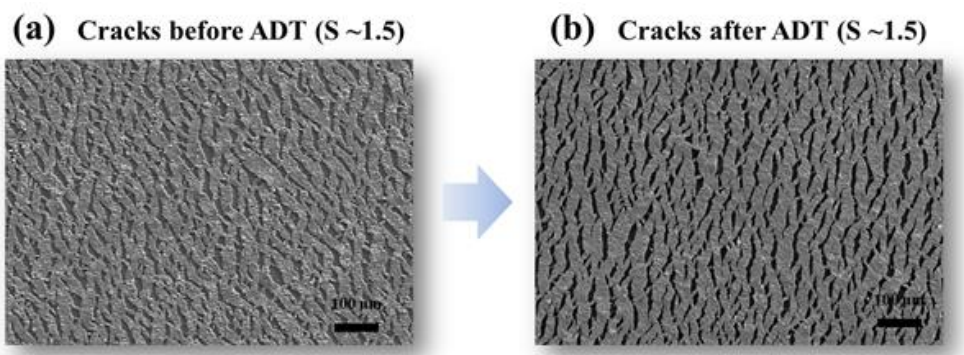


Figure 3.10 SEM images for catalyst layer of stretched MEA before ADT(a) and after ADT(b)

the existence of cracks. The enhanced water transport also can be confirmed by calculating the oxygen gain. The data of the oxygen gain were obtained by calculating potential difference when oxygen and air are supplied in the current density range and they indicate the degree of mass transfer in the cathode catalyst layer. In Figure 3.13, the calculated oxygen gain of the 1.5-strain-applied MEA showed much lower values than the conventional one, which means that the generated cracks in the cathode catalyst layer removed the produced water much easily and helped the MEA to supply fuel gas more effectively than the conventional one.

3.3.6. Membrane thinning effect

To further investigate the mass transport effect while excluding the membrane thinning effect, we measured performances of the stretched MEA and the MEA with only the membrane stretched. The performance of the MEA with only the membrane stretched was slightly higher than that of the stretched MEA in the condition of H_2/O_2 . However, in the condition of H_2/Air , the stretched MEA showed much higher performance than the MEA with only the membrane stretched as shown in Figure 3.13. In view of the commonly known fact that the performance in the condition of H_2/Air is more affected by mass transport than that in the condition of H_2/O_2 , the stretched MEA with cracks displayed positive effect in improving mass transport. We also conducted EIS measurement of the stretched MEA and the MEA with only the membrane stretched. Figure 3.14 (a) shows that they exhibited comparable ohmic resistances. The radius of the circle of the stretched MEA was much smaller than that of the MEA with only the membrane stretched, which implies that the generated crack has improved mass transport. Moreover, oxygen gain calculation for the experiments also supports our results (Figure 3.14 (b)).

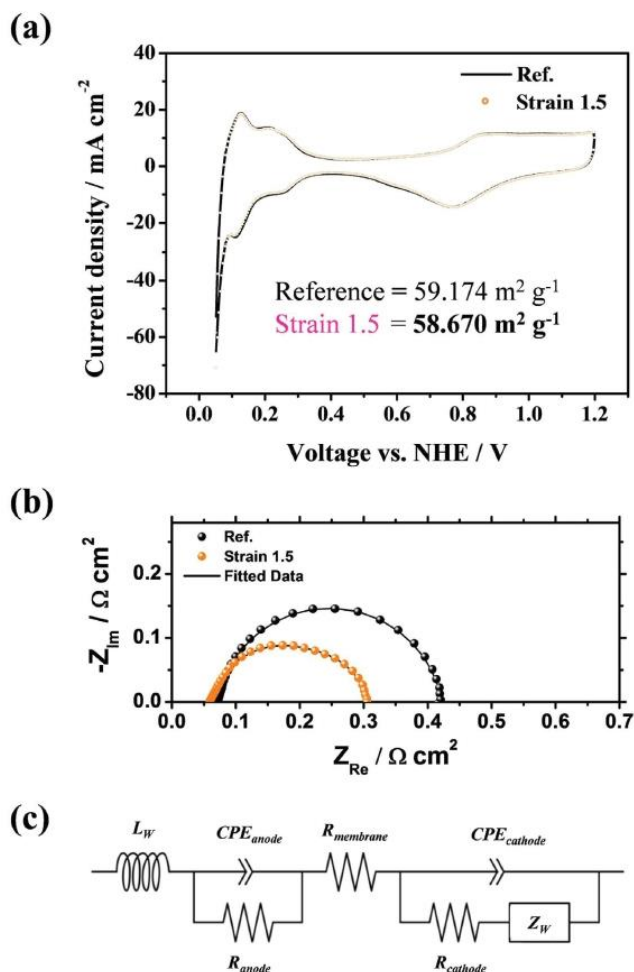


Figure 3.11 Electrochemical analysis: (a) Cyclic voltammogram (CV) of the cathode catalyst layers of a conventional MEA and the 1.5-strain applied MEA. (b) Electrochemical impedance spectroscopy (EIS) of a conventional MEA and the 1.5-strain applied MEA, at 0.6 V compared with RHE. (c) Equivalent circuit of the PEFC (L_W = inductance of the electric wire, $R_{membrane}$ = internal membrane resistance, $R_{cathode}$ (anode) = charge transfer resistance of the cathode (anode), $CPE_{cathode}$ (anode) = constant phase element of the cathode (anode) and Z_W = Warburg impedance).

Table 3.3 Electrochemical impedance spectroscopy (EIS) fitted data.

	R_{membrane}	R_{cathode}	Z_{w} (Warburg)
Conventional MEA	0.0651 (100%)	0.2987 (100%)	0.0691 (100%)
1.5-strain applied MEA	0.0560 (86.0%)	0.1995 (66.8%)	0.0393 (56.8%)

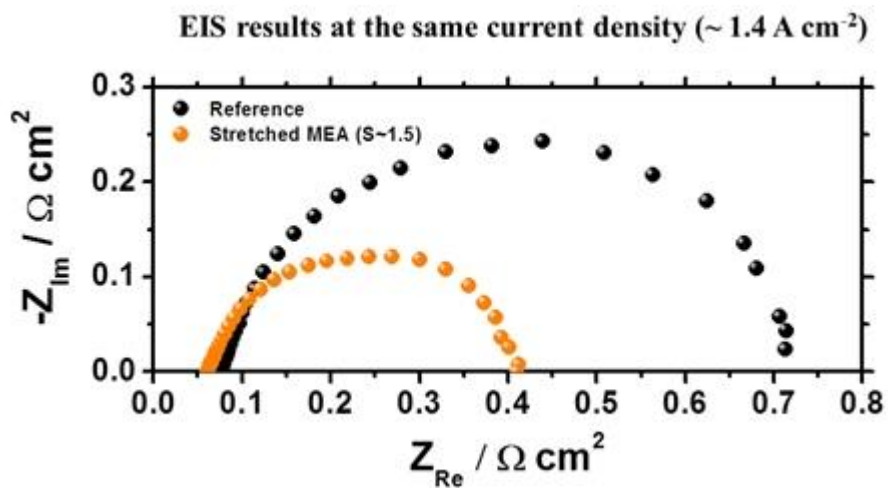


Figure 3.12. EIS measurements at the same current density ($\sim 1.4 \text{ A cm}^{-2}$) for the sample of reference and stretched MEA (S ~ 1.5)

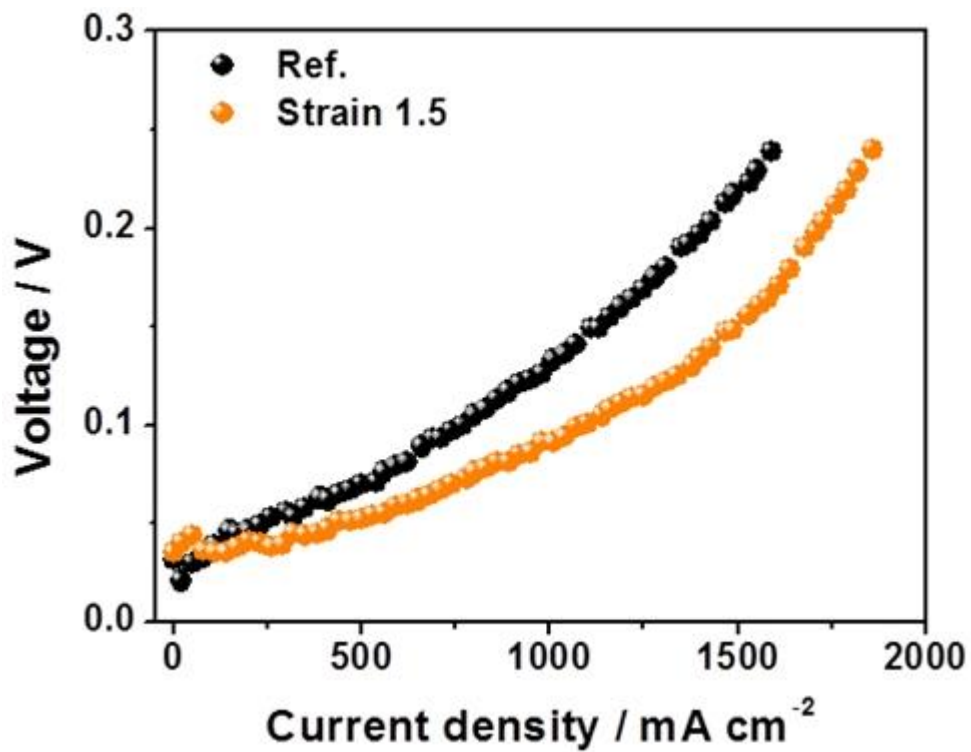


Figure 3.13 The graph for the oxygen gain obtained by calculating potential difference when oxygen and air are supplied respectively

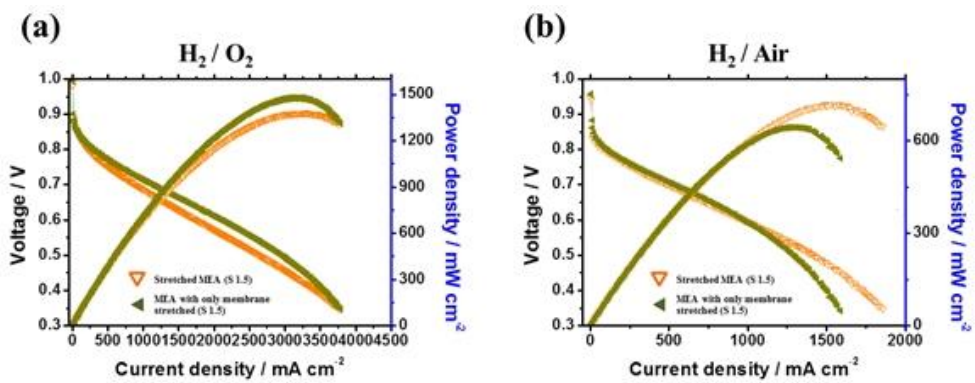


Figure 3.14. Polarization curves of the stretched MEA and the MEA with only membrane stretched. (a) H₂/O₂ condition, (b) H₂/Air condition.

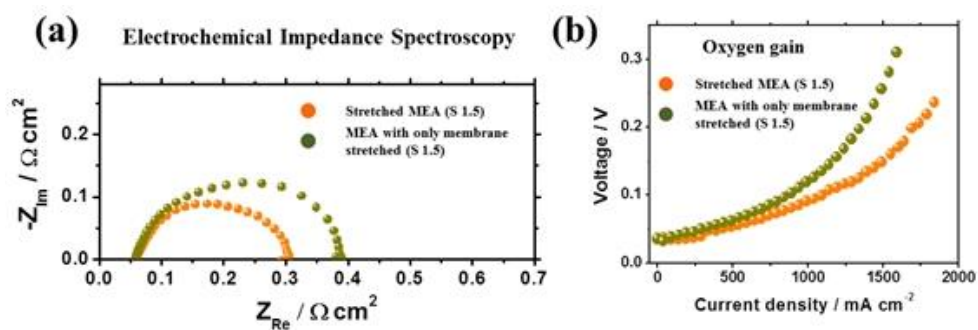


Figure 3.15. (a) EIS measurement of the stretched MEA and the MEA with only membrane stretched. (b) Oxygen gain calculation of the stretched MEA and the MEA with only membrane stretched.

3.4. Conclusions

In this study, we have presented, for the first time, a novel strategy to improve water transport and reduce ohmic resistance by simply stretching out the Pt/C-coated Nafion membrane. With the use of the unique stretching property of the Nafion membrane which has the maximum elongation of ~300% until its break, we have incorporated electrode cracks with the variations of strain (0.5, 1.0, 1.5 and 2.0) into a single cell. The generated cracks effectively enhanced water transport in the cathode catalyst layer, which was confirmed by oxygen gain and EIS measurements. Moreover, the thinned membrane from stretching out was found to reduce the ohmic resistance. These combinational effects of improved water transport and reduced ohmic resistance of the 1.5-strain-applied MEA resulted in performance enhancement compared by ~22 % of the performance of the conventional one. Our novel approach of using cracks that have been considered as defects surely possesses potential to be applied to other energy conversion and storage devices. This technique can also be helpful, with its thinned MEA, in reducing the total volume of fuel cell stacks for compact applications such as in vehicles. We performed ADT with load cycling and observed better durability in the MEA with the cracks. However, in order to clearly distinguish between the advantages and disadvantages of the cracks, there are various ADTs to check (constant current/voltage, OCV, and etc.).

3.5. References

- 1 Gasteiger, H. A. & Marković, N. M. Just a Dream—or Future Reality? *Science* **324**, 48-49 (2009).
- 2 O'Hayre, R. P., Cha, S.-W., Colella, W. & Prinz, F. B. *Fuel cell fundamentals. 2nd ed., Ch. 1, 3-23* (John Wiley & Sons New York, 2006).
- 3 Barbir, F. *PEM fuel cells. 2nd ed., Ch. 1, 1-16* (Springer, 2006).
- 4 Jang, J.-M. *et al.* The Analysis on the Activation Procedure of Polymer Electrolyte Fuel Cells. *Journal of Electrochemical Science and Technology* **2**, 131-135 (2011).
- 5 Jung, N. *et al.* High-performance hybrid catalyst with selectively functionalized carbon by temperature-directed switchable polymer. *Chemistry of Materials* **25**, 1526-1532 (2013).
- 6 Sinha, P. K., Mukherjee, P. P. & Wang, C. Y. Impact of GDL structure and wettability on water management in polymer electrolyte fuel cells. *J. Mater. Chem.* **17**, 3089-3103 (2007).
- 7 Li, H. *et al.* A review of water flooding issues in the proton exchange membrane fuel cell. *Journal of Power Sources* **178**, 103-117 (2008).
- 8 Tanuma, T. Ex Situ Characterization Method for Flooding in Gas Diffusion Layers and Membrane Electrode Assemblies With a Hydrophilic Gas Diffusion Layer. *Journal of Fuel Cell Science and Technology* **12**, 061002 (2015).
- 9 Slade, S., Campbell, S., Ralph, T. & Walsh, F. Ionic conductivity of an extruded Nafion 1100 EW series of membranes. *Journal of the Electrochemical Society* **149**, A1556-A1564 (2002).
- 10 Cho, H. *et al.* Multiplex lithography for multilevel multiscale architectures and its application to polymer electrolyte membrane fuel cell. *Nature communications* **6**, 8484, doi: 10.1038/ncomms9484 (2015).

- 11 Kim, O.-H. *et al.* Ordered macroporous platinum electrode and enhanced mass transfer in fuel cells using inverse opal structure. *Nature communications* **4**, 2473, doi: 10.1038/ncomms3473 (2013).
- 12 Cho, Y.-H. *et al.* Improved mass transfer using a pore former in cathode catalyst layer in the direct methanol fuel cell. *international journal of hydrogen energy* **37**, 11969-11974 (2012).
- 13 Reshetenko, T. V., Kim, H.-T. & Kweon, H.-J. Cathode structure optimization for air-breathing DMFC by application of pore-forming agents. *Journal of Power Sources* **171**, 433-440 (2007).
- 14 Zhao, J. *et al.* Addition of NH₄HCO₃ as pore-former in membrane electrode assembly for PEMFC. *International Journal of Hydrogen Energy* **32**, 380-384 (2007).
- 15 Cheon, S.-Y. *et al.* Electroless Nickel Plating on Fibers for the Highly Porous Electrode. *Journal of Electrochemical Science and Technology* **1**, 117-120 (2010).
- 16 Kang, D. *et al.* Ultrasensitive mechanical crack-based sensor inspired by the spider sensory system. *Nature* **516**, 222-226 (2014).
- 17 Kim, H.-N., Lee, S.-H. & Suh, K.-Y. Controlled mechanical fracture for fabricating microchannels with various size gradients. *Lab on a Chip* **11**, 717-722 (2011).
- 18 Nam, K. H., Park, I. H. & Ko, S. H. Patterning by controlled cracking. *Nature* **485**, 221-224 (2012).
- 19 Livne, A., Bouchbinder, E., Svetlizky, I. & Fineberg, J. The near-tip fields of fast cracks. *Science* **327**, 1359-1363 (2010).
- 20 Kundu, S., Fowler, M., Simon, L. & Grot, S. Morphological features (defects) in fuel cell membrane electrode assemblies. *Journal of Power Sources* **157**, 650-656 (2006).

- 21 Guo, Q. & Qi, Z. Effect of freeze-thaw cycles on the properties and performance of membrane-electrode assemblies. *Journal of Power Sources* **160**, 1269-1274 (2006).
- 22 Kim, S. & Mench, M. Physical degradation of membrane electrode assemblies undergoing freeze/thaw cycling: Micro-structure effects. *Journal of Power Sources* **174**, 206-220 (2007).
- 23 Gouws, S. *Voltammetric Characterization Methods for the PEM Evaluation of Catalysts. Ch. 5* (INTECH Open Access Publisher, 2012).
- 24 Yuan, X., Wang, H., Sun, J. C. & Zhang, J. AC impedance technique in PEM fuel cell diagnosis—A review. *International Journal of Hydrogen Energy* **32**, 4365-4380 (2007).

Chapter 4. Guided cracking of electrodes by stretching prism-patterned membrane electrode assemblies for high-performance fuel cells

4.1. Introduction

Polymer electrolyte membrane fuel cells (PEFCs) have received significant attention over the past several decades as future clean energy devices because they do not emit pollutants and they provide high energy conversion efficiencies.¹⁻⁷ Although many technological advances have been achieved in the research field of PEFCs, some practical issues still hinder their commercialization. To obtain high device performance, ohmic loss should be reduced by using a thinned electrolyte membrane⁸⁻¹⁰ and water transport at the cathode of the membrane electrode assembly (MEA) should be enhanced.¹¹⁻¹⁴ In relation to water transport, water molecules that are generated by the oxygen reduction reaction block the catalyst surface and pores in the cathode catalyst layer, reducing device performance. Hence, the produced water must be appropriately removed to maintain the pathway for the reactant oxygen gas. Many attempts have been made to effectively remove the water generated by the electrochemical reaction at the cathode. First, hydrophobic polymer nanoparticles, such as polytetrafluoroethylene, were mixed with a catalyst ink and inserted into the cathode catalyst layer during the MEA fabrication process.¹⁵⁻¹⁷ However, the inserted hydrophobic polymers adhere to the carbon support and catalyst surface without selectivity, which decreases the electrochemically active surface area of the catalyst layer. Another method to improve water transport is to introduce pore-forming agents, such as carbonate or polystyrene particles, which are removed after the catalyst layer is sprayed onto the

electrolyte membrane.¹⁸⁻²⁰ These methods require chemical or thermal post-treatments, which are complex and time consuming.

Our recent study showed that cracks generated on the cathode (formed by stretching the MEA) simultaneously enhanced mass transport and reduced membrane resistance.¹⁰ This simple and facile method does not require any post-treatment after stretching the MEA, and the cracks on the electrode effectively act as macropores to improve mass transport. However, the effects of the crack size and the areal fraction of cracks on device performance have not been studied, and reproduction of the same crack morphology is not easy in the case of MEAs with randomly distributed cracks. To address these issues, we deliberately generated controlled cracks using the concentrated surface stress²⁰⁻²⁴ of a prism-patterned membrane by varying the pattern size and the applied strain. Further, we directly observed that the cracks in MEAs acted as water reservoirs and water passage openings using environmental scanning electron microscopy (ESEM). To assess the effect of cracks with different width and areal fractions on fuel cell device performance, we conducted various electrochemical studies by comparing the device performance of MEAs with and without cracks. All the MEAs with guided cracks exhibited better performance than the conventional MEA, mainly because of the improved water transport.

4.2. Experimental section

4.2.1. Preparation of prism-patterned Nafion membranes

The prism-patterned masters used in this study were prepared by mechanical machining. A plate of stainless steel was machined by using a cutting tool with specific angle. In the process, the height of the prism pattern depended on the cutting depth of the diamond tool. In this study, prism masters with 20 μm and 50 μm periods and the same prism angle ($\sim 45^\circ$) were used. After preparation of the prism master, a prepolymer resin of perfluoropolyether (PFPE) was dispensed onto the prism master mould. Then, PFPE prism moulds were fabricated by UV replica moulding. The cured PFPE moulds were peeled from the master and cut prior to use. The electrolyte membrane (Nafion 212 membrane) was placed uniformly between a glass substrate and the as-prepared PFPE mould. The sandwiched assembly was compressed at $\sim 95^\circ\text{C}$ under a hydraulic pressure of 10–20 kg cm^{-2} for 10 min. After cooling the assembly, the prism-patterned Nafion membrane was peeled from the glass substrate and kept in deionized water for 12 h.

4.2.2. Preparation of prism-patterned MEAs

A catalyst ink was prepared by mixing deionized water, a 5 wt% Nafion ionomer solution, and isopropyl alcohol with carbon-supported catalysts (40 wt% Pt/C, Alfa Aesar, HiSPEC[®] 4000). The prepared catalyst ink was blended by ultrasonication and sprayed onto the cathode side of the as-prepared prism-patterned Nafion membrane to construct the MEAs. The catalyst Pt loadings were $\sim 0.3 \text{ mg cm}^{-2}$ on the cathode sides of the MEAs. The catalyst-coated prism membranes were dried at room temperature ($\sim 25^\circ\text{C}$) for 12 h. After stretching the catalyst-coated membranes, the catalyst inks were sprayed onto the anode with Pt loadings of $\sim 0.3 \text{ mg cm}^{-2}$. Then, Teflon-type gaskets, gas diffusion layers (JNTG-30-A3), and serpentine-type channels were placed onto the cathode and anode without a hot-press process.

4.2.3. Stretching process for the prism-patterned catalyst-coated membranes

The as-prepared catalyst-coated prism membranes were stretched using a stretching machine (Intron Corp.) to provide uniform strains to the membranes. The upper and lower sides of the MEA were pressed using two mechanical wedge grips with widths of ~5 cm to fix the MEA. The lower side of the MEA was fixed and the upper side of the MEA was moved upward to apply strain to the MEA. The MEA was stretched by varying the applied strain (~0.5 and ~1.0). MEAs were also prepared without the stretching process (i.e. conventional MEAs).

4.2.4. Physical analysis

The scanning electron microscopy (SEM) images were acquired by using a field emission scanning electron microscope (Carl Zeiss) at an acceleration voltage of 10.0 kV to observe the morphologies of the membrane and electrode layers of the samples. The water behaviour was examined using ESEM (XL-30 FEG). We observed the water condensation behaviour with respect to time based on the relative humidity (RH; about 95%) by maintaining the chamber pressure at ~5.1 Torr and the substrate temperature at ~2 °C.

4.2.5. FEM analysis

FEM analysis of the stress distribution during the stretching process was performed using the COMSOL Multiphysics software. The behaviours of the elastic and plastic materials were controlled by a governing equation of solid mechanics.³³ Additionally, the plastic property was applied only to the Nafion membrane because the stress applied to the membrane exceeds the elastic limit during the stretching process. Material information for the porous electrode composed of Pt/C, including the elastic modulus and density, was taken from previous studies.^{9,34}

4.2.6. Electrochemical measurements and analysis

The constructed MEAs were incorporated in single cells (CNL Energy). To measure the device performance of a single cell with $\sim 5.0 \text{ cm}^2$ active area at $70 \text{ }^\circ\text{C}$, humidified O_2 (or air) and H_2 gases were supplied to the cathode and anode sides, respectively. The stoichiometric coefficient of H_2/air was 2.0/9.5. Additionally, the RH values for the anode and cathode gases were both 100%. Electrochemical impedance spectroscopy (EIS, ZENNIUM electrochemical workstation, Zahner) was performed for the single cells at 1.6 A cm^{-2} with an amplitude of 500 mA and at 0.6 V with an amplitude of 5 mV. The frequency range of the measurements was from 0.1 Hz to 100 kHz. The Z-View program (Scribner Associates Incorporation) was used to fit the EIS data. Other experimental conditions, including gas humidification and temperature, were the same as those used for single cell operation at $70 \text{ }^\circ\text{C}$ with hydrogen / air. Cyclic voltammograms were obtained between 0.05 and 1.20 V at 100 mV s^{-1} to measure the electrochemical active surface of the constructed cathode catalyst layers at room temperature. Humidified N_2 and H_2 gases were supplied to the cathode and anode, respectively, and the RH was 100% during the cyclic voltammetry (CV) measurements. The cathode with N_2 gas served as the working electrode and the anode with H_2 gas was used as the reference and counter electrodes.

4.3. Results and Discussion

4.3.1. Generation of guided cracks in the cathode

Microprism-patterned arrays consist of repeated valleys and ridges. When the elastic prism structure is stretched in the direction perpendicular to the prism-line direction, the stress is concentrated in the valleys of the prism pattern and the structures are deformed, as shown in Figure 4.1. This means that we can produce confined surface stress in a specific region by controlling the surface structure and applying stress. When rigid material-coated soft prism patterns are stretched, cracks are generated at the interface between the two attached surfaces because of the elastic modulus mismatch when the surfaces are stretched or pressed.^{25,26} Additionally, cracks are generated in the valleys of the prism patterns. Figure 4.2 shows a schematic illustration of the generation of guided cracks in a porous electrode composed of carbon-supported Pt catalysts (Pt/C). Initially, microprism patterns are carved onto a Nafion 212 membrane (thickness $\sim 50 \mu\text{m}$) by thermal imprinting. Then, catalyst ink is sprayed onto the prism-patterned Nafion membrane to construct a porous electrode at the cathode side. When the catalyst-coated Nafion membrane is stretched, the different elastic modulus values of the Nafion membrane and the catalyst layer induce cracking in the catalyst layer. If the applied strain (ϵ), which is defined as the change in length after stretching divided by the original length ($\epsilon = \Delta L/L$), extends beyond the elastic region, the membrane does not fully recover to its original length; this phenomenon is called plastic deformation. Then, cracks between catalyst islands are generated. The crack width increases as the strain applied to the catalyst-coated membrane increases. In our experiments, we concentrated stress in the valleys of the prism patterns and controlled the stress distribution by varying the pattern pitch size. As a result, line-shaped cracks were generated in the valleys with specific lengths.

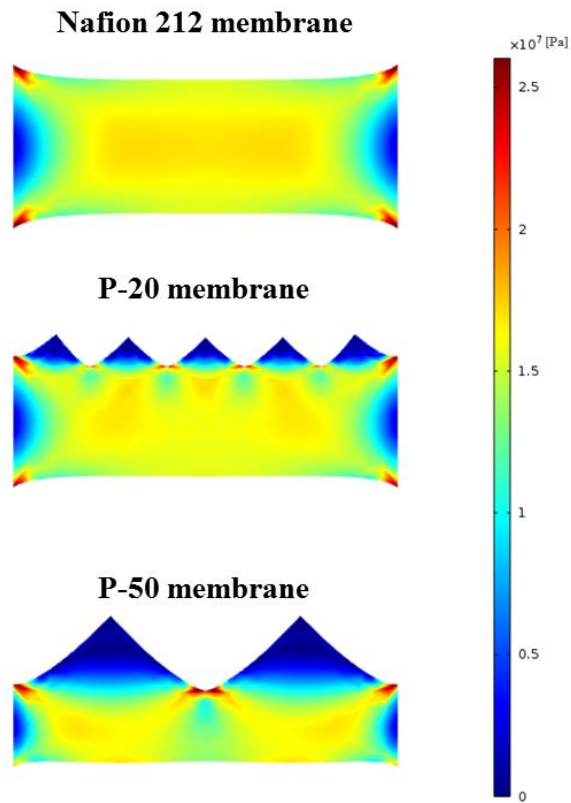


Figure 4.1 Simulation results for the stress distribution on a Nafion 212 membrane and prism-patterned membranes with pitches of 20 μm and 50 μm .

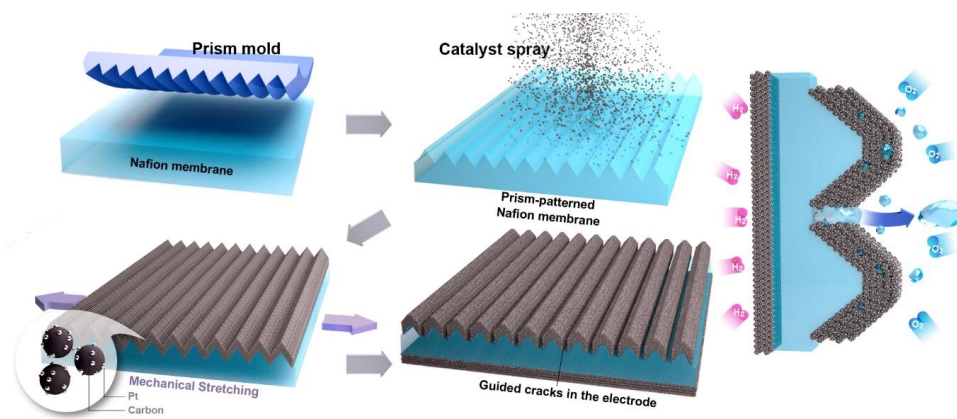


Figure 4.2 Schematic illustration of guided crack generation in an electrode by stretching the prism-patterned membrane electrode assembly.

4.3.2. Physical properties of the prism-patterned Nafion membrane

To investigate the mechanical properties of prism-patterned Nafion membranes, we conducted uniaxial tensile strength tests on a pristine Nafion 212 membrane (thickness of $\sim 50\ \mu\text{m}$) and Nafion membranes with microprism patterns with a $20\ \mu\text{m}$ pitch (P-20 membrane) and a $50\ \mu\text{m}$ pitch (P-50 membrane). Figures 4.3 (a) and (b) show that the two prism patterns have the same angle ($\sim 45^\circ$). Figure 4.3 (c) shows the stress–strain curves of the prepared membranes. The pristine Nafion 212 membrane shows an elongation to break of $\sim 291\%$ and a maximum tensile strength of $\sim 29.48\ \text{MPa}$. Thus, the Nafion 212 membrane can be elongated by a factor of three with respect to its original length. In the case of the prism-patterned Nafion membranes, the P-20 membrane is stretched to $\sim 260\%$ and the P-50 membrane is stretched to $\sim 245\%$ (until breakage, Table 4.1). The elongation to break values are lower for the prism-patterned Nafion membranes than for the pristine Nafion membrane; however, the prism-patterned membranes still exhibit high elongation properties despite the existence of valleys where the stress is focused. The strain–stress curves for the three cases show that the membranes become plastically deformable when the applied strain is above ~ 0.1 ($\sim 10\%$ elongation). This means that the membranes undergo permanent deformation (incomplete recovery to the original length) in the strain region from a strain value of ~ 0.1 to the break points. In this study, we used a broad plastic deformation region to generate cracks and controlled the crack size by varying the strain (0.5 and 1.0). Figure 4.3 (d) shows the relation between the applied strain and the ratio of altered lengths (height, thickness, and width) after removing the applied strains (0.5, 1.0, and 1.5). The height refers to the length of the membrane in the stretching direction, and the width is the length in the direction orthogonal to the stretching direction. Generally, when a specific material is stretched, the length of the specimen elongates in the stretching direction, whereas the length in the orthogonal direction decreases. To use MEAs with cracked electrodes in square single cells, we sprayed a catalyst

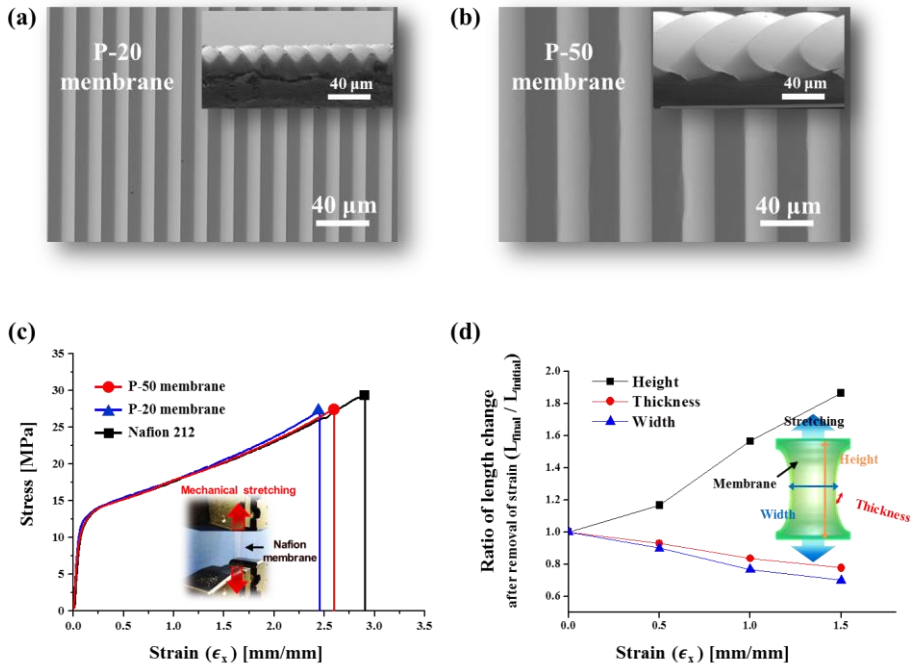


Figure 4.3 (a, b) SEM images of a Nafion membrane imprinted with a prism mould with a pitch of 20 μm (P-20 membrane) (a) and 50 μm (P-50 membrane) (b). (c, d) Stretching properties of the Nafion membranes: (c) strain–stress curves of the Nafion 212 membrane, 20 μm prism-patterned Nafion membrane, and 50 μm prism-patterned Nafion membrane measured by applying strain to the membranes (Inset: optical image showing the operation of the stretching machine); (d) ratio of height, width, and thickness changes of the Nafion membranes with varying strains (~ 0.5 , ~ 1.0 , and ~ 1.5).

Table 4.1 Physical properties of the Nafion membrane.

	Tensile strength, max. [MPa]	Elongation to break [%]
Prism 50 µm	27.61 ^{a)}	260 ^{a)}
Prism 20 µm	27.27 ^{a)}	245 ^{a)}
Nafion 212	29.48 ^{a)} 32.00 ^{b)}	291 ^{a)} 343 ^{b)}

^{a)}Values determined by strain tension tests; ^{b)}General properties of Nafion® PFSA membrane presented by DuPont™. Please refer to www.fuelcellmarkets.com/content/images/articles/nae201.pdf

layer onto rectangular-shaped membranes, considering the length changes of the membranes during stretching.

4.3.3. Morphological features of the generated guided cracks with variation of the strain

To elucidate the geometrical features of the generated cracks in the electrodes on prism patterns, we applied strains (0.5 and 1.0) to the MEAs and observed the morphological changes of the cracks using SEM (Figures 4.4 (a)–(d)). Straight cracks were formed in the prism-line direction for the P-20 and P-50 MEAs. The straight cracks in the electrode were generated by stress concentration in the valley of the prism patterns. The finite elements method (FEM) simulation confirmed that the stresses caused by stretching the MEAs are focused on the electrode surfaces (Figures 4.4 (e) and (f)). However, for a prism pattern with a pitch of $\sim 10\ \mu\text{m}$ (P-10) (Figure 4.5), the formed cracks were randomly distributed compared with those for the P-50 and P-20 MEAs. There are two main reasons for the incomplete guided cracks in the P-10 MEA. First, the stresses are not fully concentrated in the valleys because of the low height (proportional to pitch) feature of P-10 relative to the electrode thickness. Second, when applying the same magnitude of stress (strain), the stress is more geometrically distributed on the P-10 MEA because the number of valleys on the P-10 MEA is five and two times larger than those on the P-50 and P-20 MEAs, respectively. These results imply that we should simultaneously consider the pitch size of the prism pattern and the electrode thickness to generate well-guided cracks.

To investigate the morphological features of the fully guided cracks of the P-20 and P-50 MEAs, we analysed the corresponding SEM images for each strain and pattern dimension. For an applied strain of ~ 0.5 , the average crack width in the P-20 MEA was $\sim 2.1\ \mu\text{m}$ and that in the P-50 MEA was $\sim 5.3\ \mu\text{m}$. Further, the areal

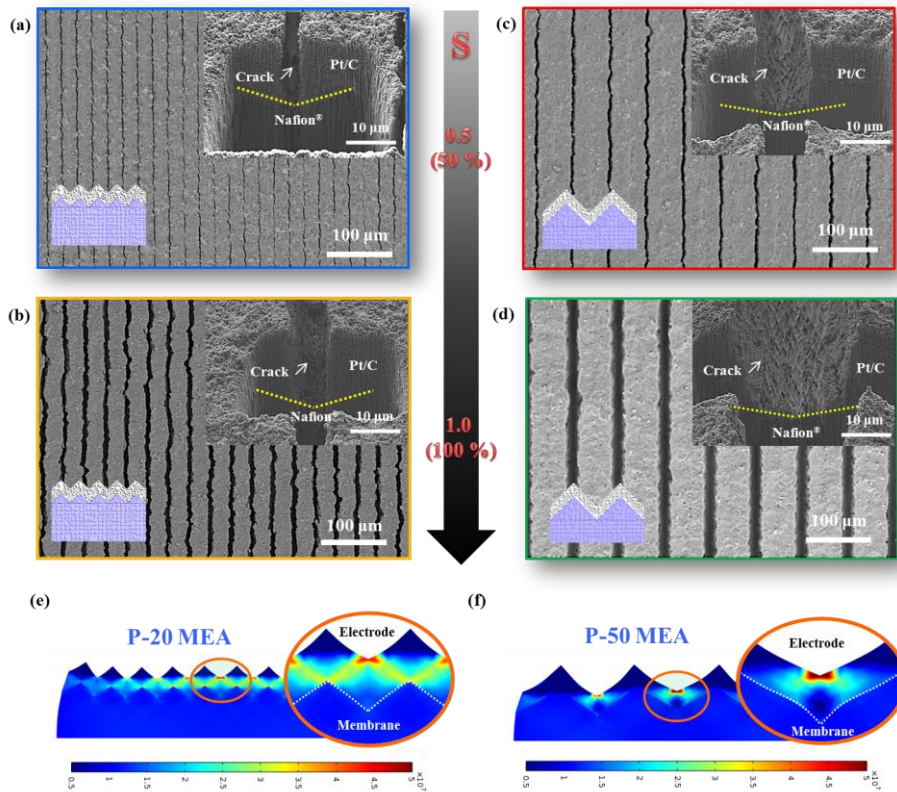


Figure 4.4 Morphological features of the generated guided cracks: (a–d) SEM images of the cracks generated after applying strains (S) of ~ 0.5 and ~ 1.0 to the prism-patterned MEAs with pitches of 20 μm and 50 μm : (a) P-20 MEA with $S \approx 0.5$, (b) P-20 MEA with $S \approx 1.0$, (c) P-50 MEA with $S \approx 0.5$, and (d) P-50 MEA with $S \approx 1.0$. (e, f) Simulations of the stress distributions on the prism-patterned MEAs with pitches of 20 μm (e) and 50 μm (f).

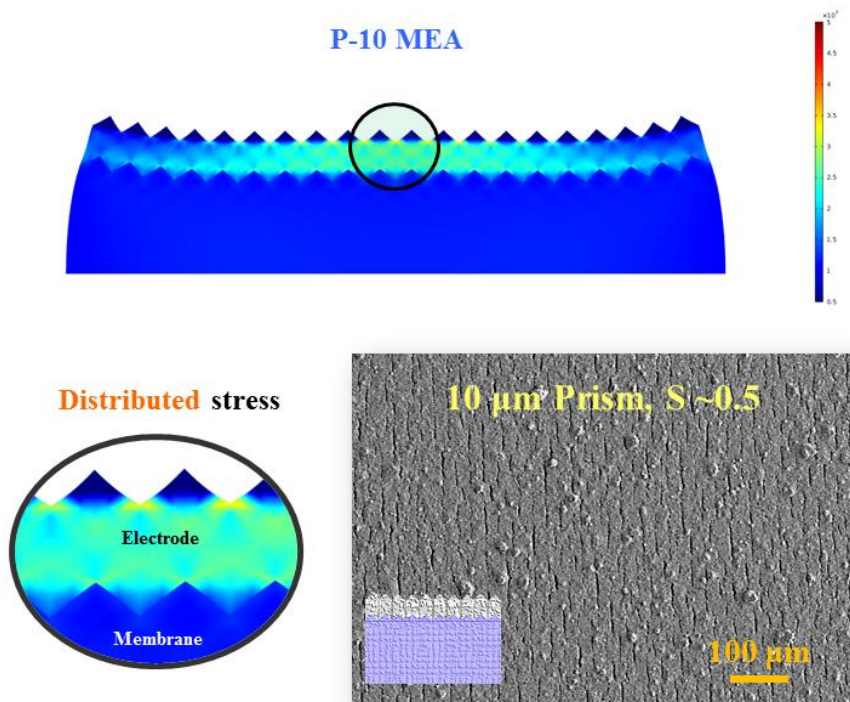


Figure 4.5 Simulation of the stress distribution on a prism-patterned MEA with a pitch of 10 μm and an applied strain of ~ 0.5 , and the corresponding SEM image.

fractions of the two samples were almost the same (~8.0%). When the applied strain was increased to ~1.0, the crack widths were enlarged. The average width in the P-20 MEA was ~8.4 μm and that in the P-50 MEA was ~21 μm , with areal fractions of 19.42%. The average width is proportional to the pattern dimension (pitch of the prism pattern), and the areal fraction of cracks increases proportionally as the applied strain increases. With the same amount of catalyst loading, the thickness of the electrode increases as the areal fraction of the cracks increases, as confirmed by observing cross-sectional SEM images (Figure 4.6). As the applied strain increased, the area of exposed bare Nafion surface increased and this resulted in decrease of areal fraction of the electrode area. In our experiments, we used the same amount of catalyst and thus the electrode thickness increased by ~14% and ~24% for strains of ~0.5 and ~1.0, respectively.

4.3.4. Behavior of water on the cracked electrode

Figure 4.7 shows schematic illustrations of how generated water behaves in the controlled cracks in the catalyst layer. The water behaviour can be divided into three major steps. First, the generated water inside the catalyst layer moves to the surface of the catalyst layer and the cracks. Next, water droplets form and grow by coalescing with neighbouring drops and the cracks fill with liquid water. After filling the cracks in the electrode, droplets arise from the cracks and become larger by coalescing with neighbouring droplets, and are finally ejected to the gas diffusion layer. To visually demonstrate the role of the cracked electrode, we directly observed the water behaviour on the surface of the cracked electrode using *in-situ* ESEM (Figure 4.8). When the RH reaches 95%, a liquid water droplet forms and the cracks fill with liquid water (white dotted circles in Figure 4.8 (a)) within 1 min. After approximately 180 s, droplets arise from the cracks (yellow dotted circles in Figure 4.8 (b)) and grow by coalescing with neighbouring droplets (Figure 4.8 (c) and movie clip available online). From these observations, we

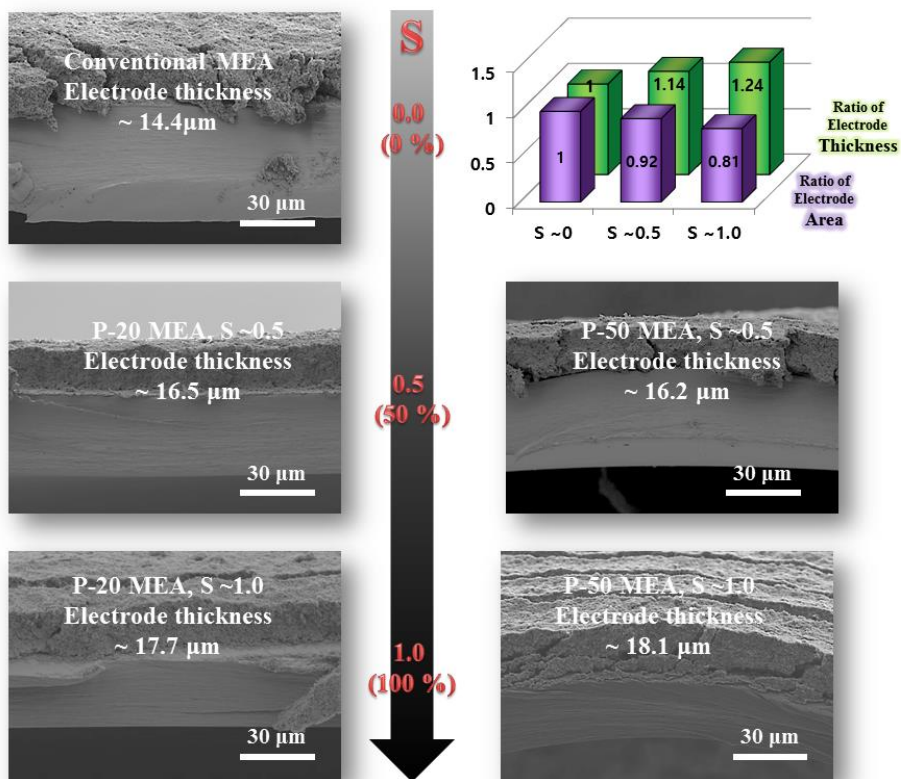


Figure 4.6 Cross-sectional SEM images of the P-20 and P-50 MEAs with $S \approx 0.5$ and 1.0, and a conventional MEA.

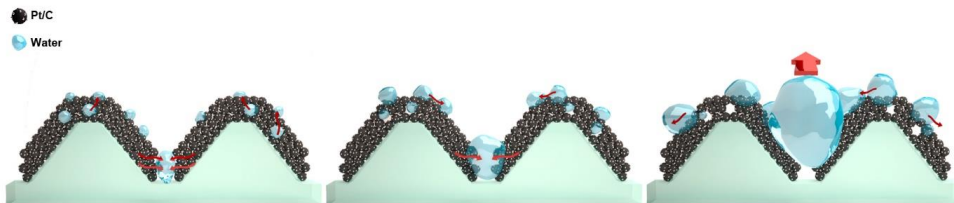


Figure 4.7 Schematic illustrations of the behaviour of generated water in the controlled cracks in the catalyst layer.

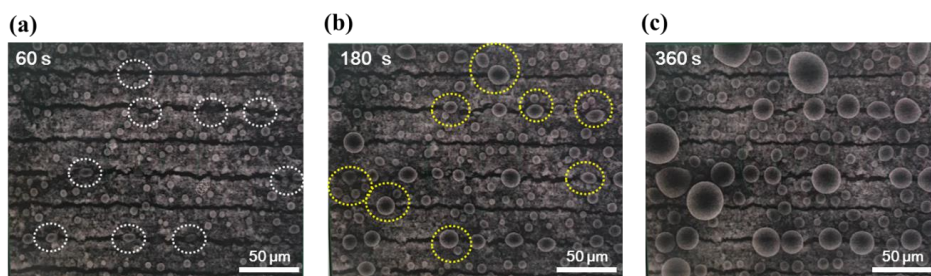


Figure 4.8. ESEM images of water behaviour on a 20 μm cracked catalyst layer (strain ≈ 0.5) with respect to time: (a) 60 s, (b) 180 s, and (c) 360 s. The chamber pressure and substrate temperature were maintained at ~ 5.1 Torr and ~ 2 $^{\circ}\text{C}$, respectively (RH = 95%).

confirmed that the guided cracks in the electrodes act as water reservoirs and also as water passages. These properties are desirable for enhancing fuel cell performance by reducing mass transport resistance.

4.3.5. Enhanced performance using cracked MEAs in PEFCs

To elucidate the effect of the guided cracks on PEFC performance, we constructed single cells by incorporating guided cracked MEAs. The single cells with guided cracked MEAs were operated by flowing fully humidified H₂/air to the anode/cathode. The experimental sets were composed of P-20 and P-50 MEAs with applied strains of ~ 0.5 and ~ 1.0 , respectively. These MEAs exhibit enhanced performance mainly because of the improved water transport under all conditions, regardless of the dimension of the prism pattern and the applied strain, relative to that of the conventional MEA (Figure 4.9 and Figure 4.10). The performance improvement of the P-20 MEA is higher than that of the P-50 MEA with the same applied strain ($S \approx 0.5$ and 1.0). Considering that the same applied strain indicates an analogous areal fraction of generated cracks, improved performance can be obtained by increasing the number of guided cracks. The performance with an applied strain of ~ 1.0 is lower than that with an applied strain of ~ 0.5 for the P-20 and P-50 MEAs. The MEAs with $S \approx 0.5$ show higher performance than the MEAs with $S \approx 1.0$, which can be explained by the morphological features of the stretched MEA. Generally, the interface between the Nafion membrane and the electrode is the site where the electrochemical reaction is most effective.²⁷ However, as more strain was applied to the MEA, the area of the bare Nafion membrane surface (without contact with the catalyst layer) increased, which reduced the electrochemical reaction and reduced the device performance for the MEAs with $S \approx 1.0$. In addition, as mentioned above, MEAs with $S \approx 1.0$ have thicker electrodes than $S \approx 0.5$, which could also lead to reduced performance. These results indicate that there exists a desirable crack density and applied strain

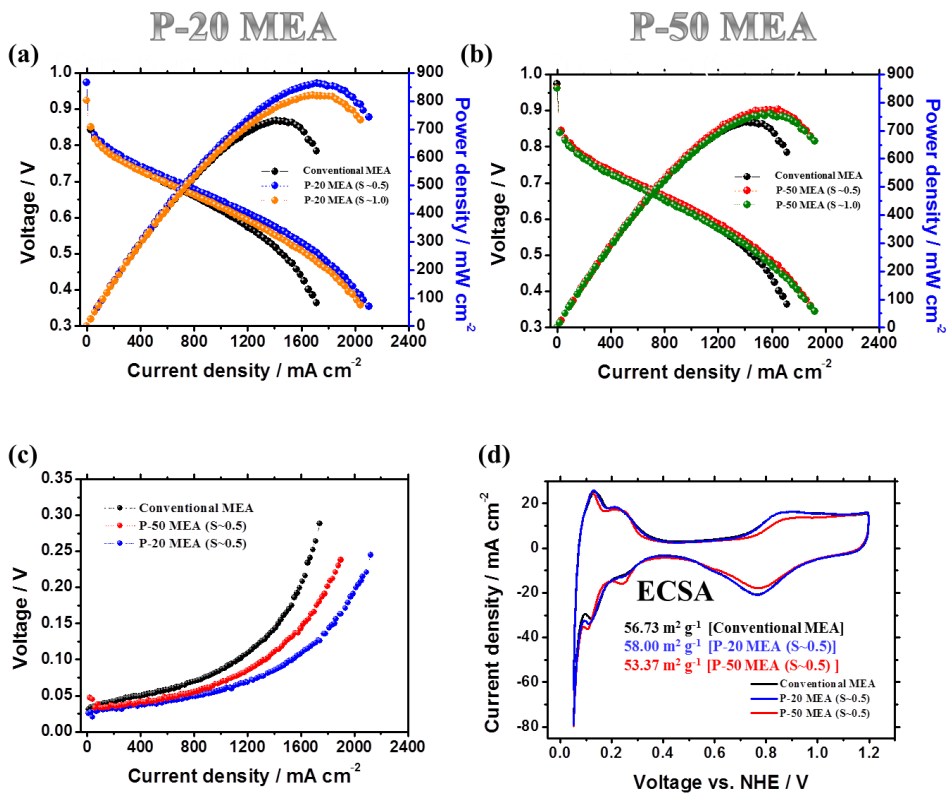


Figure 4.9 Electrochemical measurements of the MEAs: (a, b) Polarization curves of a conventional MEA and the MEAs with cracks generated using a 20 μm prism pattern (a) and a 50 μm prism pattern (b) with various strains (~ 0.5 and ~ 1.0) under H_2/air . (c) Oxygen gains obtained under ambient pressure. (d) Cyclic voltammetry (CV) measurements of the prism-patterned MEAs with the same strain (~ 0.5) and a conventional MEA at the cathode catalyst layers (NHE = normal hydrogen electrode).

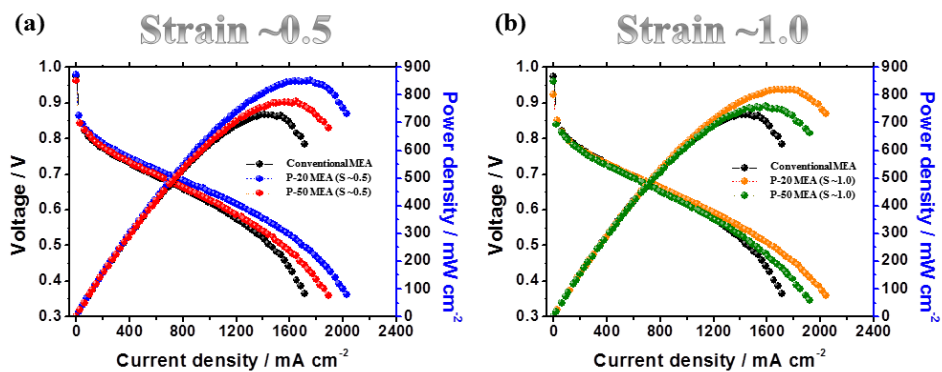


Figure 4.10 Measurements of device performance: (a, b) Polarization curves of a conventional MEA, P-20 MEA, and P-50 MEA with the same applied strain of ~0.5 (a) and ~1.0 (b) under H₂/air.

to obtain a high-performance MEA. In our experiments, the P-20 MEA with an applied strain of ~ 0.5 shows the highest performance, with a maximum power density of $\sim 863 \text{ mW cm}^{-2}$ and a current density of $\sim 1,272 \text{ mA cm}^{-2}$ at 0.6 V under H_2/air . This maximum power density is $\sim 18\%$ higher than the conventional value ($\sim 730 \text{ mW cm}^{-2}$) (Table 4.2).

To further confirm the degree of mass transfer at the cathode catalyst, we calculated the oxygen gain (ΔV) using the following equation:^{14, 28}

$$\Delta V = V_{(\text{H}_2/\text{O}_2)} - V_{(\text{H}_2/\text{air})} \quad (1)$$

The oxygen gain values of the MEAs with guided cracks are smaller than that of the reference MEA, and the difference increases as the current density increases (Figure 4.9 (c)). The P-20 MEA ($S \approx 0.5$) shows the highest performance among the prepared MEAs, which implies that the guided cracks in the MEA enhance mass transport relative to that in the conventional MEA. We also measured the device performance of an MEA using a pre-stretched membrane while excluding the thinning effect of the stretched membrane, as shown in Figure 4.11. The prism-patterned Nafion membrane was previously stretched (P-20 membrane with $S \approx 0.5$) before spraying the catalyst. Then, the catalyst ink was sprayed onto the pre-stretched membrane to construct the MEA. In this manner, the MEA with a pre-stretched membrane was prepared with no cracks in the cathode but it contained a thinned membrane. The performance of the MEA with the pre-stretched membrane is slightly higher than that of the conventional MEA. This is because the vertically asymmetric geometrical feature at the interface between Nafion membrane and catalyst layer lead to improved water transport.²⁸ However, it showed still much lower performance than that of the P-20 MEA with guided cracks under H_2/air , which indicates that the guided cracks has an effective role to enhance the device performance.

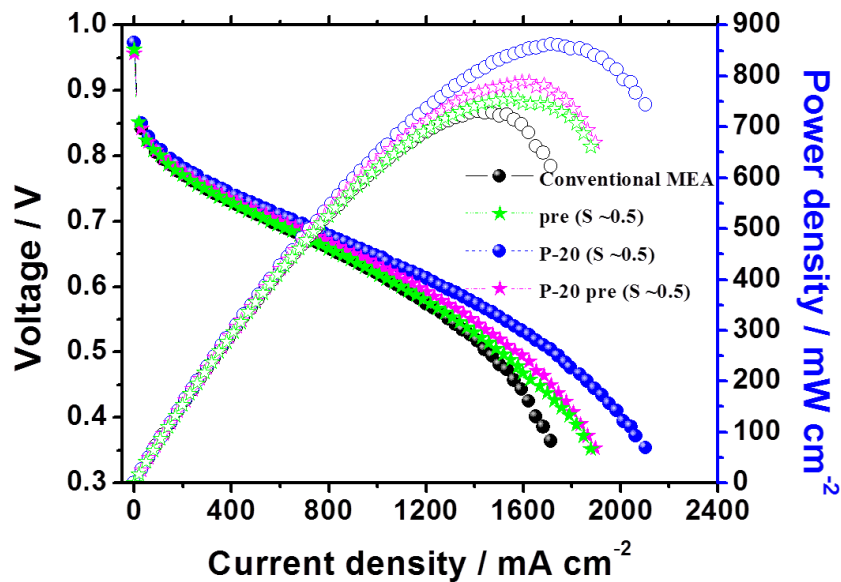
4.3.6. Electrochemical analysis of the MEA with guided cracks

To quantitatively investigate the effects of enhanced water transport, EIS and CV

Table 4.2 Maximum power densities and current densities at 0.6 V for the prism-patterned MEAs.

	P-20 MEA		P-50 MEA	
	Current density at 0.6 V [mA cm ⁻²]	Max. power density [mW cm ⁻²]	Current density at 0.6 V [mA cm ⁻²]	Max. power density [mW cm ⁻²]
Strain ~0.5	1,272	863	1,140	781
Strain ~1.0	1,162	821	1,079	764

^{a)}Conventional MEA: current density of 1,008 mA cm⁻² at 0.6 V and max. power density of 730 mW cm⁻²



	Current density at 0.6 V (mA cm ⁻²)	Max. Power density (mW cm ⁻²)
Conventional MEA	1,084	730
Pre (S~0.5)	1,098	755
P-20 (S ~0.5)	1,282	865
P-20 pre (S ~0.5)	1,166	794

Figure 4.11 Polarization curves of conventional MEA, MEA with pre-stretched membrane (S ~0.5), P-20 patterned MEA with pre-stretched membrane (S ~0.5) and P-20 patterned MEA with controlled cracks via stretching MEA (S ~0.5)

were performed for the P-20 and P-50 MEAs with an applied strain of ~ 0.5 and compared with the respective data for a conventional MEA (Figure 4.9 (d) and Figure 4.12). Electrochemical active surface areas (ECSAs) were obtained from the CV measurements.²⁹ The measured ECSAs of the conventional MEA ($56.73 \text{ m}^2 \text{ g}^{-1}$), P-20 MEA with $S \approx 0.5$ ($58.00 \text{ m}^2 \text{ g}^{-1}$), and P-50 MEA with $S \approx 0.5$ ($53.37 \text{ m}^2 \text{ g}^{-1}$) are comparable, which shows that the area of the tri-phase boundary is barely affected by the guided cracks. The EIS data for the three samples were obtained at 0.6 V and fitted to the equivalent circuit, as illustrated in Figure 4.12.³⁰⁻³² The P-20 and P-50 MEAs with $S \approx 0.5$ show comparable ohmic resistances of $0.0637 \text{ } \Omega \text{ cm}^2$ and $0.0609 \text{ } \Omega \text{ cm}^2$, respectively (that of the conventional MEA is $0.0631 \text{ } \Omega \text{ cm}^2$). Even though the current densities of the cracked MEAs are higher than that of the conventional MEA at 0.6 V, the Warburg impedance values of the P-20 MEA ($0.02026 \text{ } \Omega \text{ cm}^2$) and P-50 MEA ($0.03817 \text{ } \Omega \text{ cm}^2$) with $S \approx 0.5$ are much smaller than that of the conventional MEA ($0.09565 \text{ } \Omega \text{ cm}^2$) (Table 4.3). Moreover, in the high current density region ($\sim 1.6 \text{ A cm}^{-2}$), the difference between the Warburg impedance values for the P-20 MEA with $S \approx 0.5$ ($0.0326 \text{ } \Omega \text{ cm}^2$) and the conventional MEA ($0.3702 \text{ } \Omega \text{ cm}^2$) increases (Table 4.3 and Figure 4.12 (b)). These results imply that water transport at the cathode catalyst layer is substantially improved by the cracks, especially for P-20 MEA, providing high device performance.

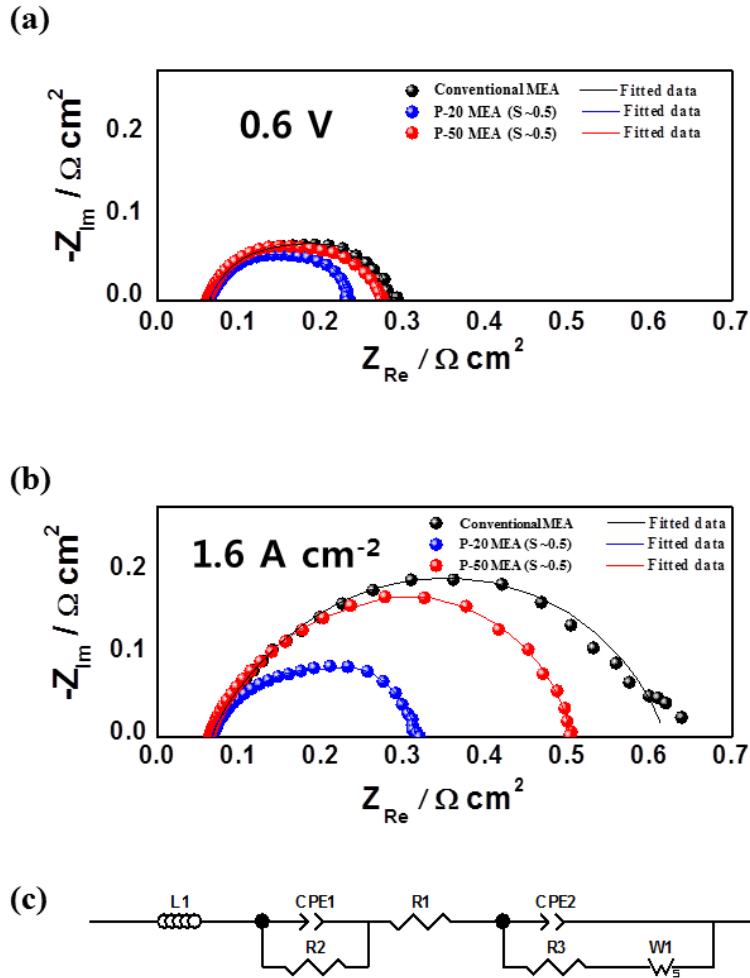


Figure 4.12 Electrochemical impedance spectroscopy (EIS) measurements of prism-patterned MEAs with the same strain (~ 0.5) and a conventional MEA at 0.6 V vs. a reversible hydrogen electrode (a) and at 1.6 A cm^{-2} (b). (c) Equivalent circuit of the PEFC ($L1$ = inductance of the electric wire, $R1$ = internal membrane resistance, $R3$ (2) = charge transfer resistance of the cathode (anode), $CPE2$ (1) = constant phase element of the cathode (anode), and $W1$ = Warburg impedance).

Table 4.3 Electrochemical impedance spectroscopy (EIS) fitted data.

	EIS at 0.6 V		EIS at 1.6 A cm ⁻²	
	R_{membrane} [Ω cm ²]	Z_w (Warburg) [Ω cm ²]	R_{membrane} [Ω cm ²]	Z_w (Warburg) [Ω cm ²]
Conventional MEA	0.0631 (100%)	0.09565 (100%)	0.0660 (100%)	0.3702 (100%)
P-20 MEA with $S \approx$ 0.5	0.0637 (101.0%)	0.02026 (21.2%)	0.0657 (99.5%)	0.0326 (8.8%)
P-50 MEA with $S \approx$ 0.5	0.0609 (96.5%)	0.03817 (39.9%)	0.0629 (95.3%)	0.0328 (8.8%)

4.4. Conclusions

In this study, we achieved enhanced device performance by incorporating guided cracks into a porous electrode by stretching the catalyst-coated membrane to improve water transport. We successfully generated guided cracks using the concentrated surface stress in an electrode with a prism-patterned Nafion membrane. We investigated the effects of crack size and the areal fraction of cracks on device performance by varying the dimension of the pattern (prism pitches of 20 μm and 50 μm) and the applied strain ($S \approx 0.5$ and 1.0). We found that the guided cracks in the electrodes have effective roles as generated water reservoirs and as water passages by observing the behaviour of the generated water in the guided and cracked electrodes using *in-situ* ESEM. We incorporated MEAs with guided cracks into single cells to examine the electrochemical performance. Under all conditions (regardless of the prism pattern dimension and applied strain), the MEAs with controlled cracks exhibited improved performance. In particular, the maximum power density of P-20 MEA (with an applied strain of ~ 0.5) increased by $\sim 18\%$ relative to that of the conventional MEA. The guided cracks in the electrode effectively enhanced water transport on the cathode side, as confirmed by EIS measurements. Our strategy to generate controlled voids, i.e. cracks in the electrode, is a very effective way to improve mass transport in fuel cells and shows the potential to be applied in other energy storage and conversion devices. However, there would be manufacturing issue of our process including the morphology distortion during stretching process and adaptability to commercialized MEAs with large area. Hence, proper design of the stretcher machine and initially sprayed region should be further investigated. In addition, Uniform cracks were observed in the MEA with prism-pattern, but the performance was higher in the MEA with random cracks than the conventional MEA. Although the shape of the cracks in the MEA with the pattern has been obtained uniformly, the cracks in the longitudinal direction are considered to have adverse effects on

performance. When the cracks are formed in a small and dense shape like random cracks in the MEA, it seems to be advantageous for mass transfer because the utilization of cracks is increased.

4.5. References

- 1 Jang, J.-M., Park, G.-G., Sohn, Y.-J., Yim, S.-D., Kim, C.-S. & Yang, T.-H. The analysis on the activation procedure of polymer electrolyte fuel cells. *J. Electrochem. Sci. Technol.* **2**, 131–135 (2011).
- 2 Zhang, H. & Shen, P. K. Advances in the high performance polymer electrolyte membranes for fuel cells. *Chem. Soc. Rev.* **41**, 2382–2394 (2012).
- 3 Gasteiger, H. A. & Marković, N. M. Just a dream—Or future reality? *Science* **324**, 48–49 (2009).
- 4 Stephens, I. E. L., Bondarenko, A. S., Grønbjerg, U., Rossmeisl, J. & Chorkendorff, I. Understanding the electrocatalysis of oxygen reduction on platinum and its alloys. *Energy Environ. Sci.* **5**, 6744–6762 (2012).
- 5 Hsieh, B.-J., Tsai, M.-C., Pan, C.-J., Su, W.-N., Rick, J., Lee, J.-F., Yang, Y.-W. & Hwang, B.-J. Platinum loaded on dual-doped TiO₂ as an active and durable oxygen reduction reaction catalyst. *NPG Asia Mater.* **9**, e403 (2017).
- 6 Jung, N., Bhattacharjee, S., Gautam, S., Park, H.-Y., Ryu, J., Chung, Y.-H., Lee, S.-Y., Jang, I., Jang, J. H., Park, S. H., Chung, D. Y., Sung, Y.-E., Chae, K.-H., Waghmare, U. V., Lee, S.-C. & Yoo, S. J. Organic-inorganic hybrid PtCo nanoparticle with high electrocatalytic activity and durability for oxygen reduction. *NPG Asia Mater.* **8**, e237 (2016).
- 7 Park, T., Kang, Y. S., Jang, S., Cha, S. W., Choi, M. & Yoo, S. J. A rollable ultra-light polymer electrolyte membrane fuel cell. *NPG Asia Mater.* **9**, e384 (2017).
- 8 Slade, S., Campbell, S. A., Ralph, T. R. & Walsh, F. C. Ionic conductivity of an extruded Nafion 1100 EW series of membranes. *J. Electrochem. Soc.* **149**, A1556–A1564 (2002).
- 9 Cho, H., Kim, S. M., Kang, Y. S., Kim, J., Jang, S., Kim, M., Park, H.,

- Bang, J. W., Seo, S., Suh, K.-Y., Sung, Y.-E. & Choi, M. Multiplex lithography for multilevel multiscale architectures and its application to polymer electrolyte membrane fuel cell. *Nat. Commun.* **6**, 8484 (2015).
- 10 Kim, S. M., Ahn, C.-Y., Cho, Y.-H., Kim, S., Hwang, W., Jang, S., Shin, S., Lee, G., Sung, Y.-E. & Choi, M. High-performance fuel cell with stretched catalyst-coated membrane: One-step formation of cracked electrode. *Sci. Rep.* **6**, 26503 (2016).
- 11 Sinha, P. K., Mukherjee, P. P. & Wang, C.-Y. Impact of GDL structure and wettability on water management in polymer electrolyte fuel cells. *J. Mater. Chem.* **17**, 3089–3103 (2007).
- 12 Jung, N., Kim, S. M., Kang, D. H., Chung, D. Y., Kang, Y. S., Chung, Y.-H., Choi, Y. W., Pang, C., Suh, K.-Y. & Sung, Y.-E. High-performance hybrid catalyst with selectively functionalized carbon by temperature-directed switchable polymer. *Chem. Mater.* **25**, 1526–1532 (2013).
- 13 Li, H., Tang, Y., Wang, Z., Shi, Z., Wu, S., Song, D., Zhang, J., Fatih, K., Zhang, J., Wang, H., Liu, Z., Abouatallah, R. & Mazza, A. A review of water flooding issues in the proton exchange membrane fuel cell. *J. Power Sources* **178**, 103–117 (2008).
- 14 Jang, S., Kim, M., Kang, Y. S., Choi, Y. W., Kim, S. M., Sung, Y.-E. & Choi, M. Facile multiscale patterning by creep-assisted sequential imprinting and fuel cell application. *ACS Appl. Mater. Interfaces* **8**, 11459–11465 (2016).
- 15 Zhang, X. & Shi, P. Dual-bonded catalyst layer structure cathode for PEMFC. *Electrochem. Commun.* **8**, 1229–1234 (2006).
- 16 Friedmann, R. & Van Nguyen, T. Optimization of the microstructure of the cathode catalyst layer of a PEMFC for two-phase flow. *J. Electrochem. Soc.* **157**, B260–B265 (2010).
- 17 Jung, N., Cho, Y.-H., Ahn, M., Lim, J. W., Kang, Y. S., Chung, D. Y., Kim,

- J., Cho, Y.-H. & Sung, Y.-E. Methanol-tolerant cathode electrode structure composed of heterogeneous composites to overcome methanol crossover effects for direct methanol fuel cell. *Int. J. Hydrogen Energy* **36**, 15731–15738 (2011).
- 18 Kim, O.-H., Cho, Y.-H., Kang, S. H., Park, H.-Y., Kim, M., Lim, J. W., Chung, D. Y., Lee, M. J., Choe, H. & Sung, Y.-E. Ordered macroporous platinum electrode and enhanced mass transfer in fuel cells using inverse opal structure. *Nat. Commun.* **4**, 2473 (2013).
- 19 Zhao, J., He, X., Wang, L., Tian, J., Wan, C. & Jiang, C. Addition of NH_4HCO_3 as pore-former in membrane electrode assembly for PEMFC. *Int. J. Hydrogen Energy* **32**, 380–384 (2007).
- 20 Cho, Y.-H., Jung, N., Kang, Y. S., Chung, D. Y., Lim, J. W., Choe, H., Cho, Y.-H. & Sung, Y.-E. Improved mass transfer using a pore former in cathode catalyst layer in the direct methanol fuel cell. *Int. J. Hydrogen Energy* **37**, 11969–11974 (2012).
- 21 Vandeparre, H., Liu, Q., Mineev, I. R., Suo, Z. & Lacour, S. P. Localization of folds and cracks in thin metal films coated on flexible elastomer foams. *Adv. Mater.* **25**, 3117–3121 (2013).
- 22 Kim, B. C., Matsuoka, T., Moraes, C., Huang, J., Thouless, M. D. & Takayama, S. Guided fracture of films on soft substrates to create micro/nano-feature arrays with controlled periodicity. *Sci. Rep.* **3**, 3027 (2013).
- 23 Choi, Y. W., Kang, D., Pikhitsa, P. V., Lee, T., Kim, S. M., Lee, G., Tahk, D. & Choi, M. Ultra-sensitive pressure sensor based on guided straight mechanical cracks. *Sci. Rep.* **7**, 40116 (2017).
- 24 Wang, L., Ji, X.-Y., Wang, N., Wu, J., Dong, H., Du, J., Zhao, Y., Feng, X.-Q. & Jiang, L. Biaxial stress controlled three-dimensional helical cracks. *NPG Asia Mater.* **4**, e14 (2012).

- 25 Kang, D., Pikhitsa, P. V., Choi, Y. W., Lee, C., Shin, S. S., Piao, L., Park, B., Suh, K.-Y., Kim, T.-i. & Choi, M. Ultrasensitive mechanical crack-based sensor inspired by the spider sensory system. *Nature* **516**, 222–226 (2014).
- 26 Kim, H.-N., Lee, S.-H. & Suh, K.-Y. Controlled mechanical fracture for fabricating microchannels with various size gradients. *Lab Chip* **11**, 717–722 (2011).
- 27 Aizawa, M., Gyoten, H., Salah, A. & Liu, X. Pillar structured membranes for suppressing cathodic concentration overvoltage in PEMFCs at elevated temperature/low relative humidity. *J. Electrochem. Soc.* **157**, B1844–B1851 (2010).
- 28 Kim, S. M., Kang, Y. S., Ahn, C., Jang, S., Kim, M., Sung, Y.-E., Yoo, S. J. & Choi, M. Prism-patterned Nafion membrane for enhanced water transport in polymer electrolyte membrane fuel cell. *J. Power Sources* **317**, 19–24 (2016).
- 29 Gouws, S. in *Electrolysis* (eds. Kleperis, J. & Linkov, V.) Ch. 5 (InTech, 2012).
- 30 Yuan, X., Wang, H., Sun, J. C. & Zhang, J. AC impedance technique in PEM fuel cell diagnosis—A review. *Int. J. Hydrogen Energy* **32**, 4365–4380 (2007).
- 31 Kulikovskiy, A. A. One-dimensional impedance of the cathode side of a PEM fuel cell: Exact analytical solution. *J. Electrochem. Soc.* **162**, F217–F222 (2015).
- 32 Niya, S. M. R. & Hoorfar, M. Study of proton exchange membrane fuel cells using electrochemical impedance spectroscopy technique—A review. *J. Power Sources* **240**, 281–293 (2013).
- 33 Anandarajah, A. *Computational Methods in Elasticity and Plasticity: Solids and Porous Media* (Springer Science & Business Media, New York, NY, USA, 2010).

- 34 Kim, S., Kim, J.-H., Oh, J.-G., Jang, K.-L., Jeong, B.-H., Hong, B. K. & Kim, T.-S. Mechanical behavior of free-standing fuel cell electrodes on water surface. *ACS Appl. Mater. Interfaces* **8**, 15391–15398 (2016).

Chapter 5. Effect of N-doped Carbon Coatings on the Durability of Highly loaded Platinum and Alloy Catalysts with Different Carbon Supports for Polymer Electrolyte Membrane Fuel Cells

5.1. Introduction

Platinum (Pt) is commonly employed in fuel cell catalysts for electrochemical reactions such as the oxygen reduction reaction (ORR), and has been widely applied in fuel cell research due to its intrinsic high activity.[1] In addition, a reduction in the size of the Pt particles to nanoscale dimensions and dispersion of the resultant nanoparticles onto high surface area supports has significantly increased its utilisation.[2] Furthermore, studies have been conducted to increase catalyst activity and reduce the quantity of Pt required by creating alloys between Pt and transition metals.[3–6] Moreover, in the context of supports for fuel cell catalysts, a low electrical resistance and a high stability are required to withstand fuel cell operating conditions. Hence, carbon supports such as Vulcan XC and Ketjen Black are commonly employed.[7]

Due to the electrochemically harsh operating conditions of polymer electrolyte membrane fuel cells (PEFCs), research regarding the durability of any materials employed is of particular importance, as degradation of the metal particles dispersed on the carbon supports can occur through migration/dissolution of the metal and corrosion of the carbon itself. As such, significant research has been conducted in this area based on a variety of strategies, such as Pt nanostructure control, alloying, and carbon support modification. For example, Park et al.[8]

synthesised a cubic platinum nanoframe through structural control and reported its improved durability. Furthermore, improvements in durability through the formation of structures composed of platinum-based alloys (e.g., alloys with Ni, Co, and Pd, among others) to give core-shell structures,[9] nanoframes,[10] hollow structures,[11] nanocages,[12] dendrites,[13] and alloys with Pt skins[14,15] have been reported. There have also been reports of increased durability through the replacement of conventional catalyst supports with more robust materials such, as carbon nanotubes (CNTs),[16] graphene,[17–19] carbon composites,[20] and metal oxides.[21–24] In addition, it has been reported[25] that the interaction between Pt and the support is strengthened by the presence of ionic liquids. Support-free catalysts have also been applied to single cells to avoid support corrosion.[26] Recently, durability enhancement studies using a protective layer, such as a metal (tantalum) oxide[27] or carbon layer[28–36] have been applied to Pt- and Pt-alloy catalysts. In particular, when carbon is applied as a protective layer to the surface of the catalyst, the durability of the catalyst is increased by preventing migration and dissolution of the metal. To date, methods for the introduction of such a carbon shell have included vapour-phase and liquid-phase methods based on the use of polyaniline,[28,29] polydopamine,[30–32] ethylenediamine,[33] 1,2-hexadecanediol with iron acetylacetonate,[34] and poly(acrylic acid)(butyl acrylate) [35] for the liquid phase methods, and CH₄, C₂H₂, EtOH, and CH₃COCH₃ for the vapour phase methods.[36] Furthermore, enhanced ORR activity has been reported upon doping the carbon protective layer with nitrogen.[37,38] Originally, nitrogen-doped carbon was extensively studied to replace expensive platinum group catalysts and exhibited good ORR activity with transition metals such as Fe, Co, etc.[39–41] However, studies also found that ORR activity was further enhanced due to the synergistic effects of the nitrogen-doped carbon shell and metal catalyst core and that the stability of the shell was improved.

Most previous studies have introduced a protective shell on a 20 wt% metal

catalyst on support. In these cases, the distance between the metal nanoparticles is long because the total amount of the metal is small compared to the support. Therefore, metal agglomeration is rare during the high temperature heat treatment used to form the carbon shell. However, highly loaded catalysts are often used in practical fuel cell devices to reduce the volume of the electrodes; therefore, the smaller distance between metal nanoparticles means that they can quickly agglomerate, even at low temperatures where the carbon shell is not well formed. Furthermore, in the previous report, the catalysts were only studied at the half-cell level after the introduction of carbon shells.[31,35] Even when a single cell evaluation was carried out, the activity of the catalysts was studied in an oxygen atmosphere[32] or the durability in a nitrogen atmosphere.[29,34]

Thus, we herein report the application of a carbon-based protective layer for highly loaded Pt- and Pt-alloy catalysts on different types of carbon supports, as shown in Figure 5.1, to prevent agglomeration of adjacent metal nano-particles during degradation process and/or heat treatment. In this case, to form the protective layer on the catalyst surface, we employed a dopamine precursor, as the desired shell can be formed rapidly in aqueous solution at room temperature. The prepared catalysts were then applied to a membrane electrolyte assembly (MEA) as cathode electrodes and subjected to single-cell electrochemical analysis in air conditions, similar to the actual operating conditions used in fuel cell applications. We also aim to confirm that the durability of Pt- and Pt-alloy catalysts can be enhanced by the presence of an N-doped carbon shell, and the related phenomenon is explained through examination of the electrochemical performance, the electrochemically active surface area, and comparative analysis of the obtained transmission electron microscopy (TEM) images.

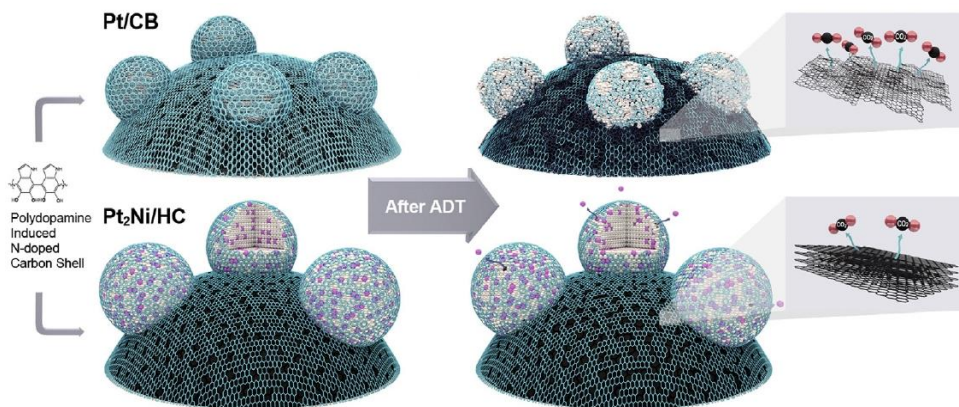


Figure 5.1 Schematic diagram of the N-doped carbon-coated Pt/CB (top) and Pt₂Ni/HC (bottom) systems before and after the accelerated degradation tests (ADTs).

5.2. Experimental section

5.2.1. Preparation of the Dopamine-coated Cathode Catalyst

Commercial 40 wt% Pt on carbon black (CB) (HiSPEC[®] 4000, Alfa Aesar, USA) and 50 wt% Pt₂Ni on carbon (RTCPN50, RTX, Republic of Korea) were employed for the purpose of this study. Heat-treated Ketjen Black carbon (HC) (KB600 JD) was employed as the carbon support for the alloy catalyst. For coating of the dopamine layer, 100 mg of each catalyst was used. Following the preparation of a 10 mM tris-HCl buffer solution (200 ml) at pH 8.5 (Trisma[®] base and 37% hydrochloric acid, Sigma-Aldrich, USA), dopamine hydrochloride (600 mg, Sigma-Aldrich) was dispensed into the solution. Subsequently, each catalyst was added to a beaker containing the prepared dopamine solution, and stirred at 500 rpm for 60 min. The resulting polydopamine was then washed several times with deionised water (DI water) and ethanol (Samchun Chemical, Republic of Korea) using a membrane filter (Advantec[®] C045A047A, Toyo Rosh Kaisha, Ltd., Japan) and dried at 80 °C overnight in a drying oven. After this time, the dried catalysts were allowed to stand at 25 °C for 3 h, separated from the filter paper in an Ar atmosphere in a tube furnace, and subjected to heat treatment at 600 °C (heating at 2 °C min⁻¹) for 2 h. Following cooling under ambient conditions, the catalysts were finally ball-milled to obtain a powder suitable for preparation of the catalyst inks.

5.2.2. Preparation of the MEA

Both before and after dopamine coating, each catalyst was mixed with DI water and isopropyl alcohol in a vial and treated using a homogeniser (VCX130, Sonics & Materials, Inc., USA) for 3 min to produce the catalyst inks. A Nafion[®] ionomer was then added at the desired loading (10–40 wt%) and the system was treated once again using a homogeniser for 3 min. A Nafion[®] 212 membrane (DuPont, USA) was cut into squares measuring 3.3 × 3.3 cm² and the protective films were peeled off. The membrane squares were then soaked in a 1 M H₂O₂ solution at

80 °C for 1 h and washed with DI water, after which they were treated with a 1 M H₂SO₄ solution at 80 °C. Following treatment, the membrane samples were washed once more with DI water and fixed between acrylic frames with square holes measuring 5 cm², then dried for 24 h. The frames were tightly clamped to the stand and the prepared catalyst inks were sprayed onto the membranes using a N₂ gas bomb and a spray gun (Richpen, GP-2, Japan). At the anode side of all MEA samples, ink containing the 40 wt% Pt/CB catalyst was applied, and the desired catalyst ink was applied to the cathode side. A loading of 0.2 mg_{Pt} cm⁻² was employed for both the anode and the cathode. After spraying, the acrylic frames were removed to give MEAs with active areas measuring 5 cm².

5.2.3 Half-Cell Test

To prepare catalyst inks for half-cell test, the catalyst was blended with Nafion[®] ionomer and isopropyl alcohol mixture. The Nafion[®] ionomer were for proton conduction. Each ink was poured on pre-treated glassy carbon electrode (RDE) tip using micro pipette (Eppendorf Korea Ltd.) and this served as the working electrode. Counter electrode and reference electrode were platinum wire and Ag/AgCl, respectively. All these electrode were operated in 0.1 M HClO₄ solution. ORR was measured at 1600 rpm with 10 mV s⁻¹ measuring rate. And the data were collected using RDE device (Auto Lab., USA).

5.2.4. Single Cell Tests

The prepared MEAs were placed in the centre of a single cell (PEM005-1, CNL Energy, Republic of Korea) consisting of two end plates and two bipolar plates. A serpentine channel (1 mm depth) was employed as the flow field for both the anode and the cathode in the bipolar plate. Two pairs of gas diffusion layers (JNT30-A3, JNTG, Republic of Korea) and Teflon gaskets were placed on both sides of each MEA. Single cell tests were then conducted using a fuel cell test station (CNL

Energy, Republic of Korea). The single cells were maintained at 70 °C throughout the experiment and the relative humidity was fixed at 100%. To activate the MEAs, a current load was applied while supplying hydrogen (H₂) (150 standard cubic centimetres; sccm) to the anode and oxygen (O₂) (200 sccm) to the cathode. The current was increased at a rate of 5 mA s⁻¹, and was maintained for 10 min at 5, 10, and 15 A. When the voltage of the single cell dropped below 0.37 V, the current load was removed and the voltage was set to the open circuit voltage (OCV). This process was repeated several times until the voltage and current remained constant, at which point the activation process was stopped and the performance evaluation was conducted. The cathode gas was then changed from O₂ to air (800 sccm) and the initial performances of the MEAs bearing different cathode catalysts were evaluated. This load cycling method was applied for accelerated degradation tests (ADTs) of the cathode catalysts, where the cycle was repeated over 200 h, increasing the current until the voltage reached the OCV (approx. 1.0 V) to 0.35 V. Upon reaching the OCV, these conditions were held for 30 s, and the current was increased at a rate of 5 mA s⁻¹. To measure the electrochemically active surface areas (ECSAs) of the cathodes, cyclic voltammetry (CV) was performed both before and after the ADTs, and H₂ and N₂ were supplied to the anode and the cathode, respectively.

5.2.5. Transmission Electron Microscopy (TEM) Measurements

Two commercial catalysts and two dopamine-coated catalysts were analysed by TEM (FEI TECNAI F20 installed in the Research Institute of Advanced Materials (RIAM)). Cathode catalysts separated from the MEAs after conducting the ADTs for 200 h were also analysed. All samples were dispersed in ethanol (Samchun Chemical, Republic of Korea) and placed using a micropipette on a 200 mesh copper grid coated with lacey carbon (EMS, USA) on filter paper (Advantec® No.2, Toyo Rosh Kaisha, Ltd., Japan). All samples were analysed at 200 kV.

5.3. Results and Discussion

5.3.1. Morphological Analysis Before and After Dopamine Coating

TEM analysis (Figure 5.2) of the commercial catalysts and dopamine-coated catalysts was conducted as described above and the obtained particle size distributions are shown in Figure 5.3. Although a number of aggregates were present, commercial Pt/CB consisted of 3.40 ± 1.04 nm metal particles dispersed uniformly on an amorphous CB support (Figure 5.2 (a)). In contrast, slightly larger alloy particles (8.21 ± 2.27 nm) distributed on HC were observed for the commercial Pt₂Ni/HC catalyst (Figure 5.2 (b)). The formation of a thin dopamine layer can be achieved on the substrate surface through the oxidative self-polymerisation of dopamine in alkaline solution[42] and N-doped carbon shells (1.5–2.3 nm) was formed by following polydopamine heat-treatment (Figure 5.2(c)) in the case of the commercial Pt/CB catalyst. During this process, the thickness of the resulting N-doped carbon shell was determined by the agitation time employed, in addition to the quantity of dopamine, and the surface characteristics of the substrate. For example, when approx. 20 wt% of the metal was loaded onto a carbon support,[30] a thin (approx. 0.5 nm) N-doped carbon shell was formed under the same coating conditions employed herein. In addition, a thicker shell was formed in the case of the Pt/CB catalyst due to differences in the catalyst composition. As the catalyst employed in our study contains 40 wt% Pt, it has a 22% smaller accessible volume than the 20 wt% Pt/CB catalyst. Thus, a thicker coating layer can be formed by the application of the same quantity of coating precursor to a smaller volume of catalyst.

Furthermore, the Pt particle size showed a non-uniform dispersion of 5.52 ± 2.54 nm, which was greater than that of the non-coated sample (Figure 5.2(a)). This is likely due to sintering of the Pt particles during the heating process, as the distance between adjacent particles is shorter. However, catalysts annealed without

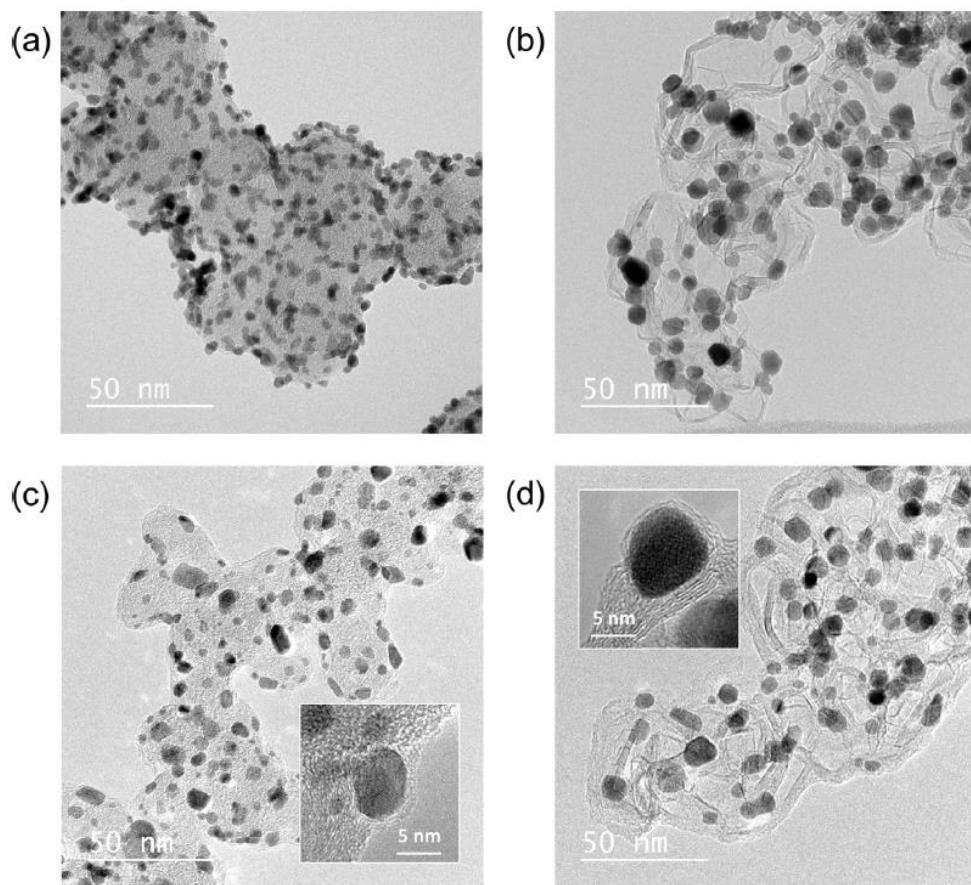


Figure 5.2 TEM images of (a) Pt/CB and (b) Pt₂Ni/HC before dopamine coating, and (c) Pt/CB and (d) Pt₂Ni/HC after dopamine coating. The insets in (c) and (d) show high-resolution TEM images.

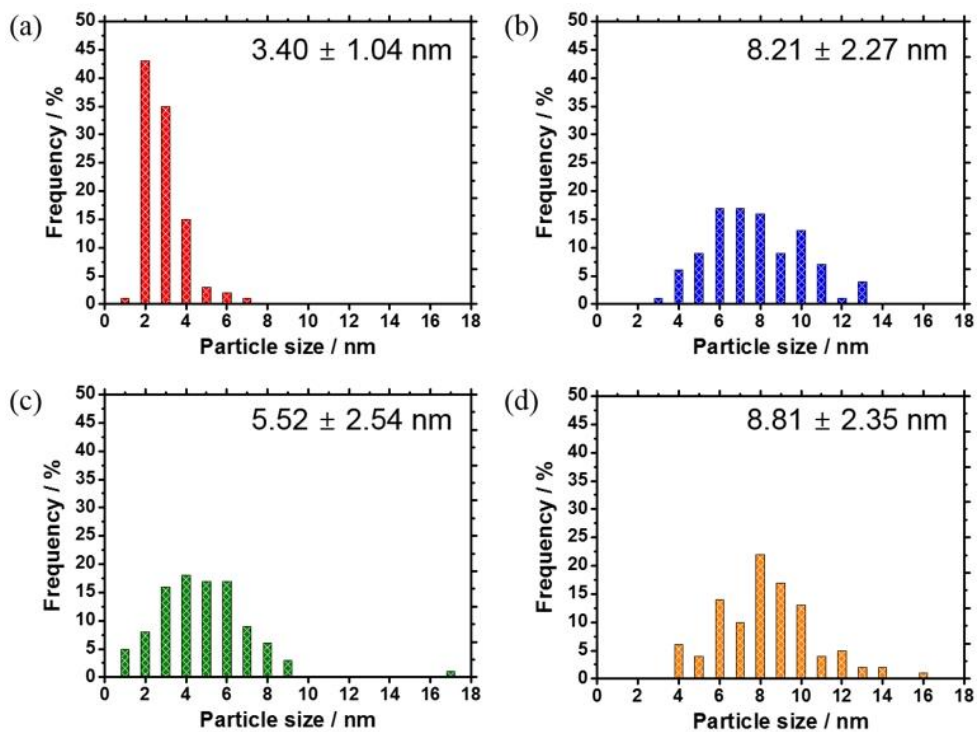


Figure 5.3 Particle size distribution of (a) Pt/CB, (b) Pt₂Ni/HC, (c) Pt/CB with N-doped carbon shell, and (d) Pt₂Ni/HC with N-doped carbon shell before ADT.

additional dopamine coating showed a significant increase in size (Figure 5.4 (a)), whereas no significant increase was observed for the dopamine-coated particles. Upon reducing the agitation time to 45 min in an attempt to reduce the shell thickness, only partial shell formation was observed, as shown in Figure 5.5. This partial shell growth was also accompanied by larger particle growth compared to that observed for the catalysts bearing 1.5–2.3 nm N-doped carbon shells. It was therefore concluded that the minimum time for the formation of an N-doped carbon shell on this catalyst was 1 h, and the minimum shell thickness for sufficient catalyst protection was 1.5–2.3 nm. Figure 5.2 (d) shows an N-doped carbon shell on a Pt₂Ni/HC catalyst. In this case, despite the heat treatment process carried out during coating, little growth of the metal alloy was observed (8.81 ± 2.35 nm) as interactions between Pt and the carbon support were strong due to the enhanced basicity arising from the π sites of the heat-treated carbon. Thus, this catalyst support prevents the migration of metal particles.[43] In contrast, the uncoated Pt₂Ni/HC exhibited significant particle growth following heat treatment, as shown in Figure 5.3 (b), thereby confirming that the dopamine coating prevents growth of the metal particles. In addition, a thinner shell (0.47–0.95 nm) was formed for this catalyst compared to that formed on Pt/CB despite the high metal loading and the use of identical coating conditions. In this context, Sheng et al.[44] reported that heat-treated carbon materials were not dispersible in distilled water, likely due to the increased hydrophobicity of the material. Therefore, as the dopamine layer is polymerised in an aqueous solution, enhanced polymerisation is observed at the CB surface compared to the heat-treated carbon surface due to the hydrophobic nature of the latter, thereby resulting in a thinner coating than that observed for Pt/CB under identical coating conditions (i.e., dopamine quantity and reaction time). As shown in Figure 5.6, the X-ray diffraction results show trends similar to the TEM results. Furthermore, the percentage of nitrogen was slightly lower in Pt₂Ni/HC than in Pt/CB after coating (Figure 5.7).

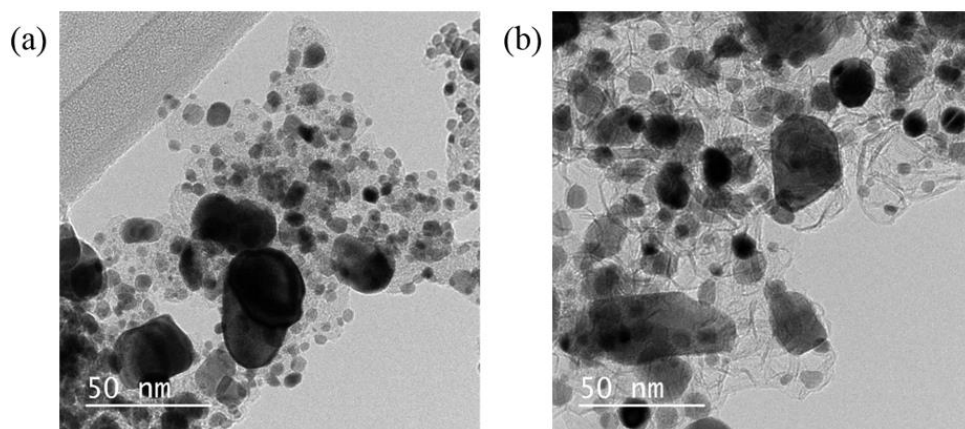


Figure 5.4 TEM images of (a) heat-treated Pt/CB and (b) heat-treated Pt₂Ni/HC without dopamine coating.

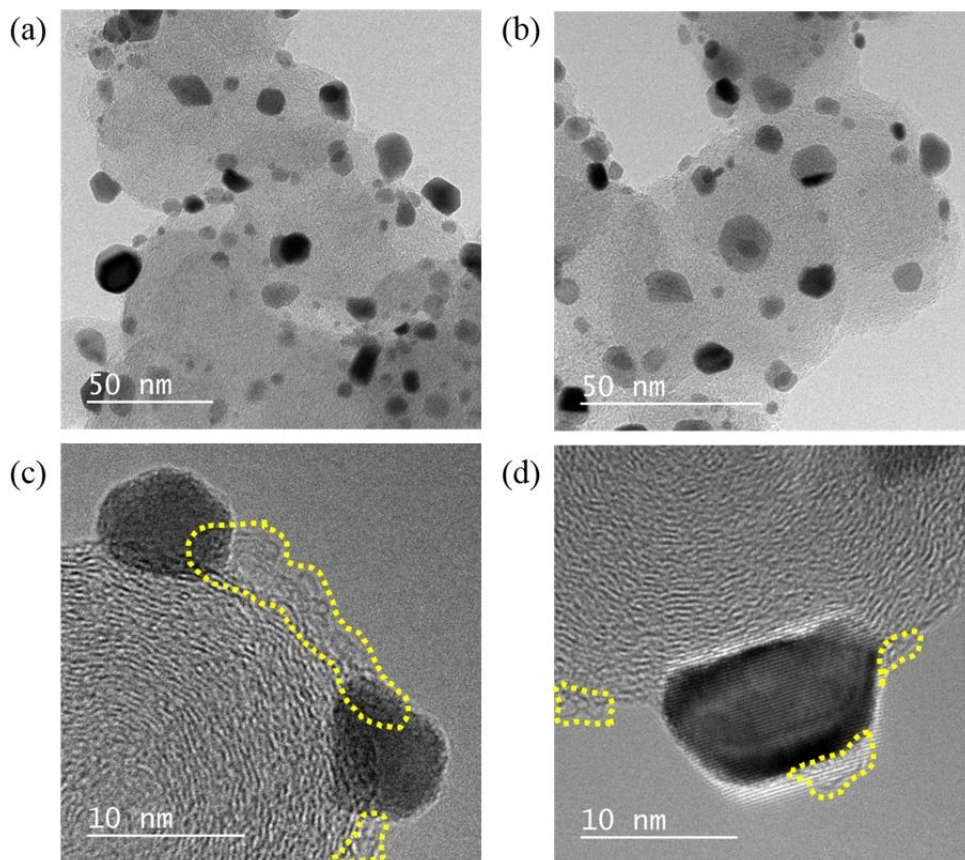


Figure 5.5 TEM images of Pt/CB after 45 min of reaction with dopamine. Inside of the yellow dotted line, carbon shell is partially formed.

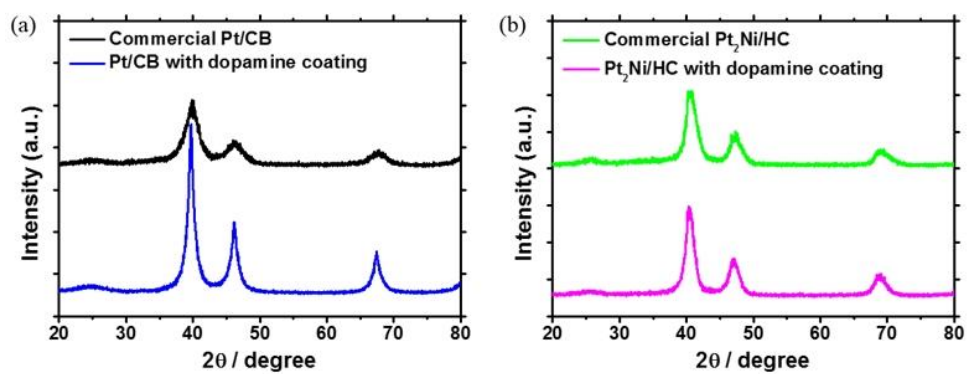
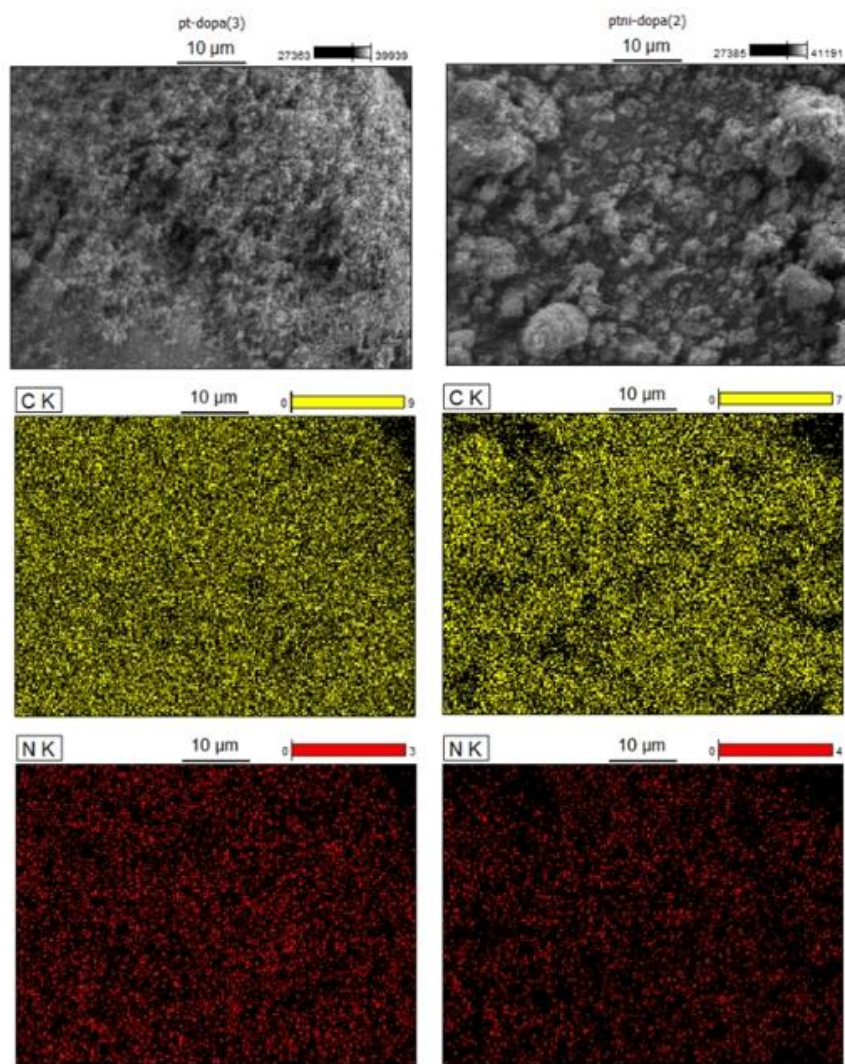


Figure 5.6 The XRD spectra of Pt/CB and the prepared Pt₂Ni/HC catalysts



Element	Pt/CB with dopamine coating		Pt ₂ Ni/HC with dopamine coating	
	wt%	at%	wt%	at%
C	99.14	99.28	99.35	99.40
N	0.86	0.72	0.65	0.60
Total	100.00	100.00	100.00	100.00

Figure 5.7 The SEM-EDS results of Pt/CB and the prepared Pt₂Ni/HC catalysts after dopamine coating.

These observations therefore confirm that dopamine coating partially inhibits catalyst particle growth during the heat treatment process. Moreover, under identical conditions, N-doped carbon shells of different thicknesses were formed for catalysts supported on CB and HC.

5.3.2. Evaluation of the Electrochemical Performances based on the Ionomer Content of Each Catalyst

As reported previously, the performance of a PEFC is greatly affected by the triple-phase boundary (TPB), which refers to the point at which the three phases, i.e., gas, liquid, and solid, converge. In a fuel cell, this refers to the reactant (gas), electrolyte (ionomer), and catalyst.[45] The electrolyte mainly serves as a medium for proton transport, and an excess of electrolyte can result in a decrease in cell performance, as the active sites (i.e., where the reactant gas reacts) on the surface of the catalyst become blocked. Conversely, if there is too little electrolyte, the proton transport pathway is reduced, and thus, the protons formed during the reaction cannot move effectively, thereby resulting in reduced fuel cell performance.[46] Therefore, optimisation of the TPB through adjustment of the electrolyte content is of particular importance for each individual catalyst system. In addition to single cell performance tests using the commercial 40 wt% Pt/CB catalysts (Figure 5.8 (a)), ionomer content tests were also performed to compare any differences in performance arising from the ionomer composition of the catalyst ink (Figures 5.8 (b)–3(d)).

For the anodes, a loading of 0.2 mg cm^{-2} was employed, as this loading does not affect the cathode performance. Initially, the commercial Pt/CB catalyst was applied to the cathode (Figure 5.8 (a)) for preparation of an MEA (denoted as PC) using the optimised ionomer content of 30 wt% with respect to the catalyst.[47] In the case of PC, a current density of 928 mA cm^{-2} was observed at 0.6 V in addition to a maximum power density of 723 mW cm^{-2} . However, it has previously been

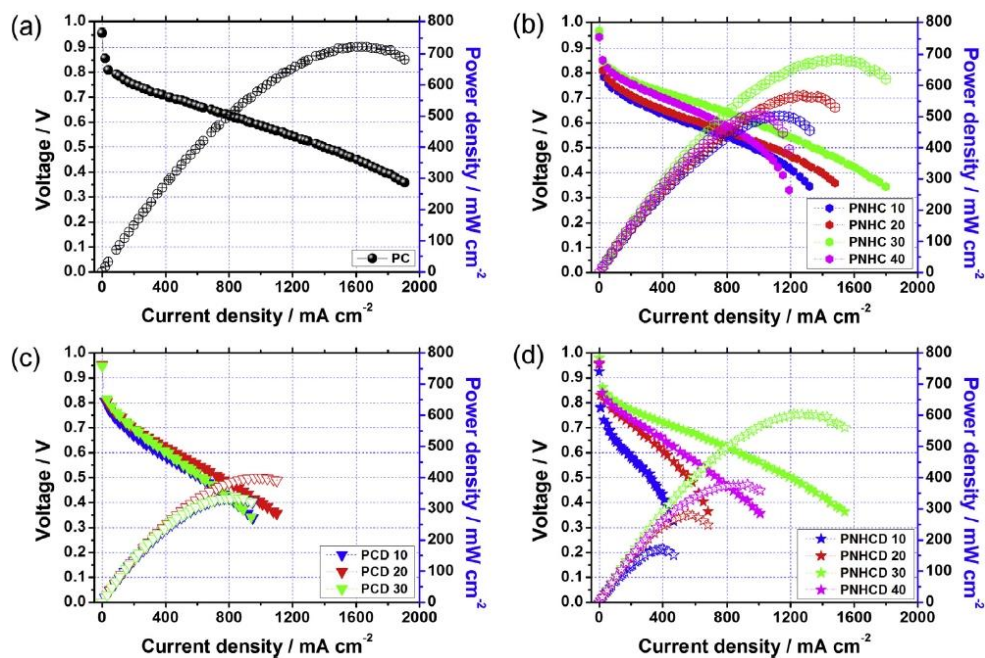


Figure 5.8 Electrochemical performance curves for (a) PC, (b) PNHC, (c) PCD, and (d) PNHCD. With the exception of PC, the ionomer content tests were performed to optimise the TPB. The ionomer contents relative to the catalyst are noted in the legends.

reported that when ordered mesoporous carbon was employed as a support, the optimum performance was achieved for systems based on a 10 wt% ionomer loading;[48] therefore, we examined ionomer contents between 10 and 40 wt% to determine the optimum TPB for this system. Figure 5.8(b) shows the results obtained upon varying the electrode ionomer contents in the presence of a commercial Pt₂Ni/HC catalyst, where the samples were labelled PNHC10, PNHC20, PNHC30, and PNHC40 based on their corresponding ionomer contents. As indicated, upon increasing the ionomer content, the performance tended to increase, and more specifically, increases in the ionomer content in the low current density region resulted in enhanced performances as the protons produced by the catalyst reaction were more effectively transferred to the required sites. However, we found that the optimal performance was observed for an ionomer loading of 30 wt% rather than 40 wt%. Compared to PC, the current density at 0.6 V was 5.5% higher (i.e., 979 mA cm⁻²), while the maximum power density was slightly lower (i.e., 684 mW cm⁻²), likely due to the intrinsic properties of the catalyst. More specifically, the half-wave potential in the half-cell data was higher than that of the commercial Pt/CB catalyst, but the limiting current was lower, as shown in Figure 5.9. In addition, the sharp decrease in performance in the presence of 40 wt% ionomer (PNHC40) at higher current densities was due to an excess of ionomer preventing effective TPB formation.

As the presence of a dopamine coating partially covers the Pt active sites and alters the physical structure of the catalyst (e.g., by changing the surface structure of the support), we examined the effect of ionomer content on TPB formation for the dopamine-coated Pt/CB and Pt₂Ni/C systems. In this case, Figure 5.8(c) shows the performances of the single cell MEAs containing dopamine-coated Pt/CB and 10–30 wt% ionomer (i.e., samples PCD10, PCD20, and PCD30). As shown, the performances of these three MEAs were <50% of that of PC, with PCD20 giving the optimal performance among these systems (i.e., a current density of 460 mA

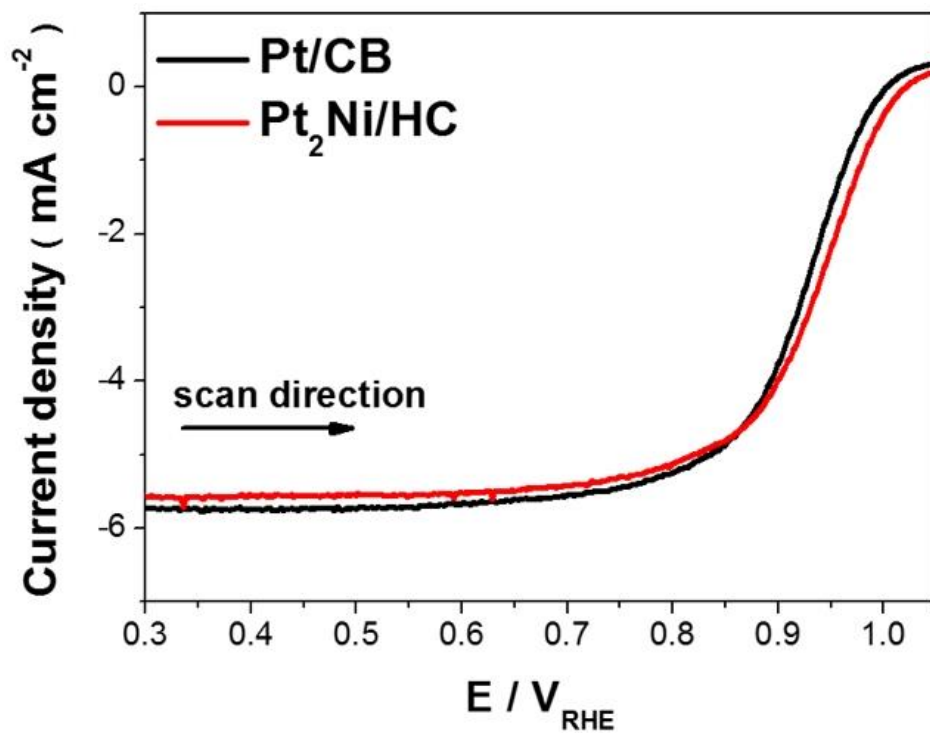


Figure 5.9 ORR activity of Pt/CB and Pt₂Ni/HC at 1600 rpm with 10 mV s⁻¹ in 0.5M H₂SO₄ solution.

cm^{-2} at 0.6 V and a maximum power density of 404 mW cm^{-2} , corresponding to 49.6 and 55.9% of the values of Pt/CB, respectively). As above, increases in performance were observed in the low current density region at higher ionomer contents. However, at an ionomer content of 30 wt%, the performance dropped in the high current density region, giving values comparable to that obtained for PCD10. We expect that this lower performance following coating is due to the partial growth of metal particles and the presence of a thick coating. According to a previous report,[30] dopamine coatings of $<1 \text{ nm}$ did not interfere with the mass transport of oxygen molecules, while for coatings thicker than 1 nm , the gas molecules were unable to easily reach the metal particle surface beneath the coating. Indeed, TEM analysis (Figure 5.2 (c)) confirmed that the performance decreased where coatings thicker than $1\text{--}2 \text{ nm}$ were present. It was therefore concluded that the higher performance exhibited by the system containing 20 wt% ionomer was due to partial coverage of the Pt active sites by the dopamine coating in the presence of 30 wt% ionomer. We then examined the effect of the ionomer content on the dopamine-coated $\text{Pt}_2\text{Ni}/\text{HC}$, as shown in Figure 5.8 (d), where the samples were denoted PNHCD10–PNHCD40 according to their ionomer contents. In this case, higher performances were once again observed upon increasing the ionomer content, although a reduced performance was obtained for the highest ionomer content (i.e., 40 wt%, PNHCD40). As before, this phenomenon was attributed to an excess ionomer content covering the active sites of the catalyst following coating with dopamine. Among these samples, the highest performance was achieved in the presence of 30 wt% ionomer (PNHCD30), although the current density at 0.6 V reached only 88.9% of that of PNHC30, while the maximum power density reached 94.3%. However, the values obtained for PNHCD30 are still significantly superior to those of all PCD (i.e., non-coated) systems, which were approximately 50% lower. In addition, since the best performance was obtained with the same ionomer content as for the uncoated $\text{Pt}_2\text{Ni}/\text{HC}$, the N-doped carbon

shell was considered thin enough to transport oxygen molecules from the outside to the metal surface.

The above results therefore confirm that the overall performances of the catalysts were reduced following dopamine coating, and the optimum ionomer contents were successfully determined for all systems. In this context, Table 5.1 shows the electrochemical performances of the prepared MEAs based on the optimum ionomer content for each catalyst.

5.3.3. Durability Tests

To confirm the durability of the catalysts in the MEAs, 200 h continuous load cycling tests were carried out as ADTs and the results are shown in Figures 5.10–5.11. We chose to apply load cycling using the ADT method as it is more taxing than other ADT methods, and consequently is more similar to authentic vehicle driving conditions where harsh conditions are common, e.g., high current densities (low cathode potentials), low current densities (high cathode potentials), and a holding period at the OCV.[49] In commonly used MEAs such as PC, the catalyst can be degraded by a number of routes, including Pt dissolution, Ostwald ripening, coalescence (agglomeration), particle detachment, and carbon corrosion.[50] These phenomena were therefore considered in the current test, and could be observed through both TEM and electrochemical analyses. As mentioned above, PC exhibited the best initial performance among the four types of system examined herein; however, following the ADTs, its reduction in performance was also the largest among the various samples. More specifically, compared to its initial performance, the current density at 0.6 V dropped to 41.4% (i.e., to 384 mA cm^{-2}) and the maximum power density reduced by 60.2% (i.e., to 435 mA cm^{-2}) (Figure 5.10 (a)).

As a number of reports indicate that catalyst activity and durability are increased in bimetallic systems, we examined the performance of PNHC, and found that the

Table 5.1 Summary of the electrochemical analyses of PC, PNHC, PCD, and PNHCD

	Ionomer content (ionomer/catalyst $\times 100$)	Before ADT			After ADT		
		Current density at 0.6V (mA cm^{-2})	Maximum Power density (mW cm^{-2})	ECS A ($\text{m}^2 \text{g}^{-1}$)	Current density at 0.6V (mA cm^{-2})	Maximum Power density (mW cm^{-2})	ECS A ($\text{m}^2 \text{g}^{-1}$)
PC	30	928	723	45.62	384	435	25.10
PNHC	30	979	684	56.83	727	514	50.83
PCD	20	460	404	33.63	700	575	30.82
PNHCD	30	870	607	34.86	747	579	43.98

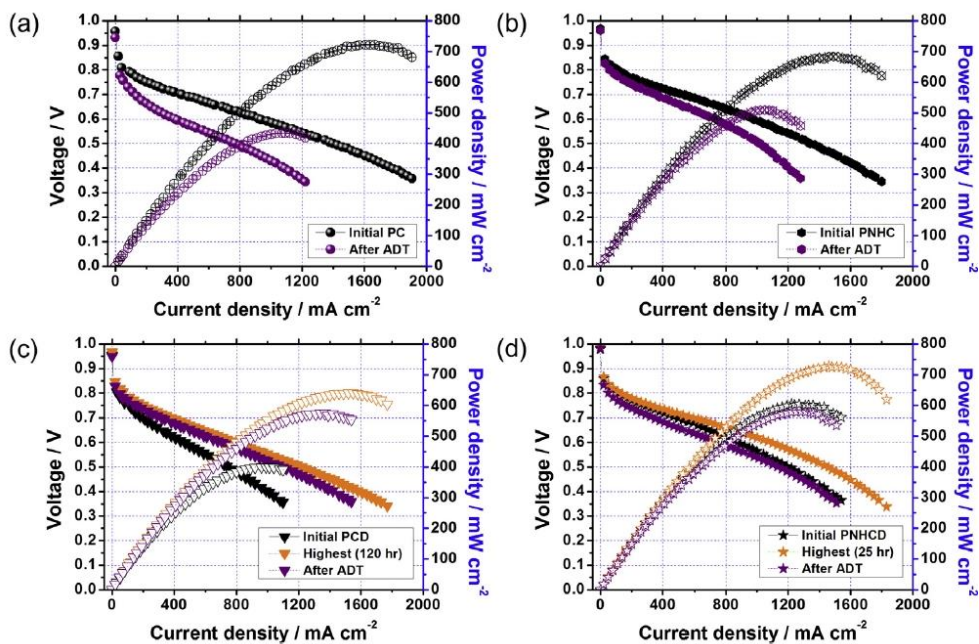


Figure 5.10 Electrochemical performance curves for (a) PC, (b) PNHC, (c) PCD, and (d) PNHCD before and after the ADTs.

initial performance was maintained up to 25 h (Figure 5.10 (b)), after which, compared with its initial performance following the ADT, the current density at 0.6 V and maximum power density reduced to 74.3% (i.e., 727 mA cm⁻²) and 75.1% (i.e., 514 mW cm⁻²), respectively. This could be attributed to the presence of a heat-treated carbon support, which can enhance interactions with the metal.[51] Furthermore, as reported in the literature,[52] Pt-Ni alloys are more resistant to sintering in MEAs compared to pure Pt. It has also been reported that a trade-off exists, in which the activity is increased when the particle size is small, and the stability is increased when the particle size is large.[53] These observations therefore indicate that PNHC exhibited a less significant performance decrease after the ADT than PC. Figure 5.10 (c) shows the performance curve obtained for PCD bearing an N-doped carbon shell on the catalyst surface. As indicated, the highest performance was obtained at 120 h (current density = 795 mA cm⁻² at 0.6 V, maximum power density = 641 mW cm⁻²) during the ADT. Similarly, the performance of PNHCD initially increased, with the highest performance being obtained after 25 h during the ADT (Figure 5.10 (d)). In this case, the current density at 0.6 V and the maximum power density were enhanced by 24.8% (i.e., to 1,086 mA cm⁻²) and 20.1% (i.e., to 729 mA cm⁻²), respectively, compared to the initial performance. Interestingly, these values are 1.170 and 1.008 times higher, respectively, than those exhibited initially by PC. Therefore, in terms of durability, formation of the N-doped carbon shell resulted in an increase in the maximum power density by 1.4 times in the case of Pt/CB, and a small decrease of 4.6% in the case of Pt₂Ni/HC after 200 h of continuous ADT.

Figure 5.11 shows both the current density at 0.6 V and the maximum power density trend for each MEA. For comparison, the data were normalised based on the initial values obtained for PC. As reported previously,[54] the performance of the PC system gradually decreased as the ADT progressed. Indeed, a similar observation was made in our experiments, as shown in Figure 5.11 (a). Similarly,

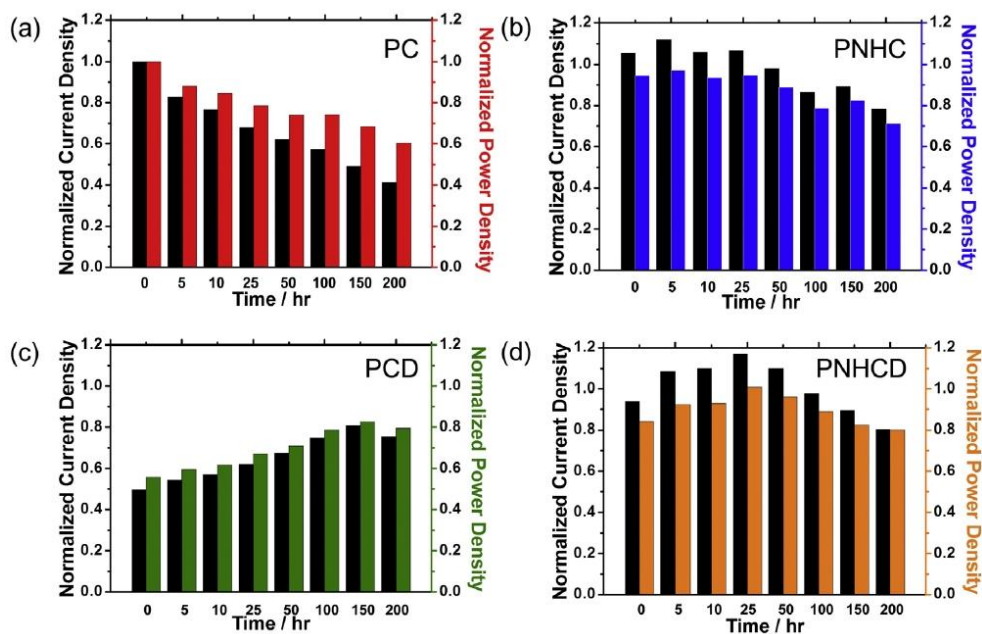


Figure 5.11 Trends of normalised current density (at 0.6 V) and maximum power density with ADT time: (a) PC, (b) PNHC, (c) PCD, and (d) PNHCD.

PNHC also exhibited a gradual decrease in its performance after approximately 25 h of the ADT, as shown in Figure 5.11 (b). In these two MEAs, it should be considered that degradation occurred progressively in the catalyst layer due to the previously mentioned catalyst degradation mechanism. In addition, Figure 5.11 (c) shows the variation in current density and the maximum power density of PCD, and confirms that the performance of this system increases with time. This can likely be accounted for by partial loss of the thick shell on the catalyst surface during degradation, thereby resulting in gradual exposure of the active sites, and a resulting increase in performance. Furthermore, after 120 h, the shell is no longer able to protect the catalyst and the performance of the PCD decreases due to degradation of the catalyst itself. In the case of PNHCD (Figure 5.11 (d)), an increase in performance was observed up to 25 h, potentially due to dissolution of the non-reactive phase in the transition metal catalyst in the presence of the N-doped carbon shell. Indeed, this improvement in the mass transfer properties was also observed in previous reports upon progression of the ADT.[55] However, after 25 h, a decrease in performance was observed for the PNHCD system. As in the case of PNHC, we expect that this was due to dissolution of the nickel present in the catalyst, since in contrast to the ADT conditions employed in a previous study (i.e., use of an N₂ atmosphere),[55] our ADTs were performed in a simulated driving environment under air. Indeed, Zhao et al.[56] reported that in an O₂ atmosphere, full dissolution of Ni was observed following the MEA tests, which is similar to the performance degradation observed due to the loss of nickel under ADT conditions in air.

We then examined the CV behaviour of the various samples before and after the ADT, as shown in Figure 5.12. These measurements were carried out under a H₂/N₂ environment. In the case of PC (Figure 5.12 (a)), the initial ECSA of 45.62 m² g⁻¹ was reduced by 55.0% to 25 m² g⁻¹ following the ADT. However, in the case of PNHC (Figure 5.12 (b)), the ECSA was reduced by only 9.0% from the initial

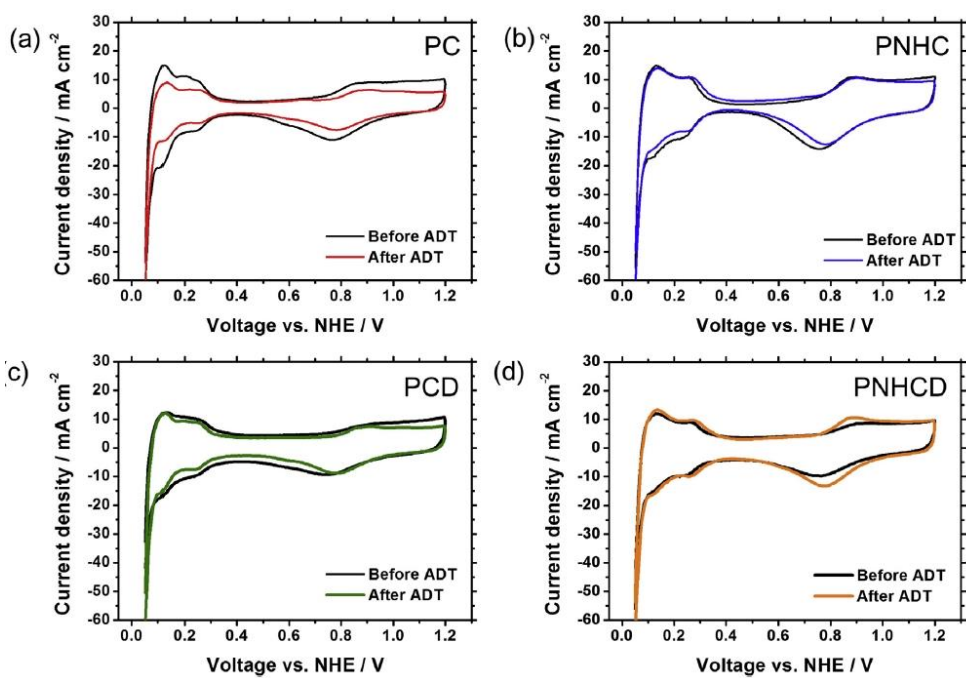


Figure 5.12 CV results for (a) PC, (b) PNHC, (c) PCD, and (d) PNHCD before and after the ADT.

value of $56.83 \text{ m}^2 \text{ g}^{-1}$ (i.e., to $50.80 \text{ m}^2 \text{ g}^{-1}$). In addition, as shown in Figure 5.12 (c), the ECSA of PCD prior to the ADT was $33.63 \text{ m}^2 \text{ g}^{-1}$, which is 26.2% less than that achieved prior to introduction of the dopamine coating. Indeed, the initial ECSA of PCD was low due to the growth of particles in the annealing process employed during introduction of the N-doped carbon shell, and also due to the relatively thick coating (i.e., 1.5–2.3 nm) present in the final sample. Thus, following the ADT, the ECSA decreased to $30.82 \text{ m}^2 \text{ g}^{-1}$, and the hydrogen adsorption/desorption peaks between 0.050 and 0.45 V were sharp. These observations also imply that the initially covered Pt active sites became exposed as the ADT progressed. Furthermore, Figure 5.12 (d) shows the CV results of the PNHCD sample before and after the ADT. As indicated, the ECSA increased from 34.86 to $43.98 \text{ m}^2 \text{ g}^{-1}$, and thus, the obtained results suggest that the 0.95 nm-thick shell was removed during the ADT, ultimately resulting in Ni dissolution. Moreover, after coating, the double layer became thicker in both cases, as shown in Figures 5.12 (a) and (c) for Pt/CB and Figures 5.12 (b) and (d) for Pt₂Ni/HC. This is likely due to the N-doped carbon shell influencing the surface properties of the carbon support, especially considering that the double layer is affected by the interface between the proton conductive materials (i.e., the membrane and the ionomer) and the catalyst, due to the charge exchanged during electroadsorption/desorption.[57] Since in this case the quantities of ionomer and Pt were equivalent, these results may originate from the support, whose surface properties were influenced by the N-doped carbon shell. Additionally, it was confirmed that this coating causes a decrease in the ECSA. Although the coating of PNHCD is thinner than that of PCD, a greater reduction in the ECSA was observed after coating for this sample. However, after coating, the initial performance of PNHCD was superior to that of PCD, thereby indicating that the ECSA, which merely reflected the adsorption/desorption of hydrogen, is not proportional to the performance. In addition, the ECSA excludes factors that affect the performance of

the actual MEA (or single cell) in the overall reaction, including gas diffusion, the ionic pathway, proton conductivity, the mass transfer of reactants, and the management of water. Indeed, a number of other studies have reported that the ECSA is not directly proportional to the performance.[58,59] It is therefore likely that the Pt₂Ni/HC catalyst employed herein is more sensitive to the effects of simple electrochemical analysis following dopamine coating. Indeed, after 200 h, the CV results indicate that the double layer of PNHCD remained essentially unchanged, unlike in the case of PCD. This indicates that the surface properties of the carbon applied to the support did not change after 200 h of the ADT. In addition, these results also indicate that Ni dissolution caused a decrease in performance rather than degradation of the support. In contrast, in the case of PCD, degradation also occurred in the support due to changes in the double layer itself.

5.3.4. TEM Analysis after the ADT

Following the ADT, the MEAs were separated from each single cell, and the cathodes were analysed by TEM. The corresponding TEM images and particle size distributions for each catalyst are shown in Figure 5.13 and Figure 5.14, respectively. As indicated, after completion of the ADT, larger particles were observed for PC (8.97 ± 2.16 nm, Figure 5.13 (a)) than for the initial catalyst (3.40 ± 1.04 nm), and the spherical carbon support also exhibited severe deformation. In the case of PNHC (Figure 5.13 (b)), although the Pt alloy particles grew slightly in size (i.e., to 8.28 ± 2.21 nm), the shape of the support remained relatively unchanged. Similarly, larger Pt particles were observed for the PCD sample after the ADT (Figure 5.13 (c)), but again, no severe support deformation was observed. This suggests that the N-doped carbon shell not only protected the Pt but also protected the support during the ADT. We expect that this was due to blockage of the high surface area and corrosion-prone amorphous CB by the graphitic N-doped

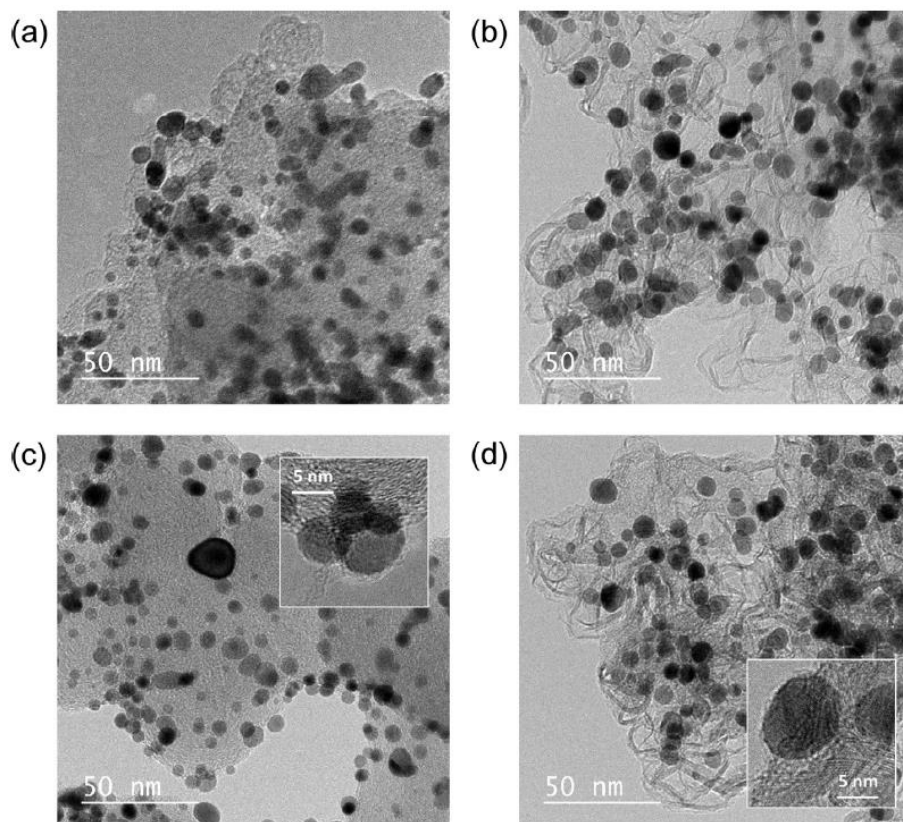


Figure 5.13 TEM images of the catalysts extracted from the MEAs after the ADT. (a) Pt/CB and (b) Pt₂Ni/HC before dopamine coating, and (c) Pt/CB and (d) Pt₂Ni/HC after dopamine coating. The insets in parts (c) and (d) show the high resolution TEM images.

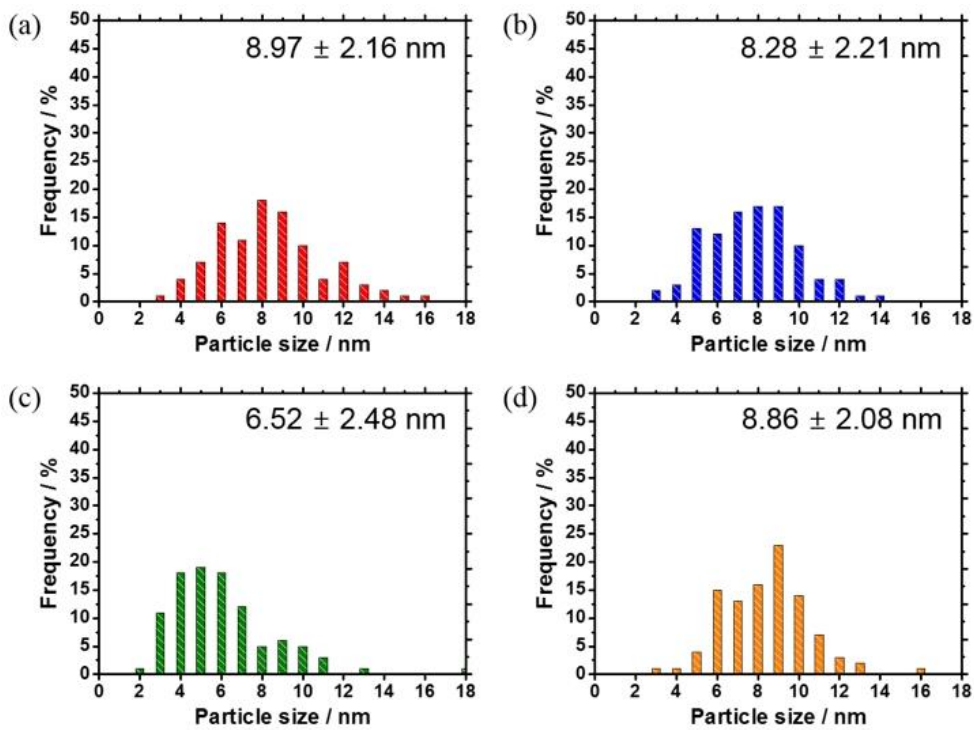


Figure 5.14 Particle size distribution of each catalyst extracted from cathode electrode of (a) PC, (b) PNHC, (c) PCD, and (d) PNHCD after ADT.

carbon in the fuel cell operating environment. It was also observed that the shell was separated from the surface of the Pt particles (inset of Figure 5.13 (c)) and the thickness was found to be considerably reduced. Finally, no significant growth was observed for the Pt particles of PNHCD (8.86 ± 2.08 nm) after the ADT, as shown in Figure 5.13 (d), and little deformation of the carbon support took place. However, it was confirmed from high resolution images (inset of Figure 5.13 (d)) that portions of the N-doped carbon shell were removed, and the metal surface was partially exposed. These results therefore confirmed that the N-doped carbon shell derived from the dopamine coating aided in preventing the aggregation of metal catalyst particles in the system examined herein.

5.4. Conclusions

We herein report the introduction of a nitrogen-doped carbon shell by dopamine coating on the surfaces of highly loaded platinum- and platinum-nickel alloy catalysts possessing different types of carbon supports to enhance the durability of polymer electrolyte membrane fuel cells. When coating was carried out under the same conditions, thick (1.5–2.3 nm) N-doped carbon shells were formed on the surfaces of Pt/carbon black (CB) particles, while thin (0.47–0.95 nm) layers were formed on the surfaces of Pt₂Ni/heat-treated Ketjen black carbon (HC) particles due to differences in their surface properties, such as the hydrophobicity of the heat-treated carbon support. Due to changes in the catalyst surfaces, it was important to form an optimal triple-phase boundary by adjusting the ionomer content when N-doped carbon was introduced, as this resulted in increased fuel cell durability. We found that the optimal ionomer content was 20 wt% for dopamine-coated Pt/CB (PCD) and 30 wt% for dopamine-coated Pt₂Ni/HC (PNHCD). In addition, prior to dopamine treatment, the performances of the single cells decreased with longer accelerated degradation test (ADT) times, while after dopamine coating, the N-doped carbon shells present on the catalyst surfaces reduced the initial performance but increased the durability. In the case of PCD, which contained a rather thick shell, the performance increased by ≤ 1.73 times as the active sites became exposed with increasing ADT time, however this system reached only 85.7% of the initial performance of commercial Pt/CB (PC). Furthermore, in the case of the bimetallic PNHCD system, the non-reactive phase of the transition metal dissolved selectively, and the performance increased by 1.25 times during the ADT compared with its initial performance (i.e., a 17% improvement over the initial performance of PC). Our results also confirmed that the thickness of the N-doped carbon shell was determined by the heat treatment of carbon, which effectively improved the durability of these systems. Moreover, the overall performance was improved by applying a Pt-alloy catalyst in combination

with an N-doped carbon shell, thereby yielding a highly durable catalyst, as confirmed by membrane electrolyte assembly durability measurements. It is therefore expected that further improvements in the durability of highly active catalysts can be achieved by controlling parameters such as the heat treatment conditions for the carbon support and the metal composition at the time of catalyst design.

5.5. References

- 1 Nørskov, J. K. *et al.* Origin of the Overpotential for Oxygen Reduction at a Fuel-Cell Cathode. *The Journal of Physical Chemistry B* **108**, 17886-17892 (2004).
- 2 Yu, X. & Ye, S. Recent advances in activity and durability enhancement of Pt/C catalytic cathode in PEMFC: Part II: Degradation mechanism and durability enhancement of carbon supported platinum catalyst. *Journal of Power Sources* **172**, 145-154 (2007).
- 3 Stamenkovic, V. R. *et al.* Trends in electrocatalysis on extended and nanoscale Pt-bimetallic alloy surfaces. *Nat Mater* **6**, 241-247 (2007).
- 4 Greeley, J. *et al.* Alloys of platinum and early transition metals as oxygen reduction electrocatalysts. *Nat Chem* **1**, 552-556 (2009).
- 5 Guo, S. & Sun, S. FePt Nanoparticles Assembled on Graphene as Enhanced Catalyst for Oxygen Reduction Reaction. *Journal of the American Chemical Society* **134**, 2492-2495 (2012).
- 6 Zhang, L. *et al.* Platinum-based nanocages with subnanometer-thick walls and well-defined, controllable facets. *Science* **349**, 412-416 (2015).
- 7 Antolini, E. Carbon supports for low-temperature fuel cell catalysts. *Applied Catalysis B: Environmental* **88**, 1-24 (2009).
- 8 Park, J., Wang, H., Vara, M. & Xia, Y. Platinum Cubic Nanoframes with Enhanced Catalytic Activity and Durability Toward Oxygen Reduction. *ChemSusChem* **9**, 2855-2861 (2016).
- 9 Zhang, G. *et al.* Core-shell Pt modified Pd/C as an active and durable electrocatalyst for the oxygen reduction reaction in PEMFCs. *Applied Catalysis B: Environmental* **132-133**, 183-194 (2013).
- 10 Chen, C. *et al.* Highly Crystalline Multimetallic Nanoframes with Three-Dimensional Electrocatalytic Surfaces. *Science* **343**, 1339-1343 (2014).
- 11 Liu, X.-J. *et al.* Hollow ternary PtPdCu nanoparticles: a superior and

- durable cathodic electrocatalyst. *Chemical Science* **6**, 3038-3043 (2015).
- 12 Eid, K. *et al.* Trimetallic PtPdRu Dendritic Nanocages with Three-Dimensional Electrocatalytic Surfaces. *The Journal of Physical Chemistry C* **119**, 19947-19953 (2015).
- 13 Yang, T. *et al.* High Durable Ternary Nanodendrites as Effective Catalysts for Oxygen Reduction Reaction. *ACS applied materials & interfaces* **8**, 23646-23654 (2016).
- 14 Park, J. *et al.* Coating Pt–Ni Octahedra with Ultrathin Pt Shells to Enhance the Durability without Compromising the Activity toward Oxygen Reduction. *ChemSusChem* **9**, 2209-2215 (2016).
- 15 Watanabe, M., Yano, H., Tryk, D. A. & Uchida, H. Highly Durable and Active PtCo Alloy/Graphitized Carbon Black Cathode Catalysts by Controlled Deposition of Stabilized Pt Skin Layers. *Journal of The Electrochemical Society* **163**, F455-F463 (2016).
- 16 Lee, T. K., Jung, J. H., Kim, J. B. & Hur, S. H. Improved durability of Pt/CNT catalysts by the low temperature self-catalyzed reduction for the PEM fuel cells. *International Journal of Hydrogen Energy* **37**, 17992-18000 (2012).
- 17 Choi, J.-Y., Higgins, D. & Chen, Z. Highly Durable Graphene Nanosheet Supported Iron Catalyst for Oxygen Reduction Reaction in PEM Fuel Cells. *Journal of The Electrochemical Society* **159**, B86-B89 (2012).
- 18 Cheng, N. *et al.* High stability and activity of Pt electrocatalyst on atomic layer deposited metal oxide/nitrogen-doped graphene hybrid support. *International Journal of Hydrogen Energy* **39**, 15967-15974 (2014).
- 19 Hoque, M. A. *et al.* Multigrain Platinum Nanowires Consisting of Oriented Nanoparticles Anchored on Sulfur-Doped Graphene as a Highly Active and Durable Oxygen Reduction Electrocatalyst. *Advanced Materials* **27**, 1229-1234 (2015).

- 20 Cheon, J. Y. *et al.* Ordered mesoporous carbon-carbon nanotube nanocomposites as highly conductive and durable cathode catalyst supports for polymer electrolyte fuel cells. *Journal of Materials Chemistry A* **1**, 1270-1283 (2013).
- 21 Huang, S.-Y., Ganesan, P., Park, S. & Popov, B. N. Development of a Titanium Dioxide-Supported Platinum Catalyst with Ultrahigh Stability for Polymer Electrolyte Membrane Fuel Cell Applications. *Journal of the American Chemical Society* **131**, 13898-13899 (2009).
- 22 Kakinuma, K., Uchida, M., Kamino, T., Uchida, H. & Watanabe, M. Synthesis and electrochemical characterization of Pt catalyst supported on Sn_{0.96}Sb_{0.04}O_{2-δ} with a network structure. *Electrochimica Acta* **56**, 2881-2887 (2011).
- 23 Cilingir Dogan, D. *et al.* Highly Durable Metal-Oxides as an Alternative Catalyst Supports for PEFCs. *ECS Transactions* **58**, 1843-1847 (2013).
- 24 Dhanasekaran, P., Vinod Selvaganesh, S. & Bhat, S. D. Nitrogen and carbon doped titanium oxide as an alternative and durable electrocatalyst support in polymer electrolyte fuel cells. *Journal of Power Sources* **304**, 360-372 (2016).
- 25 Yoshii, K. *et al.* Highly durable Pt nanoparticle-supported carbon catalysts for the oxygen reduction reaction tailored by using an ionic liquid thin layer. *Journal of Materials Chemistry A* **4**, 12152-12157 (2016).
- 26 Lee, J. *et al.* Development of Highly Stable and Mass Transfer-Enhanced Cathode Catalysts: Support-Free Electrospun Intermetallic FePt Nanotubes for Polymer Electrolyte Membrane Fuel Cells. *Adv. Energy Mater.* **5**, 1402093-n/a (2015).
- 27 Awaludin, Z., Sheng Moo, J. G., Okajima, T. & Ohsaka, T. TaO_x-capped Pt nanoparticles as active and durable electrocatalysts for oxygen reduction. *Journal of Materials Chemistry A* **1**, 14754-14765 (2013).

- 28 Nie, Y. *et al.* Pt/C trapped in activated graphitic carbon layers as a highly durable electrocatalyst for the oxygen reduction reaction. *Chemical Communications* **50**, 15431-15434 (2014).
- 29 Lee, H., Sung, Y.-E., Choi, I., Lim, T. & Kwon, O. J. Novel synthesis of highly durable and active Pt catalyst encapsulated in nitrogen containing carbon for polymer electrolyte membrane fuel cell. *Journal of Power Sources* **362**, 228-235 (2017).
- 30 Chung, D. Y. *et al.* Highly Durable and Active PtFe Nanocatalyst for Electrochemical Oxygen Reduction Reaction. *Journal of the American Chemical Society* **137**, 15478-15485 (2015).
- 31 Zhang, Z. *et al.* Facile synthesis of N-doped porous carbon encapsulated bimetallic PdCo as a highly active and durable electrocatalyst for oxygen reduction and ethanol oxidation. *Journal of Materials Chemistry A* **5**, 10876-10884 (2017).
- 32 Cho, Y., Lee, W. H. & Kim, H. Preparation of a Carbon-Supported Pt-Ni Bimetallic Catalyst with a Pt-Rich Shell Using a Dopamine as Protective Coating. *Journal of The Electrochemical Society* **164**, F65-F70 (2017).
- 33 Kim, H. S. *et al.* Platinum catalysts protected by N-doped carbon for highly efficient and durable polymer-electrolyte membrane fuel cells. *Electrochimica Acta* **193**, 191-198 (2016).
- 34 Jung, C. *et al.* Synthesis of Chemically Ordered Pt₃Fe/C Intermetallic Electrocatalysts for Oxygen Reduction Reaction with Enhanced Activity and Durability via a Removable Carbon Coating. *ACS applied materials & interfaces* **9**, 31806-31815 (2017).
- 35 Tong, X. *et al.* Ultrathin Carbon-Coated Pt/Carbon Nanotubes: A Highly Durable Electrocatalyst for Oxygen Reduction. *Chemistry of Materials* **29**, 9579-9587 (2017).
- 36 Kim, H., Robertson, A. W., Kim, S. O., Kim, J. M. & Warner, J. H.

- Resilient High Catalytic Performance of Platinum Nanocatalysts with Porous Graphene Envelope. *ACS Nano* **9**, 5947-5957 (2015).
- 37 Hu, Y. *et al.* Hollow Spheres of Iron Carbide Nanoparticles Encased in Graphitic Layers as Oxygen Reduction Catalysts. *Angewandte Chemie International Edition* **53**, 3675-3679 (2014).
- 38 Sivakumar, P. *et al.* Electrochemical Oxygen Reduction Activity of Metal Embedded Nitrogen Doped Carbon Nanostructures Derived from Pyrolysis of Nitrogen-Rich Guanidinium Salt. *Journal of The Electrochemical Society* **164**, F781-F789 (2017).
- 39 Maiyalagan, T. & Pasupathi, S. Components for PEM Fuel Cells: An Overview. *Materials Science Forum* **657**, 143-189 (2010).
- 40 Wang, H., Maiyalagan, T. & Wang, X. Review on Recent Progress in Nitrogen-Doped Graphene: Synthesis, Characterization, and Its Potential Applications. *ACS Catalysis* **2**, 781-794 (2012).
- 41 Thandavarayan Maiyalagan, Subbiah Maheswari, Saji, V. S. & in *Electrocatalysts for Low Temperature Fuel Cells* (eds Thandavarayan Maiyalagan & Viswanathan S Saji) Ch. 13, 401-421 (Wiley-VCH Verlag GmbH & Co. KGaA, 2017).
- 42 Thakur, V. K., Lin, M.-F., Tan, E. J. & Lee, P. S. Green aqueous modification of fluoropolymers for energy storage applications. *Journal of Materials Chemistry* **22**, 5951-5959 (2012).
- 43 Coloma, F., Sepulvedaescribano, A. & Rodriguezreinoso, F. Heat-Treated Carbon-Blacks as Supports for Platinum Catalysts. *Journal of Catalysis* **154**, 299-305 (1995).
- 44 Sheng, Z. M. & Wang, J. N. Thin-Walled Carbon Nanocages: Direct Growth, Characterization, and Applications. *Advanced Materials* **20**, 1071-1075 (2008).
- 45 Kim, K.-H. *et al.* The effects of Nafion® ionomer content in PEMFC

- MEAs prepared by a catalyst-coated membrane (CCM) spraying method. *International Journal of Hydrogen Energy* **35**, 2119-2126 (2010).
- 46 Suzuki, A. *et al.* Ionomer content in the catalyst layer of polymer electrolyte membrane fuel cell (PEMFC): Effects on diffusion and performance. *International Journal of Hydrogen Energy* **36**, 2221-2229 (2011).
- 47 Lim, J. W. *et al.* Ionic Resistance of a Cathode Catalyst Layer with Various Thicknesses by Electrochemical Impedance Spectroscopy for PEMFC. *Journal of The Electrochemical Society* **159**, B378-B384 (2012).
- 48 Ahn, C.-Y., Cheon, J.-Y., Joo, S.-H. & Kim, J. Effects of ionomer content on Pt catalyst/ordered mesoporous carbon support in polymer electrolyte membrane fuel cells. *Journal of Power Sources* **222**, 477-482 (2013).
- 49 Cho, Y.-H. *et al.* Characteristics and performance of membrane electrode assemblies with operating conditions in polymer electrolyte membrane fuel cell. *Electrochimica Acta* **56**, 717-721 (2010).
- 50 Meier, J. C. *et al.* Design criteria for stable Pt/C fuel cell catalysts. *Beilstein Journal of Nanotechnology* **5**, 44-67 (2014).
- 51 Zhao, X. *et al.* Evaluation of change in nanostructure through the heat treatment of carbon materials and their durability for the start/stop operation of polymer electrolyte fuel cells. *Electrochimica Acta* **97**, 33-41 (2013).
- 52 Cho, Y.-H. *et al.* Performance and stability characteristics of MEAs with carbon-supported Pt and Pt1Ni1 nanoparticles as cathode catalysts in PEM fuel cell. *International Journal of Hydrogen Energy* **36**, 4394-4399 (2011).
- 53 Matsutani, K., Hayakawa, K. & Tada, T. Effect of particle size of platinum and platinum-cobalt catalysts on stability against load cycling: Towards the development of high performance, stable fuel cell catalysts with low platinum loadings. *Platinum Metals Review* **54**, 223-232 (2010).

- 54 Kim, O.-H. *et al.* Realization of Both High-Performance and Enhanced Durability of Fuel Cells: Pt-Exoskeleton Structure Electrocatalysts. *ACS applied materials & interfaces* **7**, 14053-14063 (2015).
- 55 Wu, G., More, K. L., Johnston, C. M. & Zelenay, P. High-Performance Electrocatalysts for Oxygen Reduction Derived from Polyaniline, Iron, and Cobalt. *Science* **332**, 443-447 (2011).
- 56 Zhao, J., Jarvis, K., Ferreira, P. & Manthiram, A. Performance and stability of Pd-Pt-Ni nanoalloy electrocatalysts in proton exchange membrane fuel cells. *Journal of Power Sources* **196**, 4515-4523 (2011).
- 57 Zhang, J., Zhang, H., Wu, J. & Zhang, J. in *Pem Fuel Cell Testing and Diagnosis* 81-119 (Elsevier, 2013).
- 58 Shrestha, S., Asheghi, S., Timbro, J. & Mustain, W. E. Temperature controlled surface chemistry of nitrogen-doped mesoporous carbon and its influence on Pt ORR activity. *Applied Catalysis A: General* **464-465**, 233-242 (2013).
- 59 Shanmugam, S., Sanetuntikul, J., Momma, T. & Osaka, T. Enhanced Oxygen Reduction Activities of Pt Supported on Nitrogen-Doped Carbon Nanocapsules. *Electrochimica Acta* **137**, 41-48 (2014).

Appendix A. Preparation of *in-situ* XAFS Cell In-operando Single Cell Tests for Structural Analysis of Cathode Catalyst

X-ray absorption fine structure (XAFS) is a tool for analyzing the local structure properties, chemical valence state and local density of states of materials. Many groups have used them to analyze and study the properties of materials. However, only the characteristics of the material itself were confirmed, and it was difficult to identify the electro-catalyst in which the external influences were reflected. In particular, it has been difficult to identify the energy devices with complex variables such as fuel cells.

In this study, we designed a single cell for the analysis of cathode catalyst integrated with MEA rather than a half cell level analysis. Furthermore, a system capable of analyzing not only nitrogen but also oxygen (air) atmospheres was introduced. Therefore, analysis of the catalyst was carried out in a high current density region and corresponding voltage which can not be measured under the nitrogen atmosphere. Furthermore, a unit cell for the transmission mode and the fluorescence mode was developed and applied to the accelerator laboratory.

For the preparation of membrane electrolyte assemblies (MEAs) inks, Pt/C and synthesized 30 wt% Pd/C were dispersed in distilled water and isopropyl alcohol using a homogenizer with an amplitude of 30% for 3 min. A Nafion[®] solution was added to the Pt/C and Pd/C solution and homogenized again for another 3 min. MEAs were prepared by the catalyst-coated membrane (CCM) method. Catalyst inks were added into a feed cup of a spray gun and spread over the membrane using a nitrogen. The active area of MEAs was 5 cm². As shown in Figure a.1, the

prepared cell for the transmission mode and the fluorescence mode were fixed at 90 degrees and 45 degrees of the incident synchrotron X-ray, respectively. The system after installation in the XAFS measurement room (8C beamline Pohang Accelerator Laboratory; PAL) is shown in the figure a.2.

As a results, we are now able to analyze XAFS under practical fuel cell operation conditions, and we will analyze various catalysts based on this. Furthermore, this study can be extended to analyzing the components of fuel cells composed of metal such as a metal flow field, MEAs with cracks as well as an electro-catalyst.

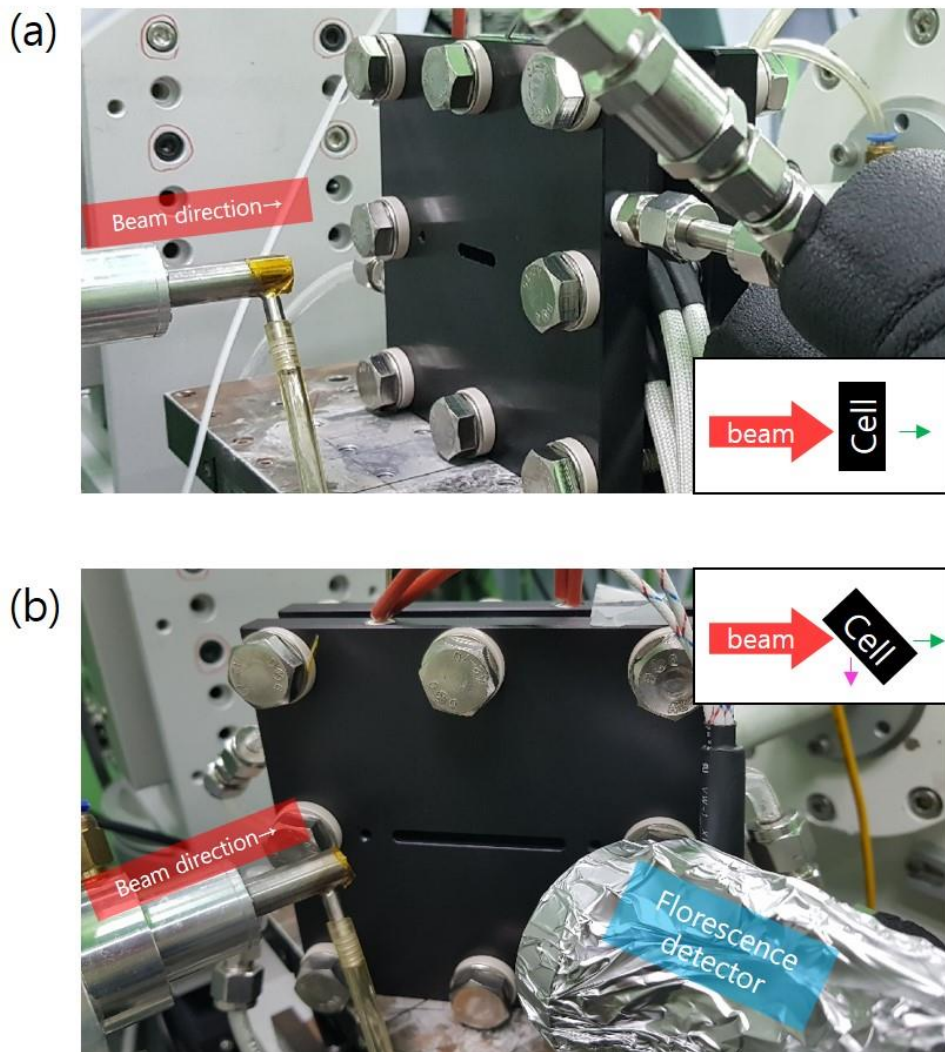


Figure a.1 XAFS measurement pictures of (a) the transmission mode and (b) the fluorescent cell unit cell.



Figure a.2 Fuel cell evaluation system set up at PAL 8C beamline

국문초록

고분자 전해질 막 연료전지는 배기가스가 거의 없기 때문에, 화석연료를 대체할 수 있는 후보 중 하나인 수소의 어플리케이션으로 많은 연구가 되고 있다. 그러나 비싼 부품들 때문에 가격에 대한 이점이 아직 내연기관에 미치지 못하기 때문에, 상용화를 위해서는 아직도 많은 연구들이 필요하다. 이 연료전지를 이루는 구성요소는 크게 막, 전극, 기체 확산층, 및 유로이다. 따라서 본 졸업 논문의 주제는 연료전지의 구성요소를 구조적으로 변경하여, 향상된 성능과 내구성을 분석하는데에 있다.

1장에서는 고분자 전해질막 연료전지에 대해 간략히 소개를 하고, 연료전지의 구성요소의 특징과, 역할 및 해결해야할 점에 대해 언급한다.

2 장에서 다공성 금속을 분석하였고, 고분자 전해질 막 연료전지 단위 셀의 유로로 적용했다. 또한, 다공성 금속의 전기 화학적 성능을 통상적으로 사용되는 사형 유로의 전기 화학적 성능과 비교 하였다. 상대 습도가 100 % 일 때 다공성 금속과 사형 유로 사이에는 큰 차이가 없었다. 그러나, 다공성 금속을 갖는 연료전지의 성능은 가압 및 상대습도 20 % 조건에서 일반적인 유로의 성능보다 우수 하였다. 또한, 유로의 적용에 의한 연료 전지 성능에 영향을 미치는 요인에 대해서도 논의 하였다.

3 장에서는 고분자 전해질 막 연료 전지의 성능 향상을 위해 전극의 균열 생성을 살펴 보았다. 이것은 일반적인 에너지 어플리케이션에서는 결함으로 간주되는 균열을 사용하여 연료전지의 성능을 향상시키는 첫 번째 시도였다. 균열이 생성 된 전극은 촉매가 코팅 된 나피온 막을 늘려서 생성되었다. 소성 변형의 측면에서, 독특한 나피온 멤브레인의

응력-변형 특성으로 막-전극 접합체는 성공적으로 연료 전지에 통합되었다. 여러가지 비율의 변형이 적용된 균열 전극을 조사하고 전기 화학적으로 평가 하였다. 놀랍게도 촉매로 코팅 된 나피온 막의 기계적 신축으로 인해 막 저항이 감소하였고 물질 전달이 향상되어 장치 성능이 향상되었다.

4 장에서는 3장의 연장선에 대한 연구로써, 프리즘 패턴을 포함하는 나피온 멤브레인의 집중 표면 응력을 이용한 전극에서, 균열이 패턴과 유사한 형태로 성공적으로 발생된 것을 연구하였다. 유도된 균열을 갖는 전극은 촉매로 코팅 된 나피온 막을 연신함으로써 형성되었다. 프리즘 패턴 간격 (20 μm 와 50 μm)과 여러 변형률 ($S \approx 0.5$ 와 1.0)에서의 변화에 대해 막-전극 접합체의 형태학적 특징을 조사했다. 균열이 생성된 전극의 표면상의 물의 거동을 환경 주사 전자 현미경을 사용하여 조사하였다. 전극 층의 균열은 물의 효율적인 저장 및 통로 인 것으로 나타났다. 비교 연구를 위해, 유도 균열이 있는 것과 없는 일반적인 막-전극 접합체를 연료 전지에 통합시켜 전기 화학적 측정을 수행하였다. 예상 한 바와 같이, 균열이 있는 모든 막-전극 접합체는 기존의 막-전극 접합체보다 우수한 성능을 보였다.

5 장에서는 두 가지 유형의 탄소 지지체가 적용된, 담지량 높은 백금 및 백금-니켈 합금 촉매의 내구성을 높이기 위해 질소 도핑 된 탄소 껍질을 도파민 코팅을 통해 촉매 표면에 도입했다. 촉매 표면이 탄소 껍질 형성 후 변경됨에 따라, 촉매 잉크의 이오노머 함량은 삼상 경계의 형성을 최적화 되도록 조절하여 실험하였다. 막-전극 접합체 적용하여 단위전지 실험 수행하였다. 또한, 촉매의 내구성을 확인하기 위해, 70 $^{\circ}\text{C}$ 및 상대 습도 100 %에서 200 시간 동안 가속 열화 실험하였다. 내구성 시험

전후에 투과 전자 현미경 및 전기 화학적 분석을 수행하였고, 관찰 된 현상에 대해 논의하였다.

부록에서는 X 선 흡수 미세 구조 (XAFS) 분석을위한 단일 셀의 개발에 대해 설명한다. XAFS는 금속 재료의 전기적 및 구조적 특성을 분석 할 수있는 도구 중 하나이다. 이 장에서는 포항 가속기 연구소 내에 설치 될 수 있는 연료 전지 평가 시스템을 설계하고 설치하는 것을 포함한다. 또한 실제 연료전지 운전 조건에서 XAFS 분석을 가능하게 하는 새로운 유형의 단전지를 개발했다. 본 연구는 앞으로 실제 구동 조건에서 연료전지 구성요소를 분석하는데 큰 역할을 할 것으로 판단된다.

주요어: 연료전지, 구성요소, 유로, 막전극접합체, 구조 변형, 성능, 내구성

학번: 2014-31090